CHALMERS
UNIVERSITY OF TECHNOLOGY

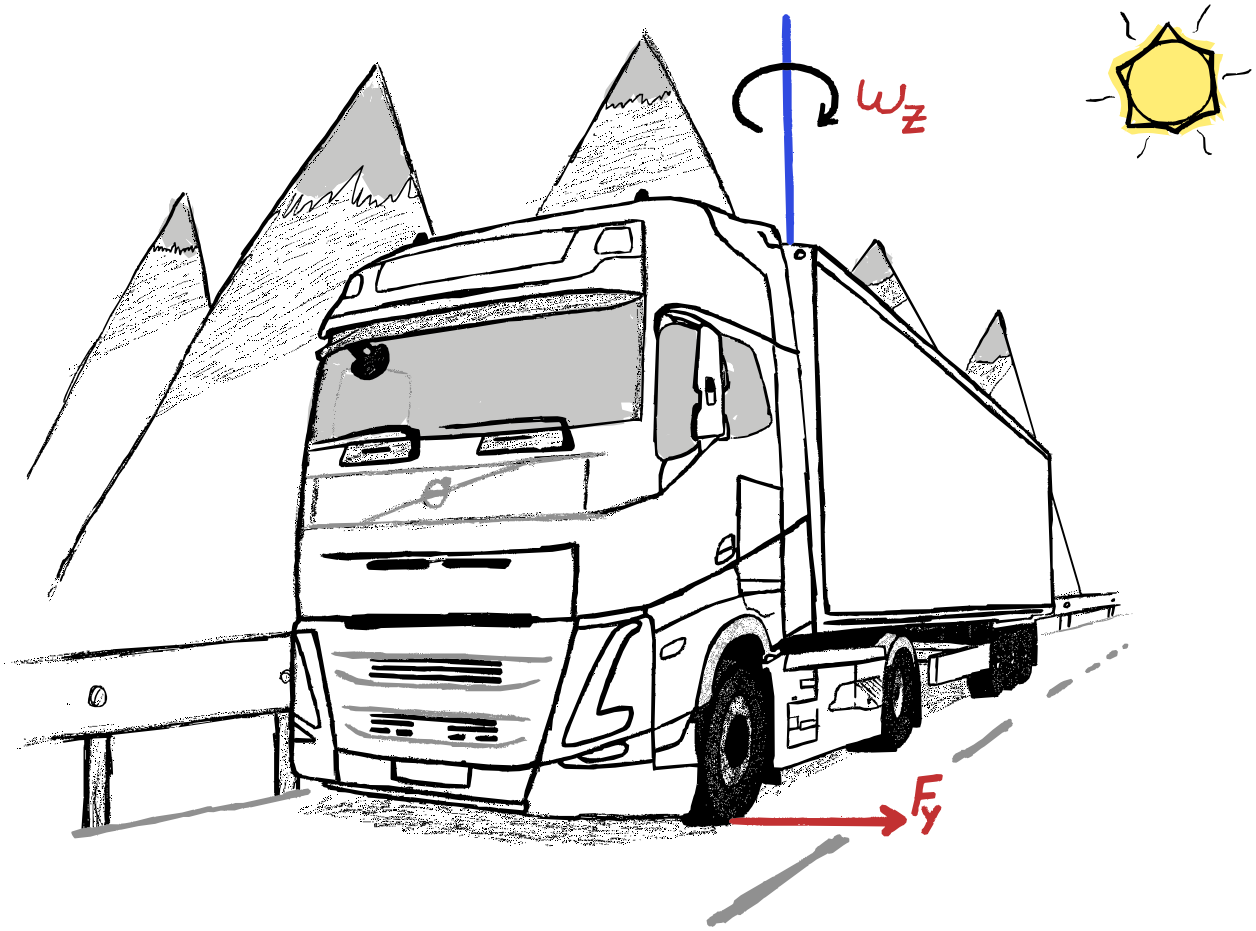

Online Tire Cornering Stiffness Estimation for Articulated Road Vehicles

Real-Time Estimation of Tire Cornering Stiffness in Articulated Vehicles using Unscented Kalman Filtering

Master's thesis in Systems, Control and Mechatronics & Complex Adaptive Systems

Syed Ahsan Ali Shah
Lucas Fosse

DEPARTMENT OF MECHANICS AND MARITIME SCIENCES
CHALMERS UNIVERSITY OF TECHNOLOGY
Gothenburg, Sweden 2026
www.chalmers.se

Master's thesis 2026

Online Tire Cornering Stiffness Estimation for Articulated Road Vehicles

Real-Time Estimation of Tire Cornering Stiffness in Articulated Vehicles using Unscented Kalman Filtering

Syed Ahsan Ali Shah
Lucas Fosse

CHALMERS
UNIVERSITY OF TECHNOLOGY

Department of Mechanics and Maritime Sciences
Division of Vehicle Engineering and Autonomous Systems
Chalmers University of Technology
Gothenburg, Sweden 2026

Online Tire Cornering Stiffness Estimation for Articulated Road Vehicles

Real-Time Estimation of Tire Cornering Stiffness in Articulated Vehicles using Unscented Kalman Filtering

Syed Ahsan Ali Shah
Lucas Fosse

Supervisor: Axel Ceder, Department of Electrical Engineering
Examiner: Mats Jonasson, Department of Mechanics and Maritime Sciences

Master's Thesis 2026
Department of Mechanics and Maritime Sciences
Division of Vehicle Engineering and Autonomous Systems
Chalmers University of Technology
SE-412 96 Gothenburg
Telephone +46 31 772 1000

AI Disclosure: LLMs have been used in this work to improve written language and to perform initial theoretical research. That's the extent to which artificial intelligence has been used in this project.

Cover: Tablet Drawing of a Volvo FH Aero Electric with Visuals for Lateral States

Typeset in LaTeX
Printed by Chalmers Reproservice
Gothenburg, Sweden 2026

Online Tire Cornering Stiffness Estimation for Articulated Road Vehicles

Joint State and Parameter Estimation using an Unscented Kalman Filter for Heavy Vehicle Applications

Syed Ahsan Ali Shah
Department of Systems, Control and Mechatronics
Chalmers University of Technology

Lucas Fosse
Department of Complex Adaptive Systems
Chalmers University of Technology

Abstract

This thesis investigates the real-time estimation of tire cornering stiffness for articulated heavy-duty vehicles using an Unscented Kalman Filter (UKF). Utilizing a simulation-based approach via IPG TruckMaker and Simulink, the study evaluates single-track, two-track, and articulated vehicle models under varying sensor availability and lateral excitation conditions. Results indicate a single-track, axle-level representation yields robust and convergent stiffness estimates for the tractor, whereas individual tire estimation seems to suffer from severe unobservability. The estimator demonstrates robustness to velocity sensor degradation by falling back on inertial and wheel speed data. Trailer cornering stiffness estimation exhibits steady-state errors attributed to unmodeled hitch dynamics. An observability-driven update strategy utilizing the local observability Gramian successfully restricts parameter updates to periods of sufficient lateral excitation.

Keywords: Vehicle dynamics; Tire Parameter; Slip Angle; State Space; Online Estimation; Observability; Bayesian filtering; Simultaneous State Parameter Estimation;

Acknowledgements

First and foremost, we would like to thank our supervisor **Axel Ceder** and our examiner **Mats Jonasson** for their invaluable guidance, constructive feedback, and continuous support throughout this thesis work. Their expertise and patience have been instrumental in shaping our master thesis.

We are also thankful to **Murrat Kumru** for the inspiring estimation and filtering lecture sessions, as well as **Nikhil Baliga**, **Gunna Sekhar Karri**, and the entire Motion Estimation and Vehicle Automation (MEVA) team at Volvo GTT for the discussions, for engaging us, for the collaborative spirit, and for creating a supportive environment that allowed us to remain focused and productive.

We are also thankful to our manager at Volvo, **Nicolas Andersson**, for providing the opportunity to conduct this thesis, for the trust and encouragement, and for regularly checking in to ensure we received the expected support.

We extend our appreciation to IPG for providing the license and for their patience and responsiveness throughout our email exchanges. Their willingness to answer questions and provide support has been very helpful for the completion of this work.

Finally, we would like to acknowledge Securitas Sverige for enduring our weekend retreats!

Thank you all!

Syed Ahsan Ali Shah, Lucas Fosse, Gothenburg, June 2026

Acronyms

ABS Anti-Lock Braking System.

ADAS Advanced Driver Assistance System.

CoG Center of Gravity.

ESC Electronic Stability Control.

IMU Inertial Measurement Unit.

INS Inertial Navigation System.

MEVA Motion Estimation and Vehicle Automation.

MUSE Multiple-Unit State Estimation.

NEES Normalized Estimation Error Squared.

SSA Side-Slip Angle.

TCS Tire Cornering Stiffness.

UKF Unscented Kalman Filter.

ZWGN Zero-Mean White Gaussian Noise.

Nomenclature

Below is the nomenclature of indices, subscripts, parameters, and variables that have been used throughout this thesis.

Indices

k	Index for discrete time step
t	Index for continuous time
i	Index for sigma points or singular values
j	Index for tractor wheels (FL, FR, RL, RR)
s	Index for trailer axles (1, 2, 3)

Subscripts

I	Inertial frame
B	Body frame
x, y, z	Coordinate axes
f	Front axle
r	Rear axle
FL	Front left wheel
FR	Front right wheel
RL	Rear left wheel
RR	Rear right wheel
tr	Trailer
$hitch$	Hitch point
$sens$	Sensor position
IMU	Inertial Measurement Unit position
COG	Center of gravity of tractor

COG_{tr}	Center of gravity of trailer
1	Front axle (trailer)
2	Middle axle (trailer)
3	Rear axle (trailer)

Parameters

m	Vehicle mass (tractor)
m_{tr}	Trailer mass
J_z	Yaw moment of inertia (tractor)
$J_{z,tr}$	Trailer yaw moment of inertia
R_w	Wheel radius
b	Track width (tractor)
b_{tr}	Track width (trailer)
l_f	Distance from COG to front axle (tractor)
l_r	Distance from COG to rear axle (tractor)
L	Wheelbase ($l_f + l_r$)
l_{hitch}	Distance from COG to hitch point (tractor)
$l_{f,tr}$	Distance from hitch to trailer COG
$l_{1,tr}$	Distance from trailer COG to front axle
$l_{2,tr}$	Distance from trailer COG to middle axle
$l_{3,tr}$	Distance from trailer COG to rear axle
L_{tr}	Trailer wheelbase (hitch to rear axle)
h_{COG}	COG height (tractor)
$h_{COG,tr}$	Trailer COG height
h_{hitch}	Hitch height (tractor)
$h_{hitch,tr}$	Hitch height (trailer)
g	Gravitational acceleration
C_f, C_r	Front and rear tire cornering stiffness (tractor, lumped)
C_j	Individual tire cornering stiffness (tractor)
$C_{r,tr}$	Trailer cornering stiffness
Q	Process noise covariance matrix
R	Measurement noise covariance matrix
T_s	Sampling time

n	State dimension
m	Measurement dimension
ϵ	Regularization term for slip angle calculation

UKF Parameters

W_0	Weight for first sigma point
W_i	Weight for remaining sigma points
γ	Scaling parameter for sigma points
λ	Unscented transform scaling parameter

Variables

x	State vector
z	Measurement vector
u	Control input vector
w	Process noise
v	Measurement noise
v_x, v_y	Longitudinal and lateral velocity (tractor)
ω_z	Yaw rate (tractor)
a_x, a_y	Longitudinal and lateral acceleration
δ	Steering angle (tractor)
δ_{FL}, δ_{FR}	Front left and right steering angles
ψ	Articulation angle (trailer relative to tractor)
$\omega_{z,tr}$	Trailer yaw rate
α	Tire slip angle
α_f, α_r	Front and rear tire slip angles (tractor, single-track)
α_j	Individual wheel slip angles (tractor)
$\alpha_{1,tr}$, $\alpha_{2,tr}$, $\alpha_{3,tr}$	Trailer axle slip angles
F_x, F_y	Longitudinal and lateral forces
F_{fy}, F_{ry}	Front and rear lateral tire forces (tractor, single-track)
$F_{y,j}$	Individual wheel lateral forces (tractor)
$F_{y,1,tr}$, $F_{y,2,tr}$, $F_{y,3,tr}$	Trailer axle lateral forces
F_{hx}, F_{hy}, F_{hz}	Longitudinal, lateral and vertical hitch forces (tractor frame)

$F_{hx,tr}$, $F_{hy,tr}$, $F_{hz,tr}$	Longitudinal, lateral and vertical hitch forces (trailer frame)
F_{fz}	Vertical load on tractor front axle
F_{rz}	Vertical load on tractor rear axle
$F_{z,axle}$	Vertical load per trailer axle
T_{RL}, T_{RR}	Rear left and right wheel torques
ω_{RL}, ω_{RR}	Rear left and right wheel speeds (tractor)
ω_{FL}, ω_{FR}	Front left and right wheel speeds (tractor)
$\omega_{2,tr}$	Trailer middle left and right wheel speeds
$\mathbf{v}$	Velocity vector
$\boldsymbol{\omega}$	Angular velocity vector
$\mathbf{r}$	Position vector
$\mathbf{R}(\delta)$	Rotation matrix
μ	State mean vector
μ_k^-	Predicted mean vector
μ_k	Estimated mean vector
P	State covariance matrix
P_k^-	Predicted covariance matrix
P_k	Estimated covariance matrix
$\chi^{(i)}$	Sigma points
$\mathcal{Z}^{(i)}$	Predicted measurement sigma points
K_k	Kalman gain
S_k	Innovation covariance matrix
C_k	Cross covariance matrix
$\hat{x}_k$	Estimated state vector
$\hat{z}_k$	Predicted measurement mean

Contents

List of Acronyms viii

Nomenclature x

List of Figures xix

List of Tables xxiii

1 Introduction 1
- 1.1 Purpose . . . 2
- 1.2 Scope . . . 2
- 1.3 Main Research Questions . . . 3
- 1.4 Social and Ethical Aspects . . . 4

2 Theory 5
- 2.1 Reference Frames and Rigid Body Kinematics . . . 5
  - 2.1.1 Time Derivatives in Rotating Frames . . . 5
  - 2.1.2 Rotation Matrices . . . 5
- 2.2 Velocity and Acceleration Transformations . . . 6
  - 2.2.1 Velocity Transformation . . . 7
  - 2.2.2 Acceleration Transformation . . . 7
  - 2.2.3 IPG TruckMaker Reference Frames . . . 7
- 2.3 Tire Mechanics and Force Generation . . . 8
  - 2.3.1 Contact Patch Mechanics and Force Development . . . 9
  - 2.3.2 Lateral Tire Force . . . 10
    - 2.3.2.1 Slip Angle . . . 10
    - 2.3.2.2 Influence of Load, Inflation Pressure and Tire Geometry 12
- 2.4 Introduction to Vehicle Dynamics . . . 13
  - 2.4.1 Axis and Coordinate Systems . . . 14
  - 2.4.2 Single-Track Model . . . 15
  - 2.4.3 Tire Slip and Kinematics . . . 16
  - 2.4.4 The State-Space Form . . . 16
  - 2.4.5 Limitations of the Linear Single-Track Model . . . 17
- 2.5 Estimation and Bayesian Filtering . . . 17
  - 2.5.1 State-Space Representation with Uncertainty . . . 18

2.5.1.1 Prediction step . . . 18
2.5.1.2 Update step . . . 19
2.5.1.3 Recursive structure . . . 19
2.5.2 Gaussian Assumption . . . 19
2.5.3 The Unscented Kalman Filter (UKF) . . . 20
2.5.3.1 Unscented Transform . . . 20
2.5.3.2 Prediction Step . . . 21
2.5.3.3 Measurement Prediction . . . 21
2.5.3.4 Update Step . . . 21
2.5.3.5 Interpretation . . . 22
2.5.3.6 Application to Vehicle Dynamics . . . 22
2.5.4 Filter Consistency . . . 22
2.5.4.1 Normalized Estimation Error Squared (NEES) . . . 22
2.6 Local Observability Gramian . . . 23
2.6.1 Quantifying Observability . . . 25
2.6.2 Discrete Time Formulation . . . 25
2.6.3 Relation to the Observability Matrix . . . 26

3 Method **27**
3.1 Estimation using Experimental Data . . . 27
3.1.1 MUSE . . . 27
3.1.2 Modified One-Track Model . . . 29
3.1.2.1 Modeling Assumptions . . . 30
3.1.2.2 State and Parameter Definitions . . . 30
3.1.2.3 Control Inputs . . . 31
3.1.2.4 Measurement Signals . . . 31
3.1.2.5 Vehicle Kinematics and Slip Angles . . . 32
3.1.2.6 Force Generation . . . 33
3.1.2.7 Equations of Motion . . . 33
3.1.2.8 Wheel Speed Measurements . . . 34
3.2 Estimation using Simulated Data . . . 34
3.2.1 TruckMaker and Simulink . . . 34
3.2.2 Measurement Noise . . . 35
3.2.3 Truck Model . . . 35
3.2.4 Trailer Model . . . 36
3.2.5 Driving Scenario . . . 36
3.3 Tractor Dynamics Filter Implementation . . . 37
3.3.1 Addtional Modeling Assumptions . . . 37
3.3.2 Stochastic State-Space Model . . . 37
3.3.3 State, Input and Measurement Definitions . . . 38
3.3.3.1 State Vector . . . 38
3.3.3.2 Control Inputs . . . 39
3.3.3.3 Measurement Signals . . . 39
3.3.3.4 Constant Parameters . . . 40
3.3.4 Vehicle Kinematics and Dynamics . . . 40
3.3.4.1 Equations of Motion . . . 41

3.3.4.2 Velocity Transformation and Slip Angle Calculation . 41
3.3.4.3 Longitudinal Force 43
3.3.4.4 Dynamic Load Transfer 43
3.3.4.5 Lateral Tire Forces 44
3.3.4.6 UKF Prediction Step 44
3.3.5 Measurement Model 45
3.3.5.1 IMU Acceleration Model 45
3.3.5.2 Velocity Measurements 45
3.3.5.3 Wheel Speed Measurements 45
3.3.5.4 Complete Measurement Function 46
3.3.5.4.1 Full Measurement Set 46
3.3.5.4.2 Reduced Measurement Set 46
3.3.5.5 Measurement Prediction 46
3.3.6 UKF Update Step 47
3.4 UKF Update Stragety 47
3.4.1 Implementation of Observability Indicator 48
3.4.2 Conditional Update of Stiffness Parameters 49
3.4.3 Quantifying Stiffness Error Propagation 49
3.5 Estimation of Individual Tire Stiffness 49
3.5.1 State Vector and Control Inputs 50
3.5.2 Wheel Kinematics and Forces 51
3.5.3 Equations of Motion 52
3.5.4 Measurement Model 52
3.6 Extension to Tractor-Trailer Configuration 53
3.6.1 Additional States 53
3.6.2 Modified Control Inputs 54
3.6.3 Additional Measurements 54
3.6.4 New Constant Parameters 54
3.6.5 Hitch Coupling 55
3.6.6 Modified Tractor Dynamics 55
3.6.7 Modified Normal Forces on the Tractor 55
3.6.8 Trailer Kinematics and Dynamics 56
3.6.8.1 Hitch Velocity Transformation 56
3.6.8.2 Trailer Axle Velocities and Slip Angles 56
3.6.8.3 Trailer Load Transfer 57
3.6.8.4 Trailer Lateral Forces 57
3.6.8.5 Lateral Hitch Force 57
3.6.8.6 Trailer Dynamics 57
3.6.8.7 Trailer Wheel Speed Measurements 58
3.6.9 Discretization 58
3.6.9.1 Consistency Evaluation Using NEES 59

4 Results **61**
4.1 MUSE Results 61
4.2 One Track Tractor Model Results 66
4.2.1 Estimation with Degraded Sensing Conditions 66

4.2.2 Estimate Comparison Between Sensing Conditions 75
4.2.3 Varying Lateral Dynamics 77
4.2.3.1 Steady-State Circle with Fixed Speed Limit 77
4.2.3.2 Variable Speed Limits 83
4.2.4 Observability-Driven Update Strategy 88
4.3 Stiffness Estimation Error Propagation 92
4.4 Two-Track Model Estimation Results 94
4.5 Truck and Trailer Estimation Results 96

5 Discussion **111**
5.1 Model Complexity and Observability 111
5.2 Excitation Dependency and Update Strategy 111
5.3 Reality and the Non-Linear Assumption 112
5.4 Articulated Dynamics and Filter Consistency 112
5.5 Sensor Degradation and System Resilience 112
5.6 Future Work 113
5.6.1 Nonlinear Tire Models 113
5.6.2 Stiffness Lookup Tables 113
5.6.3 Extended Experimental Validation 113
5.6.4 Extension to Alternative Vehicle Configurations 114

6 Conclusion **115**

References **117**

Appendix A Additional Results **I**
A.1 TwoTrack Model I
A.2 One Track Model Nonlinearity III

List of Figures

2.1 TruckMaker coordinate systems 8
2.2 Pressure Distribution 9
2.3 Friction generation mechanisms 9
2.4 Illustrations of the tire contact patch and related relations 10
2.5 Side slip angle 11
2.6 Tire tread deformation and resultant lateral force 11
2.7 Side Slip Angle vs Lateral Force 12
2.8 Vertical load vs Cornering Stiffness 12
2.9 Illustration of the One-Track Model 16
2.10 State Space Deviations 24

3.1 MUSE Project Structure 27
3.2 Planar projection of the experimental data vehicle trajectory 28
3.3 Illustration of the One-Track Vehicle Model 29
3.4 TruckMaker Project Structure 34
3.5 Illustration of the simulated road scenario 37
3.6 Illustration of simplified longitudinal load transfer 42
3.7 Simulink block layout for filter update strategy 47
3.8 Sliding window working principle 48
3.9 The two-track model with individual cornering stiffness per wheel . . 50
3.10 The single-track vehicle model, extended to a trailer configuration. . . 53

4.1 Experimental estimation results for a_x 62
4.2 Experimental estimation results for a_y 62
4.3 Experimental estimation results for v_x 63
4.4 Experimental estimation results for v_y 63
4.5 Experimental estimation results for ω_z 64
4.6 Experimental estimation results for thelumped cornering stiffness C_f 65
4.7 Experimental estimation results for the lumped cornering stiffness C_r 65
4.8 Longitudinal acceleration a_x, estimate vs. reference 66
4.9 Lateral acceleration a_y, estimate vs. reference 67
4.10 Yaw acceleration, estimate vs. reference 68
4.11 Longitudinal velocity v_x, estimate vs. reference 68
4.12 Lateral velocity v_y, estimate vs. reference 69
4.13 Yaw rate, estimate vs. reference 70
4.14 Lumped cornering stiffness C_f, estimate vs. reference 71

4.15 Lumped cornering stiffness C_r, estimate vs. reference 71
4.16 Tractor longitudinal velocity estimation error 72
4.17 Tractor lateral velocity estimation error 72
4.18 Tractor yaw rate estimation error 73
4.19 Tractor estimator NEES consistency test 74
4.20 Tractor estimator NEES distribution, empirical vs. theoretical 74
4.21 Tractor local observability singular value analysis 75
4.22 Tractor estimator sensor degradation comparison for v_x 76
4.23 Tractor estimator sensor degradation comparison for v_y 76
4.24 Tractor estimator sensor degradation comparison for ω_z 77
4.25 Tractor stiffness and observability metric in steady-state at $20\,\mathrm{km\,h^{-1}}$ 78
4.26 Tractor stiffness and observability metric in steady-state at $30\,\mathrm{km\,h^{-1}}$ 79
4.27 Tractor stiffness and observability metric in steady-state at $40\,\mathrm{km\,h^{-1}}$ 80
4.28 Tractor stiffness and observability metric in steady-state at $50\,\mathrm{km\,h^{-1}}$ 81
4.29 Tractor stiffness and observability metric in steady-state at $60\,\mathrm{km\,h^{-1}}$ 82
4.30 Tractor front stiffness estimate at increasing v_x 83
4.31 Tractor rear stiffness estimate at increasing v_x 83
4.32 Local Gramian observability metric at increasing v_x 84
4.33 Tractor front stiffness estimate at decreasing v_x 85
4.34 Tractor rear stiffness estimate at decreasing v_x 85
4.35 Local Gramian observability metric at decreasing v_x 86
4.36 Tractor front stiffness estimate with update strategy 88
4.37 Tractor rear stiffness estimate with update strategy 89
4.38 Tractor front stiffness estimate at increasing v_x with update strategy . 90
4.39 Tractor rear stiffness estimate at increasing v_x with update strategy . 90
4.40 Tractor front stiffness estimate at decreasing v_x with update strategy 91
4.41 Tractor rear stiffness estimate at decreasing v_x with update strategy . 92
4.42 Truck v_y estimates for various constant cornering stiffness values . . . 93
4.43 Truck a_y estimates for various constant cornering stiffness values . . . 93
4.44 Two-Track model stiffness estimate C_{FL} 94
4.45 Two-Track model stiffness estimate C_{FR} 95
4.46 Two-Track model stiffness estimate C_{RL} 95
4.47 Two-Track model stiffness estimate C_{RR} 96
4.48 Truck & Trailer estimator, evaluation of a_x 97
4.49 Truck & Trailer estimator, evaluation of a_y 97
4.50 Truck & Trailer estimator, evaluation of ω_z 98
4.51 Truck & Trailer estimator, evaluation of $\dot{\omega}_z$ 98
4.52 Truck & Trailer estimator, evaluation of v_x 99
4.53 Truck & Trailer estimator, evaluation of v_y 100
4.54 Truck & Trailer estimator, evaluation of ω_z 100
4.55 Truck & Trailer estimator, evaluation of C_f 101
4.56 Truck & Trailer estimator, evaluation of C_r 102
4.57 Truck & Trailer estimator, evaluation of ψ 102
4.58 Truck & Trailer estimator, evaluation of $\omega_{z,tr}$ 103
4.59 Truck & Trailer estimator, evaluation of $C_{r,tr}$ 104
4.60 Coupled tractor longitudinal velocity estimation error 104

4.61 Coupled tractor lateral velocity estimation error 105
4.62 Coupled tractor yaw rate estimation error 105
4.63 Truck & Trailer, NEES consistency test 106
4.64 Truck & Trailer, NEES distribution, empirical vs. theoretical 106
4.65 Articulation angle estimation error 107
4.66 Trailer yaw rate 108
4.67 Trailer NEES consistency test 108
4.68 Trailer NEES distribution, empirical vs. theoretical 109

A.1 Two-Track model estimate and reference for v_x I
A.2 Two-Track model estimate and reference for v_y II
A.3 Two-Track model estimate and reference for ω_z II
A.4 Truck front stiffness estimate in circle driving $50\,\mathrm{km\,h^{-1}}$ to $60\,\mathrm{km\,h^{-1}}$ III
A.5 Truck rear stiffness estimate in circle driving $50\,\mathrm{km\,h^{-1}}$ to $60\,\mathrm{km\,h^{-1}}$. III
A.6 Truck long. vel. estimate in circle driving $50\,\mathrm{km\,h^{-1}}$ to $60\,\mathrm{km\,h^{-1}}$ . . IV
A.7 Truck yaw rate estimate in circle driving $50\,\mathrm{km\,h^{-1}}$ to $60\,\mathrm{km\,h^{-1}}$ . . . IV

List of Tables

3.1 MUSE model state vector definition 30
3.2 MUSE model process noise matrix 31
3.3 MUSE model vehicle parameters 31
3.4 Control input signals used by the MUSE model 31
3.5 Measurements used by the MUSE model 31
3.6 MUSE model measurement noise matrix 32
3.7 Physical properties of the truck model 35
3.8 Physical properties of the trailer model 36
3.9 State vector definition with initial values. 38
3.10 Process noise matrix Q and its values. 38
3.11 Control input signals from IPG TruckMaker 39
3.12 Available sensors and measurement signals 39
3.13 Measurement noise matrix R and its values. 39
3.14 Constant vehicle parameters 40
3.15 Control inputs for the four-wheel model 51
3.16 Additional states introduced by the trailer 53
3.17 Modified control input signals from IPG TruckMaker 54
3.18 Additional measurement signals from the trailer 54
3.19 Additional constant parameters for the trailer 55

4.1 Steady-state lateral acceleration during varying speed limits 86
4.2 Steady-state side-slip angles and vertical force during varying speed . 87

1

Introduction

Road vehicles are an essential component of modern transportation systems and are used extensively in daily life for both personal and commercial purposes [1], [2]. In the case of heavy-duty commercial vehicles, such as trucks with trailers, vehicle operation is characterized by continuously varying loading conditions. The total mass and mass distribution of such vehicles depend on the carried payload, which can change constantly between trips and even during operation [1], [3]. These variations have a strong influence on vehicle dynamics and represent a major challenge for vehicle control and safety systems.

Over the past years, increasing attention has been directed toward autonomous driving and advanced driver assistance systems (ADASs) for commercial vehicles [4]. These technologies promise to improve road safety, enhance transport efficiency, and reduce operational costs [3]. Over several decades, extensive research has been conducted in the field of intelligent vehicles and intelligent vehicle–highway systems [5]. This research has led to the development of a wide range of vehicle control systems, including collision avoidance, collision warning systems, adaptive cruise control, automated lane keeping, as well as braking and stability-related systems such as anti-lock braking system (ABS) and electronic stability control (ESC) [1], [4], [5].

The main objective of modern vehicle control systems is to maintain vehicle stability by minimizing deviations between the actual vehicle states and their desired values. For example, ESC systems actively regulate the yaw motion of the vehicle to prevent lateral instability and have been shown to significantly reduce loss-of-control accidents [1], [6]. Similarly, ABS improves vehicle safety by preventing wheel lock-up during emergency braking situations [1]. The performance of these systems strongly depends on the availability of accurate and reliable vehicle state information.

Advanced vehicle control strategies, such as model predictive control and sliding mode control, have been proposed to further enhance vehicle stability and handling performance [6], [7]. However, the implementation of such advanced methods requires accurate knowledge of key vehicle states and parameters. While certain quantities, such as yaw rate, can be measured directly using low-cost inertial sensors, other important parameters, such as side-slip angle (SSA) and tire cornering stiffness (TCS), cannot be obtained directly using standard in-vehicle sensors.

Among the most critical parameters influencing vehicle stability are the vehicle SSA

and TCS. The vehicle SSA, defined as the angle between the vehicle velocity vector and its longitudinal axis, cannot be directly measured without expensive external sensors such as high-precision GPS systems [6], [7], [8]. Tire cornering stiffness, which describes the relationship between lateral tire force and tire slip angle, is another key parameter that significantly affects lateral vehicle dynamics. This parameter varies with factors such as vehicle load, tire properties, and road conditions, making real-time measurement or identification particularly challenging.

For articulated vehicles, such as trucks with trailers, these challenges are further amplified due to the complex dynamic interaction between the tractor and the trailer. Accurate estimation of tire cornering stiffness for both longitudinal and lateral directions is therefore essential for improving vehicle modeling, control system design, and overall driving safety.

1.1 Purpose

The purpose of this master's thesis is to develop and evaluate an online estimation framework for tire cornering stiffness for an articulated heavy-duty vehicle consisting of a truck and a trailer. Tire cornering stiffness is a key parameter in lateral vehicle dynamics and has a significant impact on vehicle stability, handling performance, and the effectiveness of advanced vehicle control systems.

The thesis aims to investigate whether reliable estimation of tire cornering stiffness can be achieved at the axle level using only standard in-vehicle sensor information, under realistic operating conditions. Particular emphasis is placed on articulated vehicle dynamics and the challenges introduced by varying loading conditions and tractor–trailer interactions.

To achieve this purpose, a simulation-based approach is adopted using IPG TruckMaker to generate controlled, repeatable driving scenarios. An online estimation strategy is employed to ensure real-time applicability, making the proposed approach relevant for vehicle control and monitoring systems. The influence of driving maneuver aggressiveness, lateral excitation, and parameter update strategy on estimation performance is systematically analyzed.

The overall goal is to provide insights into the feasibility, limitations, and practical applicability of online tire cornering stiffness estimation for articulated heavy-duty vehicles, thereby contributing to improved vehicle modeling and control-oriented parameter estimation.

1.2 Scope

The study focuses on longitudinal and lateral dynamics and considers TCS as a constant parameter. Estimation of axle stiffness captures the effects of the suspension system as well as other elastic axle components, while allowing for a more simple vehicle model. Combined slip effect and non-linear tire behavior are outside of the

scope of this work. The estimation framework will rely on the available measurements rather than the high precision measurement equipment.

Due to absence of experimental tire testing equipment and confidentiality of data, the true physical TCS is not available for neither individual tires nor for a combined axle stiffness. TCS provided by the simulation environment per wheel will be used as reference data for validation purposes.

1.3 Main Research Questions

The primary objective of this work is to estimate the TCS including the entire system stiffness of an articulated heavy-duty vehicle consisting of a truck and a trailer. TCS is a key parameter in lateral vehicle dynamics, as directly influences tire force generation, vehicle stability, and handling performance. Accurate knowledge of this parameter is essential for the design and performance of advanced vehicle control systems.

It is assumed that the vehicle is equipped with vehicle sensors, such as steering angle sensor, velocity sensor or GPS, wheel speed sensors, and an inertial measurement unit (IMU) providing yaw rate and acceleration. Direct measurements of tire forces, tire slip angle and vehicle side-slip angle are not available. Furthermore, the vehicle operates under varying sensor availability conditions.

The articulated nature of the vehicle introduces additional complexity compared to a single unit vehicle. The dynamic interaction between the tractor and the trailer, as well as articulation angle between them, significantly influences lateral dynamic and tire force distribution. As a consequence, estimations methods developed for passenger cars cannot be applied directly without modification.

The problem addressed in this thesis/work can therefore be stated as follows:

- Estimation level: Is it feasible to estimate tire cornering stiffness at an individual tire level for an articulated vehicle, or is estimation at a simplified axle level appropriate and reliable with the assumed/given measurements mentioned above?

- Excitation requirement: What level of driving aggressiveness and lateral excitation is required to ensure a reliable estimation of tire cornering stiffness? In particular, which types of driving maneuvers provide sufficient information for parameter identification, since straight-line driving does not excite lateral tire dynamics?

- Parameter update strategy: Assuming that tire cornering stiffness is a slowly varying parameter, how frequently should the parameter be updated in an online estimation framework under changing operating conditions?

- Robustness of Estimation Algorithm: How robust is the estimation algorithm when primary velocity measurements become unavailable or degraded?

In this thesis, an online estimation framework is adopted to ensure real-time applicability in vehicle control and monitoring systems. The research questions listed above guide the methodological choices and evaluation criteria used throughout the thesis.

1.4 Social and Ethical Aspects

The project will rely on simulated or anonymized vehicle data, ensuring full compliance with Volvo's data ethics guidelines. No personal data will be used, and no safety-critical experiments will be conducted. Ethical considerations include transparent reporting of assumptions, model limitations, and avoiding overgeneralized conclusions beyond the scope of the data.

Enhanced online tire estimation can also contribute to sustainability by improving several aspects, as listed below:

- **Energy Efficiency:** Accurate traction control reduces unnecessary tire slip and energy loss.
- **Safety:** Improved slip estimation enhances stability and braking performance, especially for heavy multi-trailer vehicles. Even vehicle control accidents can be reduced by 27% from reducing lateral instability which can lower the risk of losing control of the vehicle [1].
- **Material Efficiency:** Better tire force control extends tire lifespan, reducing waste and lowers the environmental impact.

This work supports the UN Sustainable Development Goals 9 (Industry, Innovation, and Infrastructure), 11 (Sustainable Cities and Communities) and 13 (Climate Action).

2

Theory

The following chapter establishes the mathematical and physical foundation required to understand the lateral dynamics of vehicles and the stochastic nature of parameter estimation. It also lays the foundation for understanding the metrics used to quantify the estimation results.

2.1 Reference Frames and Rigid Body Kinematics

The motion of a rigid body, such as a vehicle chassis, can be described using multiple reference frames [9]. Two primary frames are commonly used in vehicle dynamics:

- **Inertial frame (I):** A fixed, non-accelerating coordinate system attached to the ground. Newton's laws hold in this frame without modification [10].
- **Body-fixed frame (B):** A coordinate system attached to the vehicle's body, moving with the vehicle [11].

These frames provide the foundation for expressing kinematic quantities such as positions, velocities, and accelerations, as well as dynamic quantities like forces and moments. To reconstruct the vehicle trajectory in an inertial reference frame, the time history of the body-fixed state must be transformed accordingly [11].

2.1.1 Time Derivatives in Rotating Frames

When a vector $\mathbf{x}$ is expressed in a rotating frame, its time derivative differs from that in an inertial frame. For a body-fixed frame rotating with angular velocity $\boldsymbol{\omega}$ relative to the inertial frame, the relationship is [12]:

$$\left(\frac{d\mathbf{x}}{dt}\right)_I = \left(\frac{d\mathbf{x}}{dt}\right)_B + \boldsymbol{\omega} \times (\mathbf{x})_B \tag{2.1}$$

2.1.2 Rotation Matrices

The orientation of the body frame relative to the inertial frame can be represented using a rotation matrix. For full three-dimensional motion, the orientation is com-

monly described using Euler angles (yaw ϕ, pitch θ, roll ψ), leading to a combined rotation matrix [13]:

$$R(\phi, \theta, \psi) = R_x(\psi)\, R_y(\theta)\, R_z(\phi) \tag{2.2}$$

where

$$R_x(\psi) = \begin{bmatrix} 1 & 0 & 0 \\ 0 & \cos\psi & \sin\psi \\ 0 & -\sin\psi & \cos\psi \end{bmatrix}, \tag{2.3}$$

$$R_y(\theta) = \begin{bmatrix} \cos\theta & 0 & -\sin\theta \\ 0 & 1 & 0 \\ \sin\theta & 0 & \cos\theta \end{bmatrix}, \tag{2.4}$$

$$R_z(\phi) = \begin{bmatrix} \cos\phi & \sin\phi & 0 \\ -\sin\phi & \cos\phi & 0 \\ 0 & 0 & 1 \end{bmatrix}. \tag{2.5}$$

The order of multiplication matters. Rotating first about z (yaw), then y (pitch), then x (roll) gives a different orientation than any other order [14]. Euler angles are not commutative, so the rotation sequence must be clearly defined to avoid inconsistencies.

A vector expressed in the body frame, $\mathbf{v}_B$, can be transformed to the inertial frame as:

$$\mathbf{v}_I = R(\phi, \theta, \psi)\, \mathbf{v}_B, \tag{2.6}$$

and conversely:

$$\mathbf{v}_B = R^T(\phi, \theta, \psi)\, \mathbf{v}_I. \tag{2.7}$$

2.2 Velocity and Acceleration Transformations

The motion of a rigid body can be decomposed into a translation of a reference point and a rotation about that point, according to Chasles' theorem [14]. In three-dimensional space, this motion is fully described by the position of the reference point and the angular velocity of the body.

Given these quantities, the velocity and acceleration at any point on the rigid body can be determined using rigid body kinematics. These relations are fundamental for describing motion at different locations on a body and are used extensively in both the dynamic model and the measurement equations.

2.2.1 Velocity Transformation

The velocity of any point P on a rigid body can be expressed in terms of the velocity of a reference point, $\mathbf{r_p}$, and the body's angular velocity:

$$\mathbf{v}_P = \mathbf{v}_{r_p} + \boldsymbol{\omega} \times \mathbf{R_p} \tag{2.8}$$

where $\boldsymbol{\omega}$ is the angular velocity of the body, and $\mathbf{R_p}$ is the position vector from the reference point, $\mathbf{r_p}$, to point P [14], [15].

2.2.2 Acceleration Transformation

Similarly, the acceleration of a point P is given by

$$\mathbf{a}_P = \mathbf{a}_{r_p} + \dot{\boldsymbol{\omega}} \times \mathbf{R_p} + \boldsymbol{\omega} \times (\boldsymbol{\omega} \times \mathbf{R_p}), \tag{2.9}$$

where $\dot{\boldsymbol{\omega}}$ is the angular acceleration of the body.

The second term represents contributions from angular acceleration, while the third term accounts for centripetal (rotational) acceleration. These expressions are fundamental for describing rigid body motion in the body-fixed frame and form the basis for dynamic modeling [11], [14], [15].

2.2.3 IPG TruckMaker Reference Frames

The simulation environment IPG TruckMaker utilizes multiple reference frames to streamline object parametrization and kinematic calculations. Unless otherwise stated, the definitions of the four relevant frames follow the software reference manual [16]:

- **Fr0**: "Frame zero" is the inertial reference frame with an earth-fixed origin. This corresponds to the inertial frame (I) described previously in section 2.1.
- **Fr1**: A body-fixed reference frame accompanying all moving objects, tracking all localized translations and rotations. Fr1 is the body frame (B) from section 2.1, but differs in that the origin is not the center of gravity (CoG). The origin is located behind the vehicle for trucks, and in front of the vehicle for trailers.
- **Fr2**: The wheel carrier reference frame. It represents a pure translation from its associated mount point in Fr1. The x-axis denotes the forward driving direction, the y-axis is the wheel spin axis (directed left), and $z = x \times y$.
- **FrW**: Originates at the tire-road contact point. The x-axis aligns with the intersection of the tire's vertical plane and the road's tangent plane. The y-axis points left, orthogonal to x within the road's tangent plane, and $z = x \times y$.

Figure 2.1 illustrates the relations between Fr0, Fr1 and Fr2. The illustration depicts an idealized standstill condition with zero camber and caster, placing the tire-road contact point directly below the Fr2 origin. Under these constraints, the Fr2 frames align with their corresponding FrW frames in the top-down projection shown in the figure.

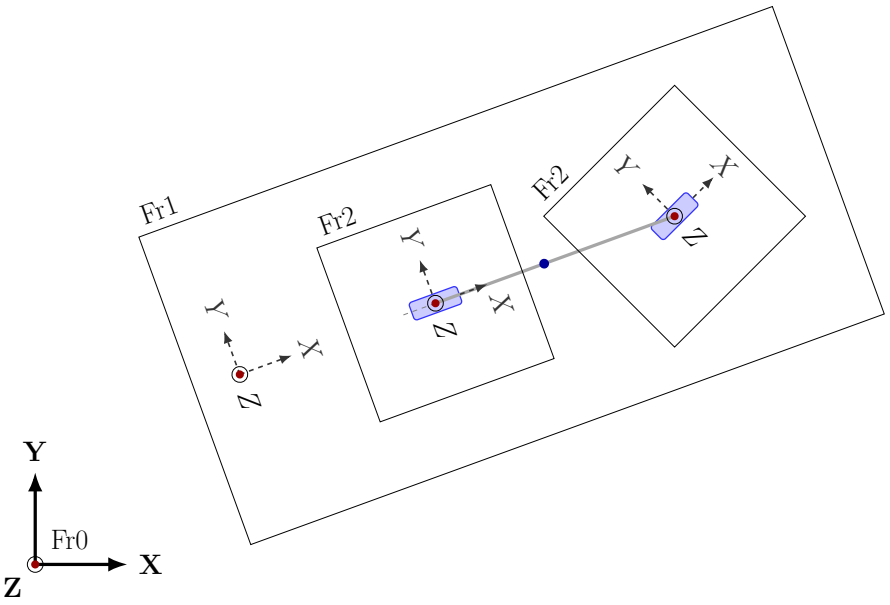

Figure 2.1: Relative positioning of the TruckMaker coordinate systems. Although TruckMaker utilizes multi-track vehicle models, a bicycle model is depicted for visual clarity. Fr2 and FrW effectively coincide at standstill.

2.3 Tire Mechanics and Force Generation

The tire is the sole interface between the vehicle and the road surface, responsible for generating almost all primary control and disturbance forces, with the exception of aerodynamics [17], [18]. The critical forces determining a vehicle's performance in braking, acceleration, and cornering are developed in four contact patches, each typically no larger than a human hand.

According to the classical framework established in vehicle dynamics, the tire serves three fundamental functions: producing longitudinal forces for acceleration and braking control, and creating lateral forces to maintain directional stability and enable cornering. [17], [19].

Although a tire is fundamentally a viscoelastic toroid, modern optimization makes it a complex nonlinear system that is difficult to model accurately [17], [19]. Many simplified tire models have been created to represent different performance aspects, but for understanding their role in vehicle dynamics, measured data is enough to capture the essential properties [17], [20], [21].

Structurally, the tire consists of a flexible carcass (main structural body of the tire) made of high-strength cords, anchored to the rim by steel beads[17]. Internal air pressure induces stresses such that deformation from external forces generates reaction forces, with behavior depending on both operating conditions and construction type.

2.3.1 Contact Patch Mechanics and Force Development

Tire forces are not applied at a single point but are the result of distributed normal and shear stresses in the contact patch [17]. Because the pressure distribution is uneven, as illustrated in figure 2.2, it shifts toward the front during rolling, which creates rolling resistance and the resultant force does not pass through the wheel center. Longitudinal and lateral forces are generated through shear as tread elements deform while passing through the contact area.

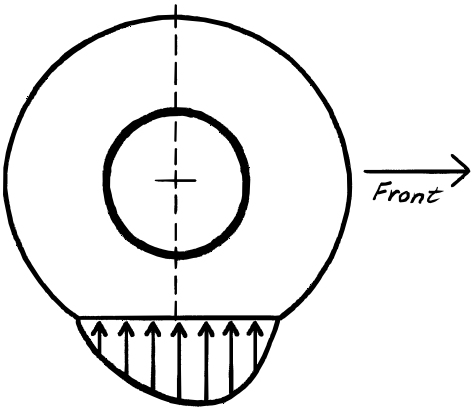

Figure 2.2: Tire internal air pressure distribution during rolling state.

The friction generated between the tire and the road surface is primarily governed by two physical mechanisms: adhesion and hysteresis. Surface adhesion is caused by molecular interactions between the tire rubber and the road aggregate, whereas hysteresis results from internal energy losses in the rubber during cyclic deformation as the tire passes over road surface asperities [17], [22]. These mechanisms are illustrated in figure 2.3.

Both mechanisms require a small amount of slip at the interface. During braking and acceleration, additional slip occurs due to tread deformation, illustrated in figure 2.4a where tread elements build up and release force across the contact patch. The friction force increases with slip up to a peak value and then decreases toward full lockup.

Tire performance depends on several factors, including vertical load, inflation pressure, surface condition, and speed. When a tread element first enters the tire-road contact patch, it cannot generate significant friction force because the rubber is

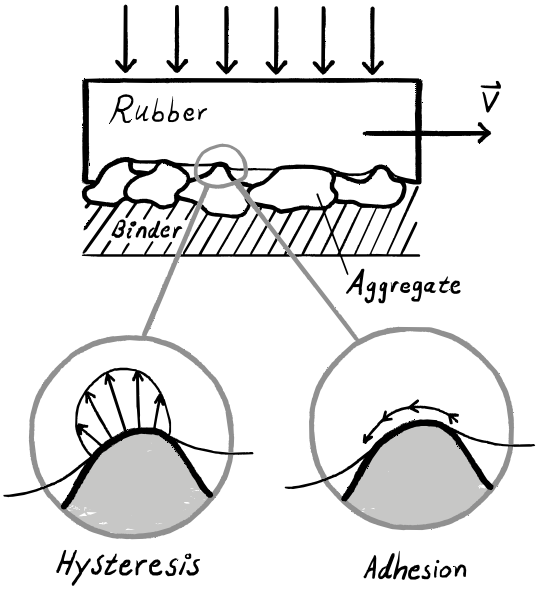

Figure 2.3: The two primary mechanisms contributing to tire-road friction.

compliant and must deform before shear forces can build up [17]. As the wheel continues to roll, the deformations of the tread element increases together with the vertical load, which allows the friction force to grow progressively. Near the rear of the contact patch, however, the vertical load decreases and the tread element begins to slide relative to the road surface. This causes the friction force to diminish gradually until it reaches zero as the tread leave the contact region. An increase in vertical load generally allows larger friction force to develop, as illustrated in figure 2.4b, while wet conditions and higher speeds further reduce grip [23]. The road surface texture also plays a significant role, meaning that friction is a property of the tire and road system rather than the tire alone.

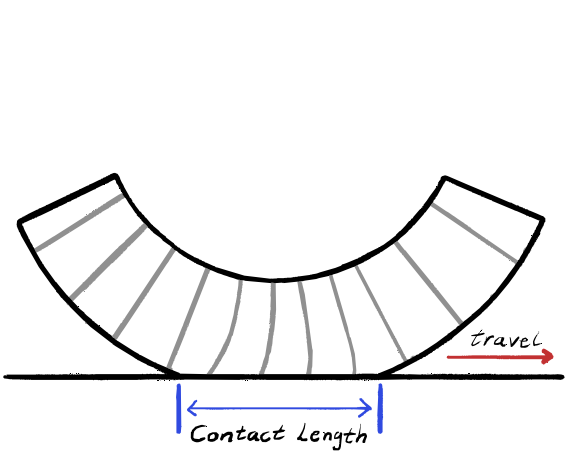

(a) Tire tread deformation in contact patch during acceleration and braking.

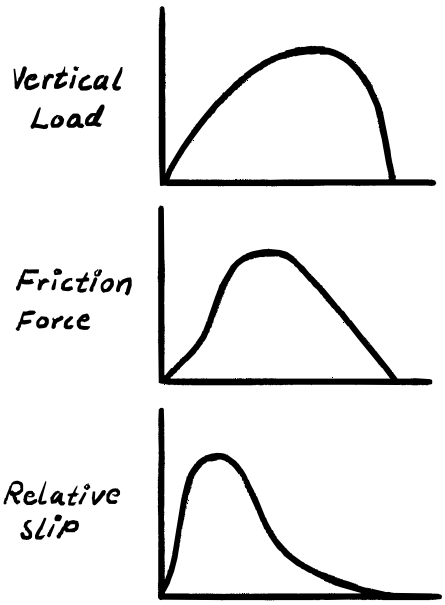

(b) A brief illustration of a relation between vertical load, slip and friction coefficient.

Figure 2.4: Illustrations of the tire contact patch and the related relations vertical load, friction force and relative slip. The horizontal axis in (b) shows position along the contact patch in (a).

2.3.2 Lateral Tire Force

During cornering, lateral tire forces are generated through mechanisms similar to those responsible for longitudinal traction and braking forces. However, instead of longitudinal slip, the dominant effect is the lateral deformation caused by tire slip angle and camber angle, or a combination of both [17].

2.3.2.1 Slip Angle

When a rolling tire is pushed sideways by a lateral force, it does not follow its exact heading direction, which creates a slip angle between where the wheel is pointing and where it actually moves [17]. This is illustrated in figure 2.5.

This behavior arises from the deformation of tread elements within the contact patch. As the tire rolls forward, these elements are initially undeformed but become progressively displaced laterally as they travel from the leading to the trailing edge of the contact area. This results in a gradual buildup of shear stresses, which generate lateral forces.

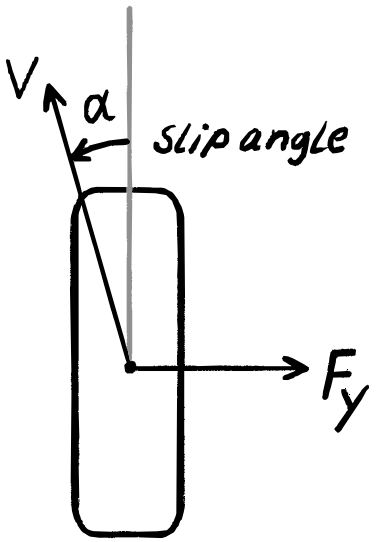

Figure 2.5: SSA α.

Due to the non-uniform distribution of these stresses, the resultant lateral force acts behind the geometric center of the contact patch as illustrated in figure 2.6. This offset, known as the pneumatic trail, produces an aligning moment that contributes to steering stability [17].

At small slip angles (typically up to 5 degrees), the lateral force increases approximately linearly with slip angle [17]. This region is characterized by the cornering stiffness, as illustrated in figure 2.7. As the slip angle increases further (around 15–20 degrees), the lateral force reaches a maximum and then decreases as portions of the contact patch begin to slide. The overall behavior is strongly influenced by tire construction, vertical load, inflation pressure, and tread geometry.

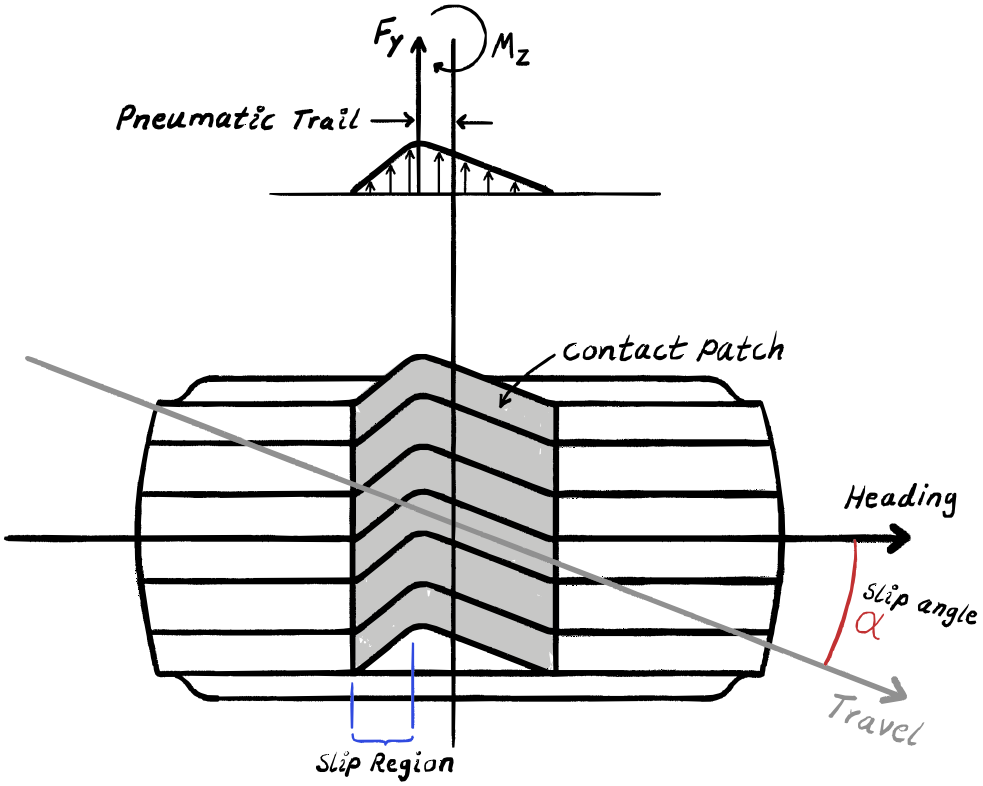

Figure 2.6: Tread deformation and resultant lateral force distribution within the tire contact patch during cornering.

The integrated shear stresses over the contact patch yield the net lateral force (F_y). In the linear region, this relationship is expressed through the cornering stiffness, defined as

$$C_\alpha = -\frac{\partial F_y}{\partial \alpha}\bigg|_{\alpha=0}. \tag{2.10}$$

Following the SAE convention, C_α is treated as a positive quantity in this work.

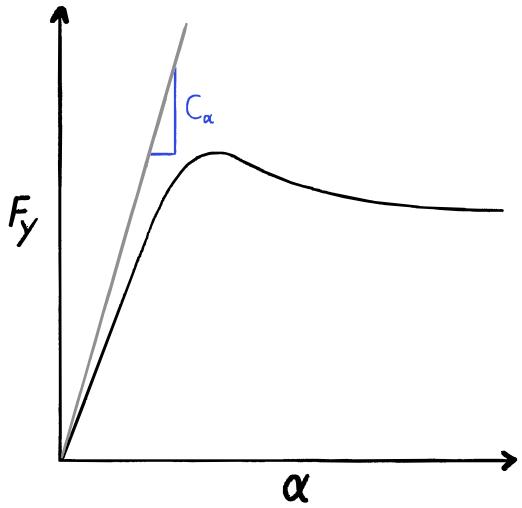

Figure 2.7: Relationship between side slip angle (SSA) and lateral force.

Cornering stiffness is influenced by several factors, including tire size, construction type (radial or bias-ply), number of plies, cord orientation, wheel width, and tread design [24]. For a specific tire, the most significant operating variables are vertical load and inflation pressure. This parameter plays a key role in determining vehicle handling characteristics, including the understeer gradient and overall stability of articulated vehicles.

2.3.2.2 Influence of Load, Inflation Pressure and Tire Geometry

Vertical load has a significant influence on tire cornering behavior [17]. Although the lateral force generated at a given slip angle increases with load, the relationship is not proportional. In fact, the cornering force per unit load is generally highest at lower loads, indicating a nonlinear dependence as illustrated in figure 2.8. As load increases, both the cornering stiffness and the effective friction coefficient tend to decrease, which results in a concave-down relationship between stiffness and load. This behavior is relevant for vehicle stability, particularly in relation to understeer characteristics.

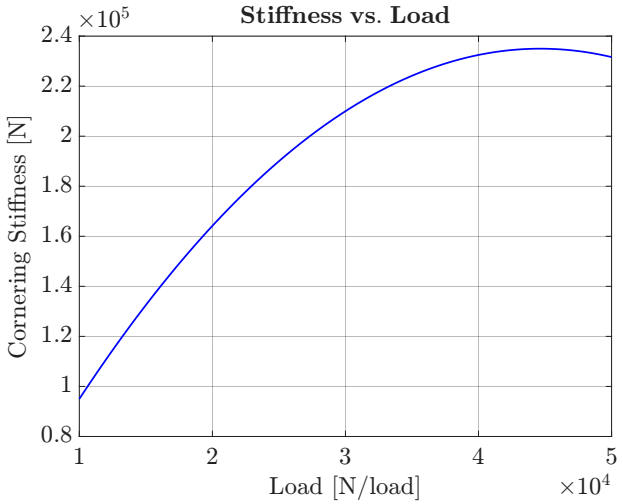

Figure 2.8: Relationship between Vertical load and Cornering Stiffness. The plot shows (2.9) of [25], using the parameters described in the same article.

Inflation pressure also affects cornering performance, primarily through its influence on carcass stiffness and contact patch geometry [17]. For passenger car tires, higher inflation pressure typically leads to increased cornering stiffness, as the stiffer carcass reduces

lateral deformation. However, the reduced contact area may also affect force generation. In practice, this relationship is not universally linear and depends on tire type and construction. Inflation pressure further influences the maximum lateral force, where lower pressures generally allow higher slip angles before saturation occurs, but at reduced peak performance.

Tire geometry, including size and width, also plays an important role [17]. Larger or wider tires generally exhibit higher cornering stiffness under the same load conditions. This is partly because they operate at a lower relative load compared to their rated capacity and partly due to increased structural stiffness in wider constructions. Similar effects can be achieved by increasing rim width, which enhances carcass support and improves lateral force response.

2.4 Introduction to Vehicle Dynamics

This section provides an introduction to vehicle dynamics, coordinate systems and the fundamental assumptions used in vehicle dynamics modeling. The goal is to establish a consistent framework for describing vehicle motion and forces prior to developing the dynamic models used in this work.

Vehicle dynamics describes the motion of ground vehicles under the influence of external forces and moments, and plays a fundamental role in vehicle safety, stability, and control system design. In particular, the ability to accurately predict vehicle behavior during maneuvers such as steering, braking, and acceleration is essential for the development of advanced driver assistance systems and autonomous vehicles [26], [27], [28].

The dynamic behavior of a vehicle is primarily governed by the interaction between the tires and the road surface, as well as external forces such as gravity and aerodynamic effects. Since the tires constitute the only contact between the vehicle and the ground, they are responsible for generating all forces that influence the motion of the vehicle. These forces determine the handling characteristics, stability, and overall performance of the vehicle [28].

Vehicle motion is typically described in terms of longitudinal, lateral, and yaw dynamics. Among these, lateral dynamics are of particular importance for vehicle stability, where key variables such as yaw rate and sideslip angle provide critical insight into vehicle behavior during cornering maneuvers [26]. These variables are widely used in vehicle stability control systems to assess and regulate the dynamic response of the vehicle under varying driving conditions.

To analyze and simulate vehicle behavior, various modeling approaches have been developed. These can generally be classified into two categories: physics-based models and data-driven models. Physics-based models rely on fundamental principles such as Newton's laws to describe the motion of the vehicle, but often require simplifying assumptions that may limit their accuracy under highly nonlinear conditions [27]. On the other hand, data-driven approaches, including neural network-based models,

have gained increasing attention due to their ability to capture complex nonlinear dynamics directly from data [27].

Among physics-based models, the single-track model, also known as the bicycle model, is one of the most widely used representations for vehicle lateral dynamics. This model simplifies the vehicle by combining the left and right wheels into a single front and rear wheel, assuming symmetric behavior. As a result, the model reduces complexity while retaining the dominant dynamics of the system, making it particularly suitable for control design and state estimation [26], [29].

Despite its simplicity, the single-track model provides a good trade-off between accuracy and computational efficiency, which makes it widely used in simulation and control applications. However, the model relies on several assumptions, such as equal tire forces on each axle and negligible roll and pitch dynamics, which may limit its applicability in extreme driving conditions [26], [29].

More complex models, such as multi-body or multi-track models, include additional degrees of freedom to capture vertical motion, roll, and pitch dynamics, as well as detailed tire-road interactions. While these models provide higher accuracy, they also increase computational complexity and require more parameters, making them less suitable for real-time estimation and control [29].

Therefore, a balance between model complexity and accuracy is required, particularly in applications involving real-time state and parameter estimation. In this context, simplified models such as the single-track model are commonly used together with estimation techniques to infer unmeasured states and uncertain parameters from sensor data.

In this thesis, the focus is on the estimation of tire-related parameters within a vehicle dynamics framework, where simplified models are combined with advanced estimation techniques to achieve "accurate" and robust performance under varying operating conditions.

2.4.1 Axis and Coordinate Systems

A consistent definition of axis and coordinate systems is fundamental for the analysis of vehicle dynamics [17]. Different conventions exist in the literature, most notably the SAE J670 and ISO 8855 standards, which primarily differ in the orientation of the vertical axis. In this work, a right-handed coordinate system is adopted, although ISO 8855, and the chosen orientation follows the requirements of the analysis.

A reference frame defines the geometric space in which motion is described. In vehicle dynamics, the Earth-fixed frame is commonly assumed to be inertial, meaning that it has no acceleration or rotation as mentioned in the section 2.1. This allows vehicle motion to be described relative to the ground.

Several coordinate systems are used to describe the motion of a vehicle and its components. The Earth-fixed coordinate system is used to represent the global

position and motion of the vehicle. In contrast, the vehicle-fixed coordinate system is attached to the vehicle body, with the longitudinal axis pointing forward, the lateral axis pointing to the side, and the vertical axis completing the right-handed system. This system is particularly useful for describing forces, moments, and vehicle states such as velocity and acceleration.

To relate vehicle motion to the road, the road plane is defined as the surface supporting the tire and generating the forces required for motion [17]. Since the road may not always be perfectly flat, a local road plane can be defined at each tire contact patch. Correspondingly, local tire coordinate systems are introduced, where the axes are aligned with the road surface and normal direction. These systems are essential for describing tire forces and slip behavior.

In addition, intermediate coordinate systems are often used to simplify the transformation of forces, moments, and motion variables between different frames. These transformations are necessary for modeling vehicle dynamics, where quantities are frequently expressed in both global and vehicle-fixed reference frames.

The selection of coordinate systems is not unique and may vary depending on the modeling approach [17]. However, a consistent definition is essential to ensure correct interpretation of kinematic relationships, force directions, and dynamic behavior.

2.4.2 Single-Track Model

To capture the transient lateral behavior of the vehicle, the single-track model, or bicycle model, can be employed [30], [31], [32]. This representation collapses the left and right wheels of each axle into a single point along the longitudinal centerline. The derivation is based on the force and moment balance at the vehicle's CoG.

As illustrated in Figure 2.9, the lateral velocity v_y, forward velocity v_x, and yaw rate ω_z define the motion. Applying Newton's second law for the lateral translation and rotation about the vertical axis yields:

$$ma_y = m(\dot{v}_y + v_x\omega_z) = F_{fy}\cos\delta + F_{ry} \approx F_{fy} + F_{ry} \tag{2.11}$$

$$J\dot{\omega}_z = F_{fy}l_f - F_{ry}l_r \tag{2.12}$$

where m is the vehicle mass, a_y is the lateral acceleration at the CoG, (O), $\dot{v}_y$ is the lateral acceleration relative to the vehicle frame, v_x is the longitudinal velocity, ω_z is the yaw rate, F_{fy} and F_{ry} are the lateral front and rear tire forces, δ is the steering angle, J is the yaw moment of inertia, l_f and l_r are the distances from the CoG to the front and rear axles, and $\dot{\omega}_z$ is the yaw acceleration. For small steering angles δ, the approximation $\cos\delta \approx 1$ is utilized.

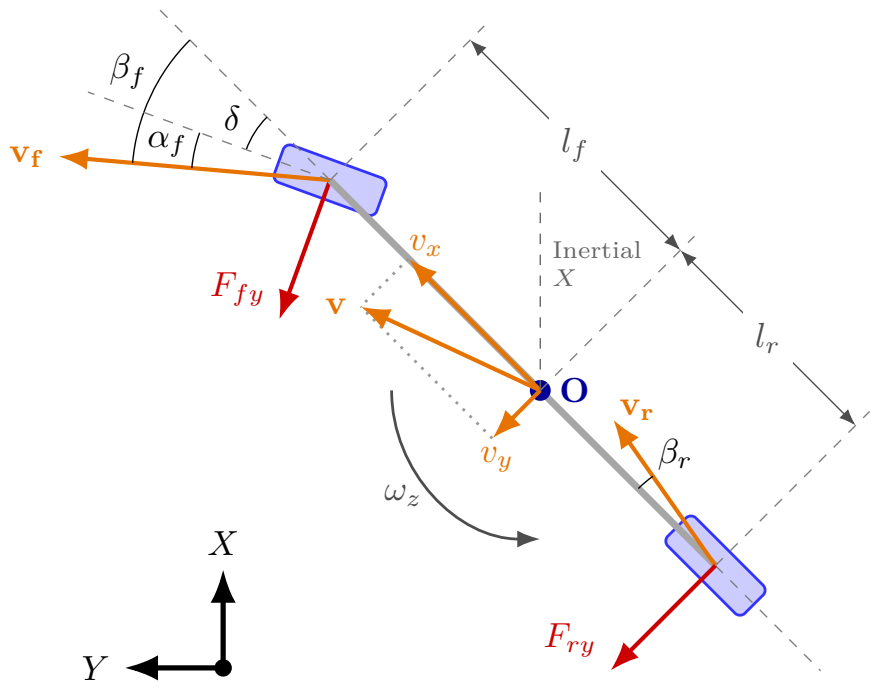

Figure 2.9: An illustration of the One-Track Model.

2.4.3 Tire Slip and Kinematics

The lateral forces F_{fy} and F_{ry} are generated by the tire slip angles α_f and α_r. Assuming a linear relationship within the tires' elastic region, the forces are modeled as:

$$F_{fy} = -C_f \alpha_f, \quad F_{ry} = -C_r \alpha_r \tag{2.13}$$

where C_f and C_r are the front and rear tire cornering stiffness, and α_f and α_r are the front and rear side slip angles.

The slip angles are defined as the difference between the wheel's orientation and the direction of its velocity vector. By analyzing the kinematics at each axle, the slip angles can be expressed in terms of the state variables:

$$\alpha_f = \beta_f - \delta \approx \frac{v_y + l_f \omega_z}{v_x} - \delta \tag{2.14}$$

$$\alpha_r = \beta_r \approx \frac{v_y - l_r \omega_z}{v_x} \tag{2.15}$$

where β_f and β_r are the body slip angles at the front and rear axles.

2.4.4 The State-Space Form

By substituting the kinematic slip relations into the force equations and rearranging for the derivatives $\dot{v}_y$ and $\dot{\omega}_z$, the system is formulated into a standard state-space representation:

$$\begin{bmatrix} \dot{v}_y \\ \dot{\omega}_z \end{bmatrix} = \begin{bmatrix} -\dfrac{C_f + C_r}{m v_x} & \dfrac{C_r l_r - C_f l_f}{m v_x} - v_x \\ \dfrac{C_r l_r - C_f l_f}{J v_x} & -\dfrac{C_f l_f^2 + C_r l_r^2}{J v_x} \end{bmatrix} \begin{bmatrix} v_y \\ \omega_z \end{bmatrix} + \begin{bmatrix} \dfrac{C_f}{m} \\ \dfrac{C_f l_f}{J} \end{bmatrix} \delta \tag{2.16}$$

In short form, the system is represented as:

$$\dot{x} = \mathbf{A}x + \mathbf{B}\delta \tag{2.17}$$

where $x = [v_y,\ \omega_z]^T$ is the state vector and δ is the steering input.

2.4.5 Limitations of the Linear Single-Track Model

While the linear single-track model is a powerful tool for initial lateral dynamics analysis, its validity is constrained by several fundamental simplifications. The primary limitations include:

- **Constant Longitudinal Speed:** The model assumes v_x is constant. In real-world driving, longitudinal and lateral dynamics are coupled; for instance, braking in a curve alters the force distribution and trajectory.
- **Linear Tire Assumption:** The model assumes tire forces are directly proportional to slip angles ($F_y = -C\alpha$) with proportinaly constant of known tire cornering stiffness.
- **Zero CoG Height:** By assuming the Center of Gravity (CoG) is at ground level, the model neglects the effects of lateral load transfer. In reality, a non-zero CoG height causes the outside tires to take more load than the inside tires during cornering.
- **Neglected Roll and Pitch Motion:** The model assumes a completely rigid body in the vertical and roll planes. For heavy-duty vehicles with high CoG, roll dynamics significantly influence the lateral stability and the actual slip angles at the axles.

This model provides the theoretical foundation for the estimation framework developed in this thesis.

2.5 Estimation and Bayesian Filtering

The mathematical description of dynamical systems is traditionally formulated within a deterministic framework [33]. In many engineering applications, including vehicle dynamics, the system state is not directly observable and must instead be inferred from noisy and incomplete measurements [34]. This leads to the class of problems known as state estimation or filtering.

In this context, the system state refers to a set of variables that fully describe the system behavior, such as position, velocity, yaw rate, or other dynamic quantities. These states evolve over time according to a dynamic model, while measurements provide indirect and noisy observations of the system [35].

A key challenge in practical systems is that neither the system dynamics nor the measurement process can be modeled perfectly. Uncertainties arise from unmodeled dynamics, parameter variations, and sensor noise. To account for this, stochastic modeling is introduced, where both the system evolution and the measurements are treated as probabilistic rather than deterministic quantities. This approach is commonly referred to as Bayesian filtering [36].

2.5.1 State-Space Representation with Uncertainty

A general nonlinear discrete-time system can be described as:

$$x_k = f(x_{k-1}, u_{k-1}) + w_{k-1} \tag{2.18}$$

$$z_k = h(x_k) + v_k \tag{2.19}$$

where $x_k \in \mathbb{R}^n$ is the state vector, $z_k \in \mathbb{R}^m$ is the measurement vector, $f(\cdot)$ is the nonlinear state transition function describing how the state evolves from time $k-1$ to k, $h(\cdot)$ is the nonlinear measurement function mapping the state to the measurement space, w_{k-1} is the process noise, and v_k is the measurement noise.

The stochastic nature of the system is introduced through:

- **Process Noise (w_{k-1}):** Represents uncertainties in the system model, such as unmodeled dynamics, disturbances, or parameter variations. It is commonly modeled as zero-mean Gaussian noise with covariance Q, $\mathcal{N}(0, Q)$.
- **Measurement Noise (v_k):** Represents sensor inaccuracies and environmental disturbances, modeled as zero-mean Gaussian noise with covariance R, $\mathcal{N}(0, R)$.

In a Bayesian framework, the objective is to compute the posterior distribution of the state conditioned on all available measurements:

$$p(x_k \mid z_{1:k}) \tag{2.20}$$

Using the Markov assumption for the state evolution and conditional independence of the measurements, the filtering problem can be decomposed recursively into two steps.

2.5.1.1 Prediction step

The prior (predicted) state distribution is obtained by propagating the previous posterior through the process model:

$$p(x_k \mid z_{1:k-1}) = \int p(x_k \mid x_{k-1})\, p(x_{k-1} \mid z_{1:k-1})\, dx_{k-1} \tag{2.21}$$

Here, $p(x_{k-1} \mid z_{1:k-1})$ is the posterior from the previous time step (knowledge of the state given past measurements), and $p(x_k \mid x_{k-1})$ is the transition probability (how the state evolves according to the dynamics). The integral marginalizes over all possible previous states.

This step represents the time evolution of the system and introduces uncertainty through the process noise.

2.5.1.2 Update step

When a new measurement z_t becomes available, the posterior distribution is computed using Bayes' theorem:

$$p(x_k \mid z_{1:k}) = \frac{p(z_k \mid x_k)\, p(x_k \mid z_{1:k-1})}{p(z_k \mid z_{1:k-1})} \tag{2.22}$$

Here, $p(x_k \mid z_{1:k-1})$ is the prior from the prediction step, $p(z_k \mid x_k)$ is the likelihood (probability of the measurement given the state), and the denominator normalizes the distribution:

$$p(z_k \mid z_{1:k-1}) = \int p(z_k \mid x_k)\, p(x_k \mid z_{1:k-1})\, dx_k \tag{2.23}$$

2.5.1.3 Recursive structure

Together, these two steps define a recursive Bayesian filtering algorithm:

$$\text{Prediction:} \quad p(x_k \mid z_{1:k-1}) \tag{2.24}$$

$$\text{Update:} \quad p(x_k \mid z_{1:k}) \tag{2.25}$$

This formulation is exact for linear Gaussian systems and forms the theoretical basis for the Kalman filter. Kalman filters are widely used in data fusion applications such as navigation, tracking, and simultaneous localization and mapping (SLAM) [37]. However, tuning the filter parameters, including process noise covariance, requires significant time and effort.

2.5.2 Gaussian Assumption

In practical applications, it is common to assume that the state distribution is Gaussian [36]. This assumption allows the distribution to be fully described by:

- The mean vector $\mu = \mathbb{E}[x]$
- The covariance $P = \mathbb{E}[(x - \mu)(x - \mu)^T]$

The challenge arises when nonlinear system dynamics are present, since a Gaussian distribution propagated through a nonlinear function is no longer exactly Gaussian. For nonlinear systems, such as vehicle dynamics with tire forces and slip angles,

approximate solutions are needed. These can be achieved with nonlinear filters such as the Unscented Kalman Filter (UKF).

2.5.3 The Unscented Kalman Filter (UKF)

For nonlinear systems, the exact computation of the Bayesian filtering equations becomes analytically intractable due to the nonlinear transformation of probability distributions. In particular, even if the prior distribution $p(x_{k-1} \mid z_{1:k-1})$ is Gaussian, the transformed distribution under nonlinear dynamics $f(\cdot)$ is generally non-Gaussian.

The Unscented Kalman Filter (UKF) addresses this problem by approximating the propagation of mean and covariance through nonlinear functions without linearization [36]. Instead of approximating the nonlinear functions, the UKF approximates the probability distribution itself.

2.5.3.1 Unscented Transform

Let the prior state be Gaussian distributed:

$$x_{k-1} \sim \mathcal{N}(\mu_{k-1}, P_{k-1}) \tag{2.26}$$

The Unscented Transform represents this distribution using a set of deterministic samples, called sigma points:

$$\chi_{k-1}^{(i)}, \quad i = 0, \ldots, 2n \tag{2.27}$$

where n is the state dimension. These points are constructed such that they exactly match the first two moments of the Gaussian distribution:

$$\chi_{k-1}^{(0)} = \mu_{k-1} \tag{2.28}$$

$$\chi_{k-1}^{(i)} = \mu_{k-1} + \gamma\sqrt{P_{k-1}}_i, \quad i = 1, \ldots, n \tag{2.29}$$

$$\chi_{k-1}^{(i+n)} = \mu_{k-1} - \gamma\sqrt{P_{k-1}}_i, \quad i = 1, \ldots, n \tag{2.30}$$

where $\gamma = \sqrt{n/(1 - W_0)}$. The weights W are defined as:

$$W_0 = 1 - \frac{n}{3} \tag{2.31}$$

$$W_i = \frac{1 - W_0}{2n}, \quad i = 1, \ldots, 2n \tag{2.32}$$

The weight for the mean and covariance is the same for all sigma points except the first, which uses W_0 for both mean and covariance reconstruction.

2.5.3.2 Prediction Step

Each sigma point is propagated through the nonlinear process model:

$$\chi_k^{(i)} = f(\chi_{k-1}^{(i)}, u_{k-1}) \tag{2.33}$$

The predicted mean is then computed as a weighted average:

$$\hat{\mu}_k^- = W_0 \chi_k^{(0)} + \sum_{i=1}^{2n} W_i \chi_k^{(i)} \tag{2.34}$$

The predicted covariance is computed from the spread of the transformed sigma points:

$$\hat{P}_k^- = W_0(\chi_k^{(0)} - \hat{\mu}_k)(\chi_k^{(0)} - \hat{\mu}_k)^T + \sum_{i=1}^{2n} W_i(\chi_k^{(i)} - \hat{\mu}_k)(\chi_k^{(i)} - \hat{\mu}_k)^T + Q \tag{2.35}$$

2.5.3.3 Measurement Prediction

The sigma points are then mapped into measurement space:

$$\mathcal{Z}_k^{(i)} = h(\chi_k^{(i)}) \tag{2.36}$$

The predicted measurement mean is:

$$\hat{z}_k = W_0 \mathcal{Z}_k^{(0)} + \sum_{i=1}^{2n} W_i \mathcal{Z}_k^{(i)} \tag{2.37}$$

The innovation covariance is:

$$S_k = W_0(\mathcal{Z}_k^{(0)} - \hat{z}_k)(\mathcal{Z}_k^{(0)} - \hat{z}_k)^T + \sum_{i=1}^{2n} W_i(\mathcal{Z}_k^{(i)} - \hat{z}_k)(\mathcal{Z}_k^{(i)} - \hat{z}_k)^T + R \tag{2.38}$$

The cross-covariance between state and measurement is:

$$C_k = W_0(\chi_k^{(0)} - \hat{\mu}_k)(\mathcal{Z}_k^{(0)} - \hat{z}_k)^T + \sum_{i=1}^{2n} W_i(\chi_k^{(i)} - \hat{\mu}_k)(\mathcal{Z}_k^{(i)} - \hat{z}_k)^T \tag{2.39}$$

2.5.3.4 Update Step

The Kalman gain is defined as:

$$K_k = C_k S_k^{-1} \tag{2.40}$$

The posterior state estimate is then updated using the measurement z_k:

$$\hat{\mu}_k = \hat{\mu}_k^- + K_k(z_k - \hat{z}_k) \tag{2.41}$$

$$\hat{P}_k = \hat{P}_k^- - K_k S_k K_k^T \tag{2.42}$$

2.5.3.5 Interpretation

The UKF can be interpreted as an efficient numerical approximation of the Bayesian filtering equations. Instead of linearizing the system dynamics as in the Extended Kalman Filter, the UKF propagates a set of deterministically chosen samples through the nonlinear functions. This allows for a more accurate approximation of the posterior mean and covariance, especially in systems with strong nonlinearities such as tire dynamics and vehicle lateral motion.

2.5.3.6 Application to Vehicle Dynamics

In vehicle dynamics, many important states such as tire forces, slip angles, and cornering stiffness cannot be directly measured. The UKF enables estimation of these quantities by combining a physics-based model (e.g., the linear single-track model) with sensor measurements.

By augmenting the state vector with parameters such as TCS, the filter can adapt to changing operating conditions, including variations in tire characteristics, road friction, and load transfer.

2.5.4 Filter Consistency

In static estimation, consistency means that the estimate converges to the true value as more data becomes available [38]. For dynamic state estimation, however, the state does not converge. Instead, the filter provides an estimate along with an associated covariance matrix. Divergence may occur due to modeling errors, numerical issues, or programming mistakes.

2.5.4.1 Normalized Estimation Error Squared (NEES)

Under the linear-Gaussian assumption, the estimation error $\tilde{x} = x - \hat{x}$ is normally distributed with zero mean and covariance P, i.e., $\tilde{x} \sim \mathcal{N}(0, P)$. To evaluate whether the filter's reported covariance P correctly reflects the actual estimation error, the error must be normalized.

This is achieved by multiplying $\tilde{x}$ with the inverse square root of P, denoted $P^{-1/2}$. The transformation, known as whitening, yields another normally distributed random vector

$$u = P^{-1/2}\tilde{x}, \tag{2.43}$$

with covariance

$$\mathbb{E}[uu^T] = P^{-1/2}\mathbb{E}[(x - \tilde{x})(x - \tilde{x})^T]P^{-1/2} = P^{-1/2}PP^{-1/2} = I, \tag{2.44}$$

where I is the identity matrix. From this it follows that

$$u \sim \mathcal{N}(0, I). \tag{2.45}$$

Since the covariance matrix of u is diagonal, its components are uncorrelated. Uncorrelatedness implies independence, so each component u_i is an independent standard normal random variable:

$$u_i \sim \mathcal{N}(0,1), \quad i = 1, \ldots, n \tag{2.46}$$

where n is the dimension of the state vector. The squared norm of u is then the sum of squares of these n independent standard normal variables:

$$\|u\|^2 = u^T u = \sum_{i=1}^{n} u_i^2 \tag{2.47}$$

The squared norm of u, written in terms of the original estimation error is the definition of Normalized Estimation Error Squared (NEES):

$$q = u^T u = \tilde{x}^T P^{-1} \tilde{x}. \tag{2.48}$$

Since q is the sum of squares of n independent standard normal random variables, it follows by definition that q is chi-squared-distributed with n degrees of freedom:

$$q \sim \chi^2(n). \tag{2.49}$$

The expected value of a chi-squared random variable equals its degrees of freedom. Therefore, if the filter is consistent, we must have that

$$\mathbb{E}[q] = n. \tag{2.50}$$

2.6 Local Observability Gramian

Consider an observed dynamical system:

$$\begin{aligned} \dot{x}(t) &= f(x(t)) \\ z(t) &= h(x(t)) \\ x(0) &= x_0. \end{aligned} \tag{2.51}$$

Suppose that the system is observable over the interval $t \in [0, T]$, for some $T > 0$. Define the solution of (2.51) to be the nominal state trajectory $x^0(t)$ and its corresponding output trajectory $z^0(t)$ over the observable time domain, given by the initial state x_0.

In terms of observability, we are interested in whether or not a small change in state x is measurable in the output z. To that end, suppose we instead have the initial

condition

$$x(0) = x_0 + \delta x_0,$$

for some non-zero δx_0. Then, we define the corresponding perturbed state and output trajectories as $x(t)$ and $z(t)$, respectively. The localized trajectory deviations are:

$$\delta x(t) \approx x(t) - x^0(t),$$
$$\delta z(t) \approx z(t) - z^0(t).$$

Applying a first-order Taylor series expansion around the moving nominal trajectory $x^0(t)$ isolates the error dynamics into the tangent linear approximating system:

$$\begin{aligned} \dot{\delta x}(t) &= A(t)\,\delta x(t), \\ \delta z(t) &= C(t)\,\delta x(t), \\ \delta x(0) &= \delta x_0. \end{aligned} \tag{2.52}$$

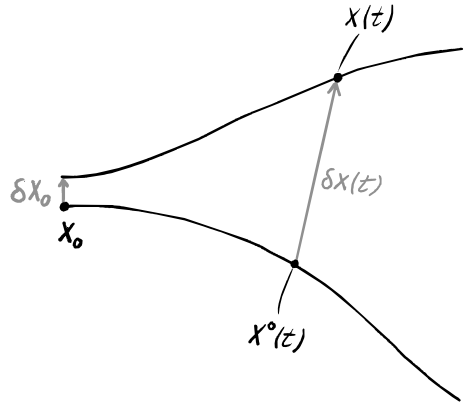

Figure 2.10: A visual representation of the two state space trajectories separated by $\delta x(t)$.

The system matrices $A(t)$ and $C(t)$ are the time-varying Jacobians evaluated continuously along the reference path:

$$A(t) = \frac{\partial f}{\partial x}(x^0(t)),$$
$$C(t) = \frac{\partial h}{\partial x}(x^0(t)).$$

Figure 2.10 is an illustration of (2.52), showing how a small deviation δx_0 from the nominal trajectory can grow over time.

Letting $\Phi(t;0)$ be the fundamental matrix solution of (2.52),

$$\begin{aligned} \dot{\Phi}(t;0) &= A(t)\,\Phi(t;0), \\ \Phi(0;0) &= I, \end{aligned} \tag{2.53}$$

$$\Longrightarrow$$

$$\begin{aligned} \delta x(t) &= \Phi(t;0)\,\delta x_0, \\ \delta z(t) &= C(t)\,\Phi(t;0)\,\delta x_0, \end{aligned} \tag{2.54}$$

where $\delta z(t)$ maps the initial state uncertainty δx_0 to the observable output deviation over $[0, T]$. Squaring the deviation and integrating over time, we have

$$\begin{aligned} \textit{signal energy} &= \int_0^T \delta z^\mathsf{T}(t)\,\delta z(t)\,dt \\ &= \delta x_0^\mathsf{T} \left(\int_0^T \Phi^\mathsf{T}(t;0)\,C^\mathsf{T}(t)\,C(t)\,\Phi(t;0)\,dt \right) \delta x_0 \\ &= \delta x_0^\mathsf{T}\,W_o(0,T)\,\delta x_0, \end{aligned} \tag{2.55}$$

where

$$W_o(0,T) = \int_0^T \Phi^\mathsf{T}(t;0)\,C^\mathsf{T}(t)\,C(t)\,\Phi(t;0)\,dt \tag{2.56}$$

is the local observability Gramian [39].

2.6.1 Quantifying Observability

If the state deviation δx_0 aligns with an eigenvector of W_o corresponding to a large eigenvalue, the resulting signal energy will be measurable. On the contrary, if δx_0 aligns with an eigenvector corresponding to a zero or near-zero eigenvalue, the resulting output signal will generate negligible energy, i.e., it is unobservable.

A common method used to determine observability is the observability rank condition. It is simply a statement of the system being observable, or not. If we instead want to measure to which degree the system is observable, it is stated in [39] that the singular values of W_o can be used to quantify the unobservability of a non-linear system.

Let the singular values of W_o be σ_i, where

$$\sigma_1 \geq \sigma_2 \geq \cdots \geq \sigma_n.$$

Then [39] defines the following two measures of observability:

$$\text{local unobservability index} = \sigma_n^{-1}, \tag{2.57}$$

$$\text{local estimation condition number} = \frac{\sigma_1}{\sigma_n}. \tag{2.58}$$

For the purpose of this project,

$$\textit{local observability metric} = \frac{\sigma_{n-1}}{\sigma_n}, \tag{2.59}$$

was used to evaluate and implement update strategies. Using the lowest two singular values was chosen based on the assumption that the smaller relative difference on the lower end would provide more stable results compared to (2.58).

2.6.2 Discrete Time Formulation

Let $t_k = k\,\Delta t < T$, $k \in \mathbf{Z}^{0+}$, for some suitable sampling interval Δt. We define

$$A_k = A(t_k), \tag{2.60}$$

$$C_k = C(t_k), \tag{2.61}$$

to represent the time-varying Jacobians sampled at a discrete time step k. Assume that A_k is **piecewise constant** over the small interval $[t_k, t_{k+1})$. The matrix solution to the problem

$$\begin{aligned} \dot{\Phi}(t_{k+1}; t_k) &= A_k \Phi(t_{k+1}; t_k) \\ \Phi(t_k; t_k) &= I \end{aligned}$$

is then by assumption the matrix exponential

$$\Phi(t_{k+1}; t_k) = e^{A_k(t_{k+1} - t_k)} = e^{A_k \Delta t}. \tag{2.62}$$

Using equation (2.62), letting $\Phi_k = \Phi(t_{k+1}; t_k)$, we define the discrete-time system corresponding to (2.52):

$$\begin{aligned} \delta x_{k+1} &= \Phi_k \, \delta x_k, \\ \delta z_k &= C_k \, \delta x_k. \end{aligned} \tag{2.63}$$

Recursively applying the state update from the initial perturbation δx_0 to the deviation δx_k at time step k yields the state transition matrix

$$\Psi_k = \prod_{i=1}^{k} \Phi_{k-i} = \Phi_{k-1} \Phi_{k-2} \cdots \Phi_0, \tag{2.64}$$

where $\Psi_0 = I$, as in (2.52). The discrete output deviation at time step k is projected via $\delta z_k = C_k \Psi_k \delta x_0$. If we let $N = \lfloor T/\Delta t \rfloor$, the discrete-time version of (2.55) becomes

$$\begin{aligned} \textit{signal energy} &\approx \sum_{k=0}^{N-1} \delta z_k^{\mathsf{T}} \, \delta z_k \\ &= \delta x_0^{\mathsf{T}} \left(\sum_{k=0}^{N-1} \Psi_k^{\mathsf{T}} \, C_k^{\mathsf{T}} \, C_k \, \Psi_k \right) \delta x_0 \\ &= \delta x_0^{\mathsf{T}} \, W_o^d(0, N) \, \delta x_0, \end{aligned} \tag{2.65}$$

where the discrete-time local observability Gramian is

$$W_o^d(0, N) = \sum_{k=0}^{N-1} \Psi_k^{\mathsf{T}} \, C_k^{\mathsf{T}} \, C_k \, \Psi_k. \tag{2.66}$$

In this report, there is no need to differentiate between discrete- and continuous time, so the discrete time-varying linear transition matrix at time step k will be denoted by A_k, not by Φ_k, differing from the discussion in this subsection.

2.6.3 Relation to the Observability Matrix

Equation (3.8) in [40] is the common definition of the observability matrix for a linear, time-invariant system:

$$\mathcal{O} = \begin{bmatrix} C \\ C\,A \\ C\,A^2 \\ C\,A^3 \\ \vdots \\ C\,A^{n-1} \end{bmatrix} \tag{2.67}$$

Let A be an $n \times n$ state transition matrix for a discrete, linear, time-invariant system, with a corresponding output projection matrix C. For such a system, the discrete local observability Gramian in (2.66) turns into

$$W_o^d(N) = \sum_{k=0}^{N-1} \left(A^{\mathsf{T}}\right)^k C^{\mathsf{T}} \, C \, (A)^k. \tag{2.68}$$

Rewriting the sum in (2.68) as a matrix multiplication, we get

$$W_o^d(n) = \mathcal{O}^{\mathsf{T}} \mathcal{O}. \tag{2.69}$$

3

Method

This chapter outlines the methodology used to answer the research questions outlined in section 1.3. Two estimation frameworks have been developed and evaluated. The first framework was based on experimental data recorded during the early spring of 2022, and a specialized MATLAB framework developed by this project's supervisor as part of a PhD project. The second estimation framework was implemented using the simulation software suit *IPG TruckMaker*, in combination with Simulink to interface with the simulation and to implement the estimator. The details of each implementation follow in the subsections below.

3.1 Estimation using Experimental Data

The experimental data was provided by the project's supervisor, Axel Ceder. According to Axel, all data was collected by the motion estimation and vehicle automation (MEVA) department at Volvo GTT, and it was recorded using inertial navigation system (INS) units developed by the UK-based company OXTS [41], mounted to each body in the articulated vehicle configuration during experiments. The log data will be part of [42], to-be published by Axel Ceder as part of his PhD thesis. The logs includes meta-data for vehicle geometry.

For this method, the data log used was `IceCircle_2022_03_07_165704.h5` recorded Monday 7$^{\text{th}}$ March, 2022. The vehicle drove a steady-state circle with a diameter of 30 m. The vehicle trajectory is shown in figure 3.2 as a planar projection of the true 3-dimensional path. The estimator in this section was implemented with the help of a MATLAB framework for multiple unit state estimation (MUSE).

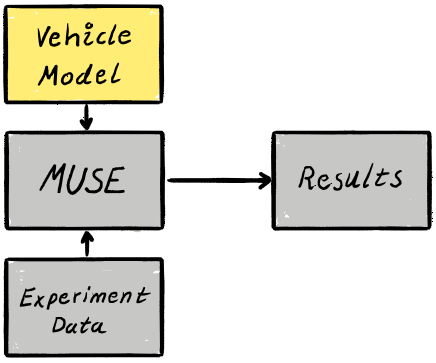

Figure 3.1: Schematic of a MUSE project.

3.1.1 MUSE

Multiple unit state estimation (MUSE) is a MATLAB-based framework for state estimation of multiple-unit vehicles like truck-trailer combinations [42]. It was developed

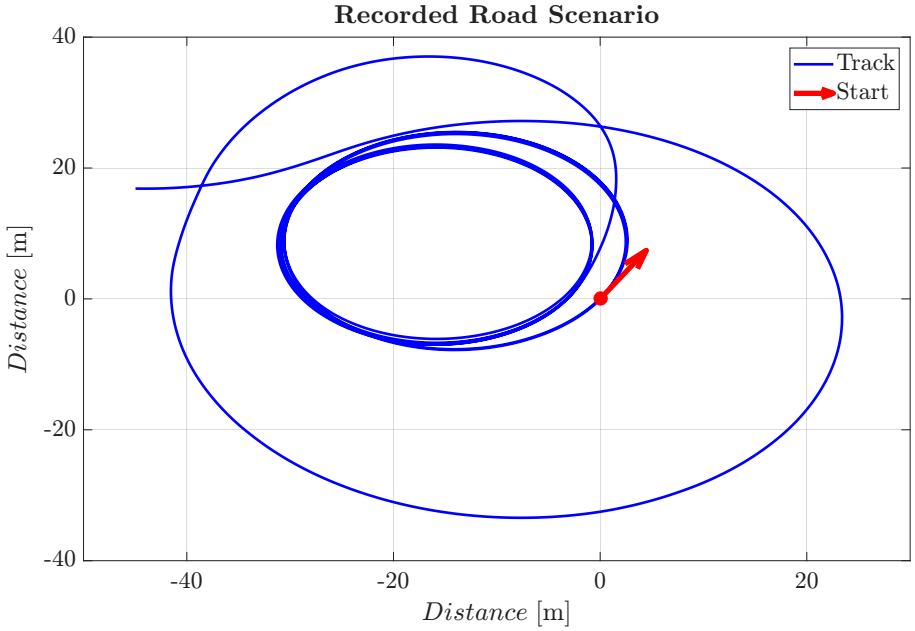

Figure 3.2: A planar projection of the trajectory (blue) that the articulated vehicle drove in the experimental data used for the MUSE estimator. The vehicle driving scenario was a steady-state circle of ⌀30 m. The red vector indicates the start position of the vehicle.

as part of PhD research at Chalmers University of Technology focusing on state estimation for articulated heavy vehicles. The workflow of using this framework is shown in figure 3.1. Since MUSE has not been published at the time of writing this report, a brief description of how MUSE works will follow.

The framework converts a vehicle model, which is specified by defining an estimator class, into a state space model and a measurement model. Using the two models, it then implements an unscented Kalman filter to perform sensor fusion for state estimation on a chosen time-series log of experimental data. Implementing the vehicle model for TCS parameter estimation was a matter of defining a subclass of the MUSE estimation model, providing definitions of the following methods of that class:

- `defineMeasurements:` Defines measurements, e.g. acceleration or velocity, that the model uses.
- `defineInputs:` Defines the inputs the model uses. For example, applied torque or steering angle.
- `modelConfiguration:` Defines structural constants such as which axles are used, which of them are steerable, track width, et cetera.
- `defineParameters:` Defines modeling parameters symbolically, for example gravitational acceleration or the inertial tensor.
- `setupParameters:` Assign parameter values and corresponding uncertainty. Specifies state covariance P_0, process noise matrix Q and the measurement noise matrix R.
- `defineEquations:` The mathematical description of the model, defined using symbolic variables and parameters.

For this estimator implementation, MUSE did most of the heavy lifting. It created a Kalman filter from the vehicle model, processed the experiment log to create unified time series of the different measurements in each log file, and then ran the filter while feeding it the experiment data. The MATLAB code for the MUSE vehicle model class can be found in [43]. The mathematics of the implementation will now follow.

3.1.2 Modified One-Track Model

The physical and state-space model used for the MUSE-based estimator was derived from the One-Track Model described in section 2.4.2 and section 2.4.4, respectively. The state vector was augmented to also include v_x, C_f and C_r. This change yielded a non-linear state space model. One of the nonlinearities can be seen if equation (2.11) is solved for $\dot{v}_y$:

$$\dot{v}_y = \frac{1}{m}(F_{fy}\cos\delta + F_{ry}) - v_x\omega_z. \tag{3.1}$$

The geometry of the physical quantities of the model are shown in figure 3.3. They will be relevant to the modeling of vehicle dynamics described in the subsequent subsections. The figure is the same asfigure 2.9, but also includes longitudinal forces F_{fx} and F_{rx}. The indicated vertical (Z) dimension is not considered in the MUSE-based estimator's vehicle model, but will be relevant in section 3.2.

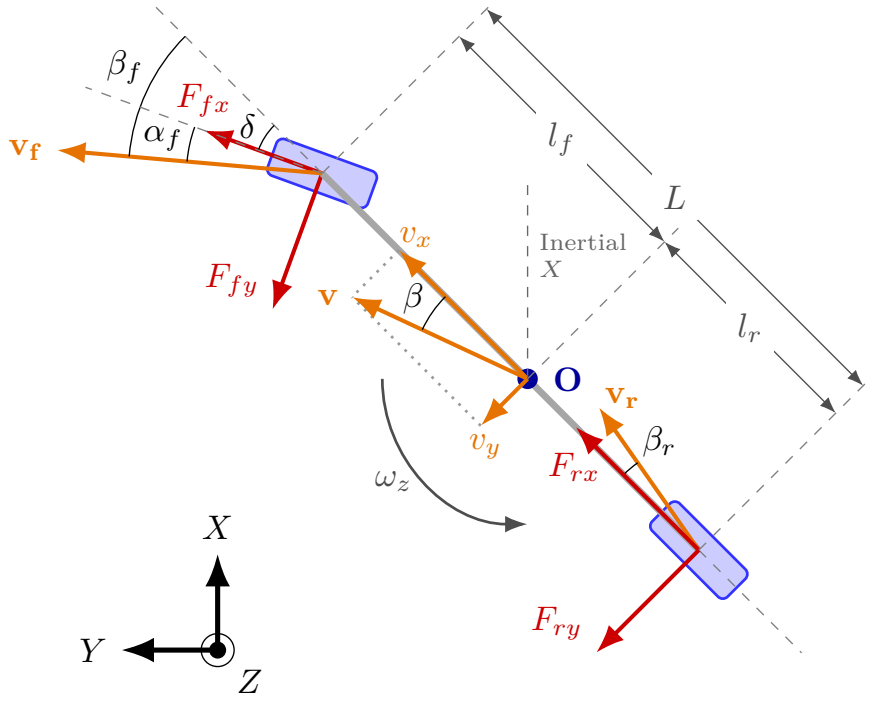

Figure 3.3: The single-track (bicycle) model used for state prediction. The vehicle body is represented by a rigid chassis with two combined wheels. Key quantities include the center of gravity (CoG), steering angle δ, slip angles α_f and α_r, and the yaw rate ω_z.

3.1.2.1 Modeling Assumptions

To constrain the dynamic problem, the following was assumed to define the system's operational validity domain:

- Motion is strictly planar. Rolling resistance, roll, pitch, heave and aerodynamics are neglected.
- The vehicle being modeled is a single rigid-body truck.
- Left-right structural and mass symmetry permits the aggregation of wheel pairs into a single centerline track.
- Inertial properties (mass m and yaw inertia J_z) are time invariant.
- Tire lateral forces are modeled using a slip-angle formulation with linear cornering stiffness, valid for small slip angles.
- Cornering stiffness parameters C_f and C_r are augmented as slowly varying invariant states ($\dot{C}_f = 0$, $\dot{C}_r = 0$).

3.1.2.2 State and Parameter Definitions

The 5-dimensional continuous-time state vector of the model is detailed in table 3.1. To facilitate online estimation of the unknown tire parameters, they were added to the state vector along with observable kinematic states. The process noise matrix Q is shown in table 3.2.

Table 3.1: MUSE model state vector definition along with initial values. The first three states were initialized to the first sample of the corresponding time series from a given log file.

Symbol	Description	Unit	Initial Value
v_x	Longitudinal velocity at CoG	$\mathrm{m\,s^{-1}}$	–
v_y	Lateral velocity at CoG	$\mathrm{m\,s^{-1}}$	–
ω_z	Yaw rate	$\mathrm{rad\,s^{-1}}$	–
C_f	Front tire cornering stiffness	$\mathrm{N\,rad^{-1}}$	400000
C_r	Rear tire cornering stiffness	$\mathrm{N\,rad^{-1}}$	400000

Table 3.3 summarizes the vehicle parameters used in the model. Each physical value was obtained from either experiment log meta-data, parsed and provided to the model through interfaces available in MUSE, or from estimates made by MUSE in real-time. In the latter case, they have been treated as constant in accordance with the simplifying assumption stated in section 3.1.2.1.

Table 3.2: MUSE model process noise matrix Q and its values.

Element	State	Variance	Unit
Q_{11}	v_x	2×10^{-2}	$\mathrm{m}^2/\mathrm{s}^2$
Q_{22}	v_y	2×10^{-2}	$\mathrm{m}^2/\mathrm{s}^2$
Q_{33}	ω_z	3×10^{-4}	$\mathrm{rad}^2/\mathrm{s}^2$
Q_{44}	C_f	0	$1/\mathrm{rad}^2$
Q_{55}	C_r	0	$1/\mathrm{rad}^2$

Table 3.3: MUSE model vehicle parameters

Symbol	Description	Symbol	Description
m	Vehicle mass	l_f	Distance: CoG to front axle
J_z	Yaw moment of inertia	l_r	Distance: CoG to rear axle
L	Wheelbase ($l_f + l_r$)	R_w	Effective wheel radius
b	Half track width		

3.1.2.3 Control Inputs

The control signals available in MUSE and used by the model are listed in table 3.4.

Table 3.4: Control input signals used by the MUSE model

Symbol	Description	Unit
δ	Steering-to-road angle	rad
T_r	Rear axle torque	N m

3.1.2.4 Measurement Signals

Table 3.5 lists the measurements used by the vehicle model for the MUSE estimator. The corresponding measurement noise matrix R and its values are listed in table 3.6.

Table 3.5: Measurements used by the MUSE model

Symbol	Description	Unit
a_x	Longitudinal acceleration	$\mathrm{m\,s}^{-2}$
a_y	Lateral acceleration	$\mathrm{m\,s}^{-2}$
v_x	Longitudinal velocity	$\mathrm{m\,s}^{-1}$
v_y	Lateral velocity	$\mathrm{m\,s}^{-1}$
ω_z	Yaw rate	$\mathrm{rad\,s}^{-1}$
ω_{RL}	Rear left wheel speed	$\mathrm{rad\,s}^{-1}$
ω_{RR}	Rear right wheel speed	$\mathrm{rad\,s}^{-1}$

Table 3.6: MUSE model measurement noise matrix R and its values.

Element	Measurement	Variance	Unit
R_{11}	a_x	$1/3 \times 2$	$\mathrm{m}^2/\mathrm{s}^4$
R_{22}	a_y	$1/3 \times 2$	$\mathrm{m}^2/\mathrm{s}^4$
R_{33}	v_x	$1/3 \times 2 \times 10^{-1}$	$\mathrm{m}^2/\mathrm{s}^2$
R_{44}	v_y	$1/3 \times 2 \times 10^{-1}$	$\mathrm{m}^2/\mathrm{s}^2$
R_{55}	ω_z	$1/3 \times 5 \times 10^{-2}$	$\mathrm{rad}^2/\mathrm{s}^2$
R_{66}	ω_{RL}	$1/3 \times 5 \times 10^{-2}$	$\mathrm{rad}^2/\mathrm{s}^2$
R_{77}	ω_{RR}	$1/3 \times 5 \times 10^{-2}$	$\mathrm{rad}^2/\mathrm{s}^2$

3.1.2.5 Vehicle Kinematics and Slip Angles

Figure 3.3 illustrates the kinematic geometry. Tire slip angles (α_f, α_r) represent the angular deviation between the physical wheel orientation and the instantaneous velocity vector at the wheel hub. In order to compute the slip angles, $\mathbf{v_f}$ and $\mathbf{v_r}$ need to be computed as translations from $\mathbf{v}$, and subsequently projected into a wheel-aligned, body-fixed reference frame.

The translational and angular velocities at the CoG are defined in the vehicle-fixed coordinate system as

$$\mathbf{v} = \begin{bmatrix} v_x, v_y, 0 \end{bmatrix}^T, \tag{3.2}$$

$$\boldsymbol{\omega} = \begin{bmatrix} 0, 0, \omega_z \end{bmatrix}^T. \tag{3.3}$$

The displacement vectors from the CoG to each respective wheel hub are defined as

$$\mathbf{R}_f = \begin{bmatrix} l_f, 0, 0 \end{bmatrix}^T, \tag{3.4}$$

$$\mathbf{R}_r = \begin{bmatrix} -l_r, 0, 0 \end{bmatrix}^T \tag{3.5}$$

With equation (2.8) we can then compute the velocities at each wheel hub, like so:

$$\mathbf{v}_f = (\mathbf{v} + \boldsymbol{\omega} \times \mathbf{R}_f) = \begin{bmatrix} v_x, v_y + \omega_z l_f, 0 \end{bmatrix}^T, \tag{3.6}$$

$$\mathbf{v}_r = (\mathbf{v} + \boldsymbol{\omega} \times \mathbf{R}_r) = \begin{bmatrix} v_x, v_y - \omega_z l_r, 0 \end{bmatrix}^T. \tag{3.7}$$

With these transformed velocities, the body side slip angles are computed as:

$$\beta_f = \tan^{-1}\left(\frac{v_y + \omega_z l_f}{\max(|v_x|, \epsilon)}\right), \tag{3.8}$$

$$\beta_r = \tan^{-1}\left(\frac{v_y - \omega_z l_r}{\max(|v_x|, \epsilon)}\right). \tag{3.9}$$

The longitudinal velocity was bounded low by $\epsilon \sim 0.1$ to prevent numerical instability at very low longitudinal speeds. Using the body side slip angles, the tire slip angles can be computed as

$$\alpha_f = \beta_f - \delta, \tag{3.10}$$
$$\alpha_r = \beta_r. \tag{3.11}$$

Assuming also small body side slip angles, the final tire slip angle equations become

$$\alpha_f = \frac{v_y + l_f \omega_z}{\max(|v_x|, \epsilon)} - \delta, \tag{3.12}$$
$$\alpha_r = \frac{v_y - l_r \omega_z}{\max(|v_x|, \epsilon)}. \tag{3.13}$$

3.1.2.6 Force Generation

Lateral tire forces act perpendicular to the wheel heading and are modeled as linearly proportional to the slip angles, where the estimated cornering stiffness parameters act as proportionality constants:

$$F_{fy} = -C_f \alpha_f, \tag{3.14}$$
$$F_{ry} = -C_r \alpha_r. \tag{3.15}$$

The negation is to model the force as restorative, opposing the slip direction.

Front tractive force was modeled as ($F_{fx} = 0$), with no brake force and no rolling resistance. The rear tractive force (F_{rx}) was derived strictly from the applied axle torque (T_r) and the effective rolling radius:

$$F_{rx} = \frac{T_r}{R_w} \tag{3.16}$$

3.1.2.7 Equations of Motion

Newton-Euler mechanics govern the dynamic state evolution. Because the equations are formulated in the vehicle's rotating body frame, fictitious Coriolis accelerations ($v_y \omega_z$ and $-v_x \omega_z$) must be superimposed to account for the non-inertial reference frame rotating relative to the global inertial plane. Resolving the planar force and moment balances yields:

$$\dot{v}_x = \frac{F_{fx} \cos\delta - F_{fy} \sin\delta + F_{rx}}{m} + v_y \omega_z, \tag{3.17}$$
$$\dot{v}_y = \frac{F_{fx} \sin\delta + F_{fy} \cos\delta + F_{ry}}{m} - v_x \omega_z, \tag{3.18}$$
$$\dot{\omega}_z = \frac{(F_{fy} \cos\delta + F_{fx} \sin\delta) l_f - l_r F_{ry}}{J_z}. \tag{3.19}$$

Setting the time derivative to zero forces the estimator to attribute parameter evolution entirely to measurement residuals rather than modeled physical laws. These five differential functions were implemented in the class method `defineEquations` of the MUSE vehicle model. The framework then used the equations to implement the estimator.

3.1.2.8 Wheel Speed Measurements

To relate wheel speed measurements to the CoG velocity, equation (2.8) was utilized with lateral-only displacement vectors from the rear wheel hub to the lateral location of the physical tires on the rear axle(s), resulting in the equations

$$\omega_{RL} = \frac{(v_x - b\omega_z)}{Rw}, \tag{3.20}$$

$$\omega_{RR} = \frac{(v_x + b\omega_z)}{Rw}. \tag{3.21}$$

3.2 Estimation using Simulated Data

The primary focus of this thesis project was on implementing an estimator using the simulation software IPG TruckMaker. The reason for developing a second estimation framework, instead of using only experimental data in combination with MUSE, was two-fold:

1. Using a simulation environment allowed for more control over driving style and driving scenario. One can vary settings such as maximum speed and road network layout, to exhibit desired dynamics for a particular test. Having this flexibility was crucial to be able to quickly iterate different tests during estimator validation. Such flexibility is inherently not present in recorded experimental data, and gathering new data is a cumbersome and time-consuming process in this particular case due to bureaucracy.

2. Quantities that are not accessible in the real world are available, inherent to the requirement to simulate all vehicle dynamics. Lateral forces, velocities and slip angles were accessible for vehicles' tires [16]. Such data was not present in the experimental data, making it difficult to verify the accuracy of the estimated TCS parameters. Having access to the quantities mentioned facilitated creating reference values for the TCS parameters.

Consequently, after realizing the shortcomings of using experimental data, the project pivoted to using IPG TruckMaker exclusively to develop, test and iterate the stiffness parameter estimator.

3.2.1 TruckMaker and Simulink

Using TruckMaker version 15.0 to run a simulation required configuring two things: a driving- and maneuver scenario, and a vehicle setup [44]. Sections 3.2.3 and 3.2.4 describe the chosen vehicle body models for the truck and trailer, respectively. The driving scenario was designed from scratch using the TruckMaker Scenario Editor. It is described in section 3.2.5.

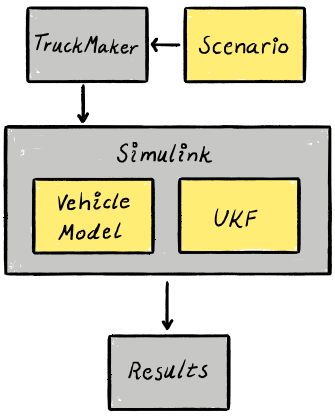

Figure 3.4: Schematic of the structure of the Simulink-TruckMaker project.

The simulation acted as a source of kinematic data, replacing the previous method of using experimental log data. Since MUSE was specifically designed for working with experimental log data, it could not be easily used without requiring an extensive time investment from the project's supervisor. To implement the simulation-based estimator, an unscented Kalman filter (UKF) had to be implemented to replace the filter design framework that had been provided by MUSE. Simulink was used to implement the new estimator, as detailed in section 3.3.

3.2.2 Measurement Noise

IPG TruckMaker provides ideal, noise-free signals. To emulate realistic sensor conditions, zero-mean Gaussian noise was added to the measurement vector z_k before being fed into the UKF. MUSE included noise models for acceleration, gyroscope and velocity [42]. These models were used in this part of the project, slightly modified to work with Simulink and IPG TruckMaker.

3.2.3 Truck Model

The truck model used in this project was based on the IPG TruckMaker example called `Demo2AxleSemiTruck4x2_Volvo`, which was included in the base installation of the software. It was configured with only one rear axle and no twin tires. Both axles had tires of the type `RT_315_70R22` from the example files of the software installation as well, with customized rolling resistance set to 0. Except for sensor mountings, there were no additional vehicle customizations that deviated from the demo model. Vehicle properties relevant to modeling the vehicle dynamics are presented in table 3.7.

The truck had two sensors mounted to its body frame:

- an IMU in the vehicle CoG, to act as a ground truth for the estimated states,
- one additional IMU in the vehicle body, slightly above and in front of the CoG, which was considered to be the analog to the IMU found in a real truck.

Both IMU had the calculation class "body mounted + no G," meaning that its reference frame was that of the truck, and all sensor readings compensated for gravity-induced effects.

Table 3.7: Physical properties of the truck model `Demo2AxleSemiTruck4x2_Volvo`.

Property	Symbol	Value	Unit
Total Mass	m	6800.00	kg
Wheelbase	L	3.570	m
Distance CoG to Front Axle	l_f	1.047	m
Distance CoG to Rear Axle	l_r	2.523	m
Yaw Moment of Inertia	J_z	12994.92	kg·m^2
CoG Height	h	0.925	m

3.2.4 Trailer Model

The trailer model was based on `Demo3AxleSemiTrailer_Volvo`, also from the included installation files. The configuration was without any modifications. The tire model used for the truck, described in the previous section, was used for the trailer as well.

Table 3.8: Physical properties of the trailer model `Demo3AxleSemiTrailer_Volvo`.

Property	Symbol	Value	Unit
Total Mass	m_{tr}	31960.00	kg
Distance CoG to Hitch	$l_{f,tr}$	4.945	m
Distance CoG to Rear Axle	$l_{r,tr}$	2.805	m
Yaw Moment of Inertia	$J_{z,tr}$	145971.764	kg·m^2
CoG Height	h_{tr}	1.950	m

3.2.5 Driving Scenario

To test whether the non-linear One-Track Model could capture the information required to estimate TCS parameters, a test track that provided enough lateral dynamics would be required. It was also desirable to have dynamics that could test how the model behaved in the case of no lateral acceleration, and also in the transitions between the two extremes.

Consequently, the track design incorporates three distinct geometries to isolate specific vehicle states. A steady-state circle provides constant lateral acceleration, facilitating the identification of cornering stiffness via sustained excitation. A straight segment serves as a control to evaluate estimator convergence and stability in the absence of lateral information. Finally, a figure-8 configuration integrates steady-state maneuvers with transient transitions between lobes, challenging the model's capacity to handle rapid phase reversals and non-linear dynamics between opposing lateral load cases.

The test track used in this project is shown in figure 3.5. It was created using the IPG TruckMaker Scenario Editor. There were three routes defined on the test track:

Route 0: A chain of all three sections with two laps in the steady-state circle, then into the straight and finally an infinite loop in the figure 8. The max velocity in each section was roughly 60 km s^{-1}, 90 km s^{-1} and 40 km s^{-1}, respectively.

Route 1: The second section and the third section, starting in the straight, ending in an infinite loop of the figure 8.

Route 2: Only the first section, the steady-state circle, being driven in an infinite loop.

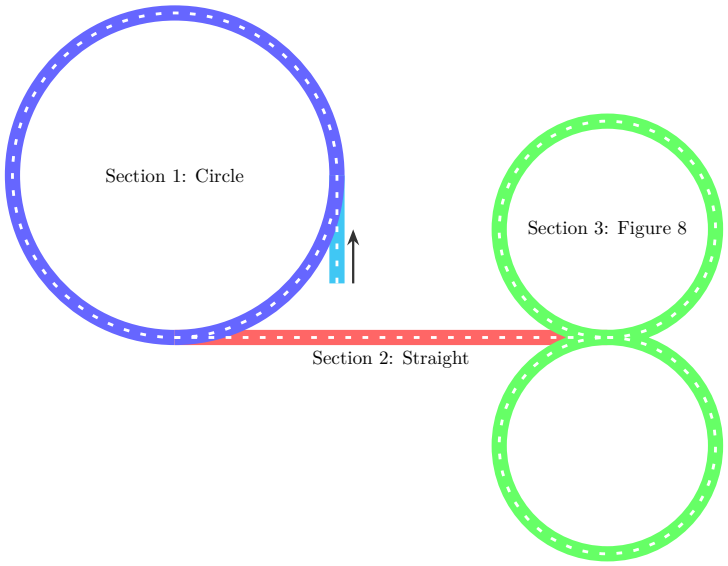

Figure 3.5: The simulated scenario. The first section was a circle of radius 100 m. The second section was a 700 m straight and the third section was a figure eight where each lobe had a radius of 50 m.

3.3 Tractor Dynamics Filter Implementation

This section presents the nonlinear state estimation framework developed in this work for reconstructing tractor longitudinal (x-direction) and lateral (y-direction) dynamics. The estimator is based on a UKF, implemented in MATLAB/Simulink, and evaluated through co-simulation with IPG TruckMaker, which supplies both input signals and sensor measurements.

3.3.1 Addtional Modeling Assumptions

To establish a tractable yet accurate estimation problem in IPG Truckmaker, the following/additional assumptions are adopted for the filter design.

- Process and measurement uncertainties are modeled as additive zero-mean white Gaussian noise (ZWGN) with covariance matrices Q and R, respectively.
- All external inputs and measurements are provided by the IPG TruckMaker simulation environment, ensuring a consistent and repeatable evaluation framework.

3.3.2 Stochastic State-Space Model

The vehicle dynamics are represented as a nonlinear discrete-time state-space system. This formulation separates the deterministic evolution of the system from stochastic uncertainties, providing a natural foundation for Bayesian filtering.

$$x_k = f(x_{k-1}, u_k\,; p) + w_k, \quad w_k \sim \mathcal{N}(0, Q) \tag{3.22}$$
$$z_k = h(x_k, u_k\,; p) + v_k, \quad v_k \sim \mathcal{N}(0, R) \tag{3.23}$$

In these equations,

- $x_k \in \mathbb{R}^5$ is the augmented state vector,
- u_k contains driver inputs from TruckMaker,
- p represents constant physical vehicle parameters,
- z_k is the measurement vector,
- w_k and v_k are process and measurement noise, respectively.

The UKF is employed to approximate the posterior distribution $p(x_k|z_{1:k})$. The UKF does not require explicit linearization of the nonlinear functions f and h, making it better suited for highly nonlinear vehicle dynamics.

3.3.3 State, Input and Measurement Definitions

Before delving into the filter mechanics and vehicle modeling, it is essential to define the quantities that are estimated, controlled, and measured.

3.3.3.1 State Vector

The UKF estimates a 5-dimensional state vector that combines vehicle motion states with unknown tire parameters. This augmentation allows simultaneous estimation of both the vehicle's dynamic behavior and the uncertain tire characteristics. Table 3.10 shows the values used for the process noise of the model.

Table 3.9: State vector definition with initial values.

Symbol	Description	Unit	Initial Value
v_x	Longitudinal velocity at COG	$\mathrm{m\,s^{-1}}$	15
v_y	Lateral velocity at COG	$\mathrm{m\,s^{-1}}$	0.1
ω_z	Yaw rate	$\mathrm{rad\,s^{-1}}$	0.1
C_f	Front tire cornering stiffness	$\mathrm{rad^{-1}}$	7.5
C_r	Rear tire cornering stiffness	$\mathrm{rad^{-1}}$	7.5

Table 3.10: Process noise matrix Q and its values.

Element	State	Variance	Unit
Q_{11}	v_x	2×10^{-2}	$\mathrm{m^2/s^2}$
Q_{22}	v_y	2×10^{-2}	$\mathrm{m^2/s^2}$
Q_{33}	ω_z	3×10^{-4}	$\mathrm{rad^2/s^2}$
Q_{44}	C_f	0	$1/\mathrm{rad^2}$
Q_{55}	C_r	0	$1/\mathrm{rad^2}$

3.3.3.2 Control Inputs

To mitigate modeling uncertainty inherent in the actuator plant dynamics, the state estimator utilizes low-level actuator states as control inputs rather than high-level driver demands generated by the IPG TruckMaker driver model. This was a design choice to bypass the nonlinear mapping and propagation latencies within the signal chain, ensuring the estimator inputs remain directly coupled to the vehicle's kinematic and kinetic force generation mechanisms.

Table 3.11: Control input signals from IPG TruckMaker

Symbol	Description	Unit	Source
δ	Steering-to-road angle	rad	Driver steering input
T_{RL}	Rear left wheel torque	Nm	Powertrain model
T_{RR}	Rear right wheel torque	Nm	Powertrain model

3.3.3.3 Measurement Signals

The UKF fuses information from available sensors in the IPG TruckMaker environment. The measurement configuration adapts based on velocity sensor availability.

Table 3.12: Available sensors and measurement signals

Symbol	Description	Sensor	Unit
a_x	Longitudinal acceleration	IMU	m/s^2
a_y	Lateral acceleration	IMU	m/s^2
v_x	Longitudinal velocity at sensor location	Velocity sensor	m/s
v_y	Lateral velocity at sensor location	Velocity sensor	m/s
ω_z	Yaw rate	IMU	rad/s
ω_{RL}	Rear left wheel speed	Wheel speed sensor	rad/s
ω_{RR}	Rear right wheel speed	Wheel speed sensor	rad/s

Table 3.13: Measurement noise matrix R and its values.

Element	Measurement	Variance	Unit
R_{11}	a_x	$1/3 \times 2$	m^2/s^4
R_{22}	a_y	$1/3 \times 2$	m^2/s^4
R_{33}	v_x	$1/3 \times 2 \times 10^{-1}$	m^2/s^2
R_{44}	v_y	$1/3 \times 2 \times 10^{-1}$	m^2/s^2
R_{55}	ω_z	$1/3 \times 5 \times 10^{-2}$	rad^2/s^2
R_{66}	ω_{RL}	$1/3 \times 5 \times 10^{-2}$	rad^2/s^2
R_{77}	ω_{RR}	$1/3 \times 5 \times 10^{-2}$	rad^2/s^2

In practical automotive applications, direct measurements of longitudinal and lateral velocity are available from dedicated velocity sensors (e.g., radar, Ground Truth)

mounted at a known position on the vehicle. These measurements offer accurate velocity information.

However, to simulate a realistic scenario where the velocity sensor signal is lost (e.g., sensor failure or environmental interference), the velocity measurements v_x and v_y are deactivated after a predetermined time threshold. In this sensor-denied operating mode, the estimator must rely solely on IMU and wheel speed measurements.

During sensor-denied operation, the individual wheel speed sensors ω_{RL} and ω_{RR} provide the primary source of information for longitudinal motion. It is important to emphasize that when velocity sensor measurements are available, the wheel speed measurements are not used by the estimator. The high-quality velocity signals are sufficient for accurate state estimation, and the wheel speed sensors are only activated as a fallback when the primary velocity sensor is lost. This selective use of sensors ensures optimal performance under normal conditions while maintaining robustness during sensor outages.

Thus, the measurement vector adapts based on velocity sensor availability:

- **Velocity sensor available:** $z_k = \begin{bmatrix} a_x & a_y & v_x & v_y & \omega_z \end{bmatrix}^T$
- **Velocity sensor denied:** $z_k = \begin{bmatrix} a_x & a_y & \omega_z & \omega_{RL} & \omega_{RR} \end{bmatrix}^T$

This setup allows evaluation of the UKF's ability to maintain accurate state estimates during periods without absolute velocity references, transitioning seamlessly from velocity-aided to velocity-denied operation.

3.3.3.4 Constant Parameters

The vehicle parameters listed in Table 3.14 are assumed known and constant throughout the estimation. These values are obtained directly from the IPG TruckMaker vehicle model.

Table 3.14: Constant vehicle parameters

Symbol	Description	Symbol	Description
m	Vehicle mass	l_f	Distance: COG to front axle
J_z	Yaw moment of inertia	l_r	Distance: COG to rear axle
L	Wheelbase ($l_f + l_r$)	h_{CoG}	COG height
R_w	Wheel radius	b	Track width
h_{hitch}	Hitch height		

3.3.4 Vehicle Kinematics and Dynamics

With the parameter, state, input, and measurement definitions in place, we now describe the vehicle model that forms the core of the UKF prediction step. The model is based on the nonlinear single-track (bicycle) representation, previously

shown in figure 3.3, which captures the essential longitudinal and lateral dynamics while maintaining computational efficiency.

3.3.4.1 Equations of Motion

The vehicle's planar motion is governed by three coupled differential equations, derived from Newton's second law applied to the free-body diagram of the vehicle model, shown in Figure 3.3. It should be noted that the vehicle is rear axle driven, equivalent to $F_{fx} = 0$.

The longitudinal dynamics describe how the forward velocity changes under the influence of longitudinal and lateral forces:

$$\dot{v}_x = \frac{1}{m} \left(F_{rx} - F_{fy} \sin \delta \right) + v_y \omega_z \tag{3.24}$$

The lateral dynamics capture the development of side-slip velocity, which is crucial for cornering behavior:

$$\dot{v}_y = \frac{1}{m} \left(F_{fy} \cos \delta + F_{ry} \right) - v_x \omega_z \tag{3.25}$$

Finally, the yaw dynamics determine the rotational acceleration of the vehicle about its vertical axis:

$$\dot{\omega}_z = \frac{1}{J_z} \left(l_f F_{fy} \cos \delta - l_r F_{ry} \right) \tag{3.26}$$

These three equations form the core of the prediction model. However, to evaluate them, we need expressions for the tire forces F_{fy}, F_{ry}, and F_{rx}, which in turn depend on the vehicle kinematics.

3.3.4.2 Velocity Transformation and Slip Angle Calculation

To accurately compute the slip angles at each axle, we first determine the velocity at the front and rear contact patches, where the F_{fz}, F_{rz} are drawn in Figure 3.6. This is achieved by transforming the center of gravity CoG velocity and adding rotational contributions.

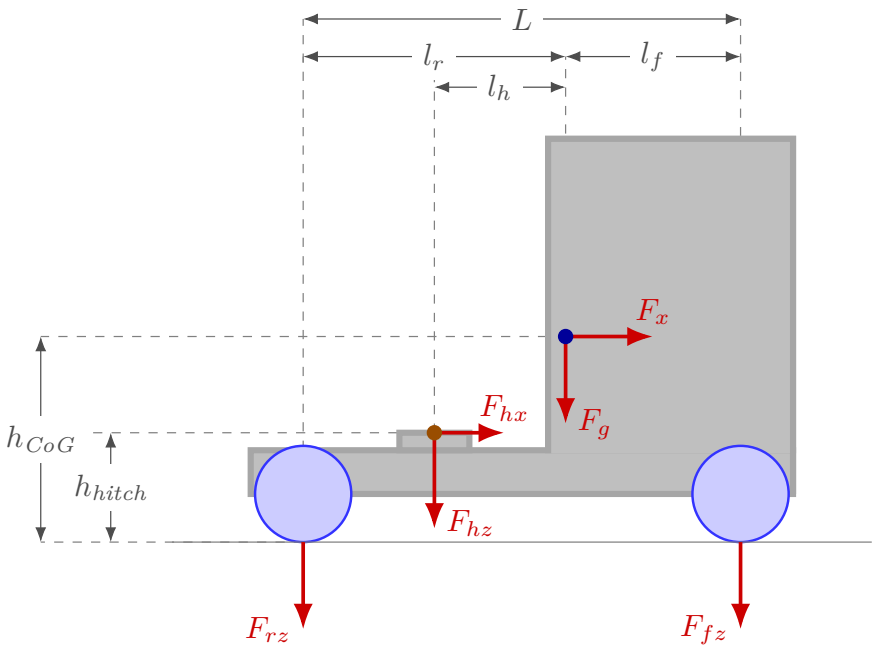

Figure 3.6: Illustration of simplified longitudinal load transfer. The orange node indicates the hitch position, and the blue node represents the center of gravity.

The velocity at the CoG is defined in the vehicle-fixed coordinate system as:

$$\mathbf{v}_{cog} = \begin{bmatrix} v_x \\ v_y \\ 0 \end{bmatrix}, \quad \boldsymbol{\omega} = \begin{bmatrix} 0 \\ 0 \\ \omega_z \end{bmatrix} \tag{3.27}$$

The position vectors from the COG to the front and rear axle contact points are defined as:

$$\mathbf{R}_f = \mathbf{p}_{fax} - \mathbf{p}_{cog} \tag{3.28}$$
$$\mathbf{R}_r = \mathbf{p}_{rax} - \mathbf{p}_{cog} \tag{3.29}$$

These vectors include vertical offsets to account for axle height differences relative to the COG.

Using rigid body kinematics, the velocity at each axle is computed as:

$$\mathbf{v}_f = \mathbf{R}(\delta)^T \left(\mathbf{v}_{cog} + \boldsymbol{\omega} \times \mathbf{R}_f\right) \tag{3.30}$$
$$\mathbf{v}_r = \mathbf{v}_{cog} + \boldsymbol{\omega} \times \mathbf{R}_r \tag{3.31}$$

The rotation matrix $\mathbf{R}(\delta)$ transforms the vehicle-fixed front axle velocity into the front wheel coordinate system, accounting for the steering to road angle δ:

$$\mathbf{R}(\delta) = \begin{bmatrix} \cos\delta & -\sin\delta & 0 \\ \sin\delta & \cos\delta & 0 \\ 0 & 0 & 1 \end{bmatrix} \tag{3.32}$$

With these transformed velocities, the tire slip angles at contact patch are computed as:

$$\alpha_f = \tan^{-1}\left(\frac{v_{fy}}{\max(|v_{fx}|, \epsilon)}\right) \tag{3.33}$$

$$\alpha_r = \tan^{-1}\left(\frac{v_{ry}}{\max(|v_{rx}|, \epsilon)}\right) \tag{3.34}$$

A small regularization term ϵ is introduced in the denominator to prevent numerical instability at very low longitudinal speeds.

3.3.4.3 Longitudinal Force

The total longitudinal force acting on the vehicle is derived from the drive wheel torques and braking forces:

$$F_{rx} = \frac{T_{RL} + T_{RR}}{R_w} + F_{x,brake} \tag{3.35}$$

Here, $F_{x,brake}$ represents the sum of front and rear braking forces, provided by the TruckMaker model. This force drives the longitudinal acceleration and influences the load transfer discussed next.

3.3.4.4 Dynamic Load Transfer

When the vehicle accelerates or brakes, vertical loads shift between the front and rear axles. This load transfer significantly affects tire grip and must be accounted for in the lateral force model.

The longitudinal acceleration is first computed from the net longitudinal force and kinematic coupling:

$$a_x = \frac{F_x}{m} + v_y\omega_z \tag{3.36}$$

The dynamic vertical loads is approximated/estimated by following, see Figure 3.6:

$$F_{fz} = \frac{mgl_r}{L} - \frac{ma_x h_{CoG}}{L} \tag{3.37}$$

$$F_{rz} = \frac{mgl_f}{L} + \frac{ma_x h_{CoG}}{L} \tag{3.38}$$

$$\tag{3.39}$$

These expressions show that acceleration shifts load to the rear axle, while braking shifts load to the front axle.

3.3.4.5 Lateral Tire Forces

With the slip angles and vertical loads determined, the lateral tire forces can be computed using a linear tire model. The lateral force is proportional to the slip angle, with the cornering stiffness scaling the vertical load:

$$F_{fy} = -C_f \alpha_f F_{fz} \tag{3.40}$$

$$F_{ry} = -C_r \alpha_r F_{rz} \tag{3.41}$$

The negative sign ensures that the lateral force opposes the slip angle, consistent with the SAE sign convention. This linear approximation is valid for small slip angles (typically $|\alpha| < 5°$), which covers normal driving conditions.

At this point, all quantities needed to evaluate the equations of motion are available. The model therefore forms a closed system that can be propagated forward in time, forming the basis for the UKF prediction step.

3.3.4.6 UKF Prediction Step

For each sigma point $\mathcal{X}_{k-1}^{(i)}$, the vehicle dynamics model $f(\cdot)$ is evaluated to obtain the predicted sigma points at time k:

$$\mathcal{X}_{k|k-1}^{(i)} = \mathcal{X}_{k-1}^{(i)} + T_s \cdot f(\mathcal{X}_{k-1}^{(i)}, u_k, p) \tag{3.42}$$

The predicted state mean and covariance are then computed as the weighted average of the propagated sigma points:

$$\hat{x}_k^- = \sum_{i=0}^{2n} W_i^{(m)} \mathcal{X}_{k|k-1}^{(i)} \tag{3.43}$$

$$\hat{P}_k^- = \sum_{i=0}^{2n} W_i^{(c)} (\mathcal{X}_{k|k-1}^{(i)} - \hat{x}_k)(\mathcal{X}_{k|k-1}^{(i)} - \hat{x}_k)^T + Q \tag{3.44}$$

3.3.5 Measurement Model

With the vehicle dynamics model established, we now turn to the measurement model, which relates the system states to the sensor outputs provided by IPG TruckMaker. An accurate measurement model is essential for the UKF update step, as it defines how the predicted states map to the observed sensor signals.

The measurement function depends on whether the velocity sensor data is available or not.

3.3.5.1 IMU Acceleration Model

The IMU is a critical sensor providing accelerations in the vehicle-fixed coordinate system. Starting from rigid body kinematics, the acceleration at the IMU location is given by:

$$\mathbf{a}_{\boldsymbol{IMU}} = \dot{\mathbf{v}} + \dot{\boldsymbol{\omega}} \times \mathbf{R}_{\boldsymbol{IMU}} + \boldsymbol{\omega} \times (\boldsymbol{\omega} \times \mathbf{R}_{\boldsymbol{IMU}}) \tag{3.45}$$

where $\dot{\mathbf{v}}$ is the acceleration of the CoG, $\dot{\boldsymbol{\omega}}$ is the angular acceleration, $\boldsymbol{\omega}$ is the angular velocity, and $\mathbf{R}_{IMU}$ is the position vector from COG to the IMU.

3.3.5.2 Velocity Measurements

Since the velocity sensor is mounted at a known position $\mathbf{R}_{sens}$ relative to the vehicle's CoG. Using rigid body kinematics, the velocity at the sensor location is given by equation 2.8:

$$\mathbf{v}_{sens} = \mathbf{v} + \boldsymbol{\omega} \times \mathbf{R}_{sens} \tag{3.46}$$

where $\mathbf{v}$ is the velocity of the CoG, $\boldsymbol{\omega}$ is the angular velocity, and $\mathbf{R}_{sen}$ is the position vector from CoG to the velocity sensor.

3.3.5.3 Wheel Speed Measurements

When the velocity sensor is unavailable, the individual wheel speed sensors ω_{RL} and ω_{RR} provide the primary source of information for longitudinal motion. Under the assumption of rolling without slip, the wheel angular velocities are modeled as:

$$\omega_{RL} = \frac{v_x - \omega_z \cdot b/2}{R_w} \tag{3.47}$$

$$\omega_{RR} = \frac{v_x + \omega_z \cdot b/2}{R_w} \tag{3.48}$$

These individual wheel speed models capture the yaw-induced velocity difference between the left and right wheels, which is essential for estimating both v_x and ω_z simultaneously.

3.3.5.4 Complete Measurement Function

The measurement function $h(x_k, u_k, p)$ adapts based on velocity sensor availability.

3.3.5.4.1 Full Measurement Set In this mode, wheel speed measurements are not used. The measurement function relies on IMU and velocity sensor measurements, with the velocity sensor transformed from COG states:

$$h(x_k, u_k, p) = \begin{bmatrix} \dot{v}_x \\ \dot{v}_y \\ v_x \\ v_y \\ \omega_z \end{bmatrix} \tag{3.49}$$

Note that the velocity measurements v_x and v_y are expressed at the sensor position $\mathbf{R}_{sens}$.

3.3.5.4.2 Reduced Measurement Set In this mode, velocity sensor measurements are unavailable. The estimator instead relies on IMU and wheel speed measurements:

$$h(x_k, u_k, p) = \begin{bmatrix} \dot{v}_x \\ \dot{v}_y \\ \omega_z \\ w_{RL} \\ w_{RR} \end{bmatrix} \tag{3.50}$$

The estimator operates in two distinct modes. Under normal conditions with the velocity sensor available, high-quality velocity measurements transformed to the sensor location provide accurate state estimation. When the velocity sensor is lost, the system seamlessly transitions to a fallback mode using only IMU and individual wheel speed measurements. This dual-mode operation allows performance across a wide range of driving scenarios.

3.3.5.5 Measurement Prediction

Having a measurement model the new sigma points are generated from the predicted distribution and propagated through the measurement model $h(x_k, u_k, p)$, which includes the IMU accelerations, velocity transformations, and wheel speed calculations:

$$\mathcal{Z}_k^{(i)} = h(\mathcal{X}_{k|k-1}^{(i)}, u_k, p) \tag{3.51}$$

The predicted measurement mean and innovation covariance are:

$$\hat{z}_k = \sum_{i=0}^{2n} W_i^{(m)} \mathcal{Z}_k^{(i)} \tag{3.52}$$

$$S_k = \sum_{i=0}^{2n} W_i^{(c)} (\mathcal{Z}_k^{(i)} - \hat{z}_k)(\mathcal{Z}_k^{(i)} - \hat{z}_k)^T + R \tag{3.53}$$

3.3.6 UKF Update Step

The cross-covariance between the state and measurement predictions is computed as:

$$C_k = \sum_{i=0}^{2n} W_i^{(c)} (\mathcal{X}_{k|k-1}^{(i)} - \hat{x}_k^-)(\mathcal{Z}_k^{(i)} - \hat{z}_k)^T \tag{3.54}$$

The Kalman gain is then:

$$K_k = C_k S_k^{-1} \tag{3.55}$$

Finally, the state estimate and covariance are updated using the actual sensor measurements z_k:

$$\hat{x}_k = \hat{x}_k^- + K_k(z_k - \hat{z}_k) \tag{3.56}$$

$$\hat{P}_k = \hat{P}_k^- - K_k S_k K_k^T \tag{3.57}$$

This structure enables real-time estimation of both vehicle motion states and uncertain tire parameters, providing a complete picture of the tractor's lateral dynamics from standard automotive sensors. The UKF's ability to handle nonlinearities without linearization makes it particularly well-suited for this application, where the product terms in the IMU model introduce strong coupling between the longitudinal and lateral directions.

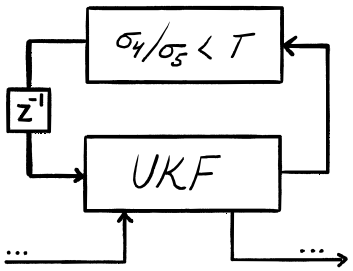

Figure 3.7: The update strategy was added adjacent to the UKF, which sent a boolean indicator whether the filter should update TCS or not.

3.4 UKF Update Stragety

One of the stated research questions in section 1.3 mentions a "parameter update strategy". Most filter implementations described so far have had the TCS parameters updated in each timestep. Whether or not this is a good strategy will be apparent when looking at the results.

Another strategy that was implemented, to be described in this section, was based on the idea that the observability metrics described in section 2.6 would perhaps be useful as indicators for when a given state trajectory could provide useful information about the lateral dynamics of the truck. The strategy used the singular values (σ_i) from a sliding-window estimation of the local observability Gramian from (2.66) to compute the metric formulated in (2.59). This metric was then used by the UKF to decide whether or not to update the estimated TCS parameters in each time step.

3.4.1 Implementation of Observability Indicator

Figure 3.7 shows how this update strategy was schematically incorporated into the Simulink model. The UKF output state predictions for some time step, and fed them to an adjacent function block that computed the metric formulated in (2.59). The result of the computation was fed back to the UKF in the immediate subsequent time step.

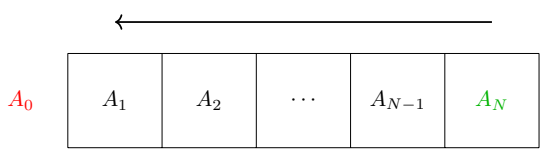

Figure 3.8: Working principle of the sliding window buffer for A_k. At each timestep k, the array is left-shifted, expelling A_0 and inserting $A_N = A_k$ to the right.

The observability metric was computed by constructing the discrete local observability Gramian W_o^d over a sliding temporal window of $N = 10$ samples. In each time step, the function block computed the corresponding time-varying Jacobians A_k and C_k using the same physical vehicle parameters as in the physical model of the filter and the state estimates fed from the UKF. The resulting matrices got shifted into their corresponding sliding window buffers, at the same time shifting out the previous oldest entry. Figure 3.8 shows the sliding buffer for the state transition matrix.

During initialization of the filter, specifically the time interval $0 < t < (N-1)\Delta t$, the Gramian was approximated using the static linear time-invariant observability matrix $W_o^d \approx \mathcal{O}^\mathsf{T}\mathcal{O}$ from (2.69). Once the sliding window was fully populated, the Gramian was computed according to (2.66).

The singular values of W_o^d were extracted at each time step, using MATLAB's singular value decomposition `svd()`. The resulting σ_i was stabilized through a moving-average low-pass filter utilizing a sliding window of $N = 100$, similarly to the one shown in figure 3.8. The observability metric (2.59) was then used with a threshold $\mathcal{T}$ to yield a boolean output signal defined to be

$$\mathcal{U} := \begin{cases} 1 & \text{if } \langle\sigma_4\rangle/\langle\sigma_5\rangle < \mathcal{T}, \\ 0 & \text{if } \langle\sigma_4\rangle/\langle\sigma_5\rangle \geq \mathcal{T}, \end{cases} \tag{3.58}$$

where $\langle\cdot\rangle$ denotes the moving average. An empirical threshold of $\mathcal{T} = 50$ was found using Route 0 of the scenario described in section 3.2.5: the observability metric was

below the threshold value during maneuvers with sufficient lateral dynamics for the specified scenario.

3.4.2 Conditional Update of Stiffness Parameters

The update strategy was implemented by making (3.56) conditional on the boolean signal (3.58). Expressed in the same notation as in section 3.3.6, with $[\,\cdot\,]_i$ denoting vector component i, the conditional update step used as the update strategy was

$$[\hat{x}_k]_i = \left\{ \begin{array}{ll} \left[\hat{x}_k^- + K_k(z_k - \hat{z}_k)\right]_i, & \text{if } \mathcal{U} = 1 \\ \left[\hat{x}_k^-\right]_i, & \text{if } \mathcal{U} = 0 \end{array} \right\}, \forall i \in \{4, 5\}. \tag{3.59}$$

The MATLAB implementation of this update strategy can be found in [43].

3.4.3 Quantifying Stiffness Error Propagation

If either C_f or C_r are wrong, the physics calculations for lateral force at each axle will be wrong, affecting estimated lateral dynamics. To quantify how an error in axle cornering stiffness propagates to the estimated states corresponding to lateral dynamics, the estimator described in section 3.3 was temporarily configured to keep the states C_f and C_r fixed (i.e., they were not updated). This was implemented using the indicator signal (3.58) from above, setting $\mathcal{U} = 0$. The effect of this was to never apply the computed Kalman gain to either estimate, keeping the initial values of C_f and C_r when running the filter.

Keeping only one of the two stiffness states fixed while estimating the other would be counter-productive to quantifying error propagation, since the filter would then try to balance the free state to compensate for the error due to the two being coupled through the vehicle's moment of inertia. Hence, both had to be kept fixed. A sweep over C_r was performed while only using a single value for C_f, in order to be able to distinguish how a single axis affects the lateral dynamics. Sweeping both would yield a superposition of the errors introduced at each axle, making the results less comprehensible.

With varying initial values $C_r \in \{10, 11, 12, 13, 14\}$ and $C_f = 9.5$, the truck was driven around Route 0 with always available velocity measurements. The choice of initial values was based on empirical findings after running the One Track estimator in section 3.3 around that same route, in an identical setup, differing only in initial values and $\mathcal{U} = 1$. The choice of keeping C_f fixed was motivated by observing that C_f converged to roughly 9.5 when testing different longitudinal velocities $v_x \geq 40\,\mathrm{km\,h^{-1}}$ when driving the truck around Route 2, whereas C_r fluctuated a lot more.

3.5 Estimation of Individual Tire Stiffness

To investigate whether individual tire cornering stiffness can be estimated for each wheel separately, a four-wheel model is developed. This model extends the single-track framework by representing each wheel independently, as illustrated in Figure

3.9. The underlying tractor model, UKF framework, and sensor models remain unchanged unless explicitly noted.

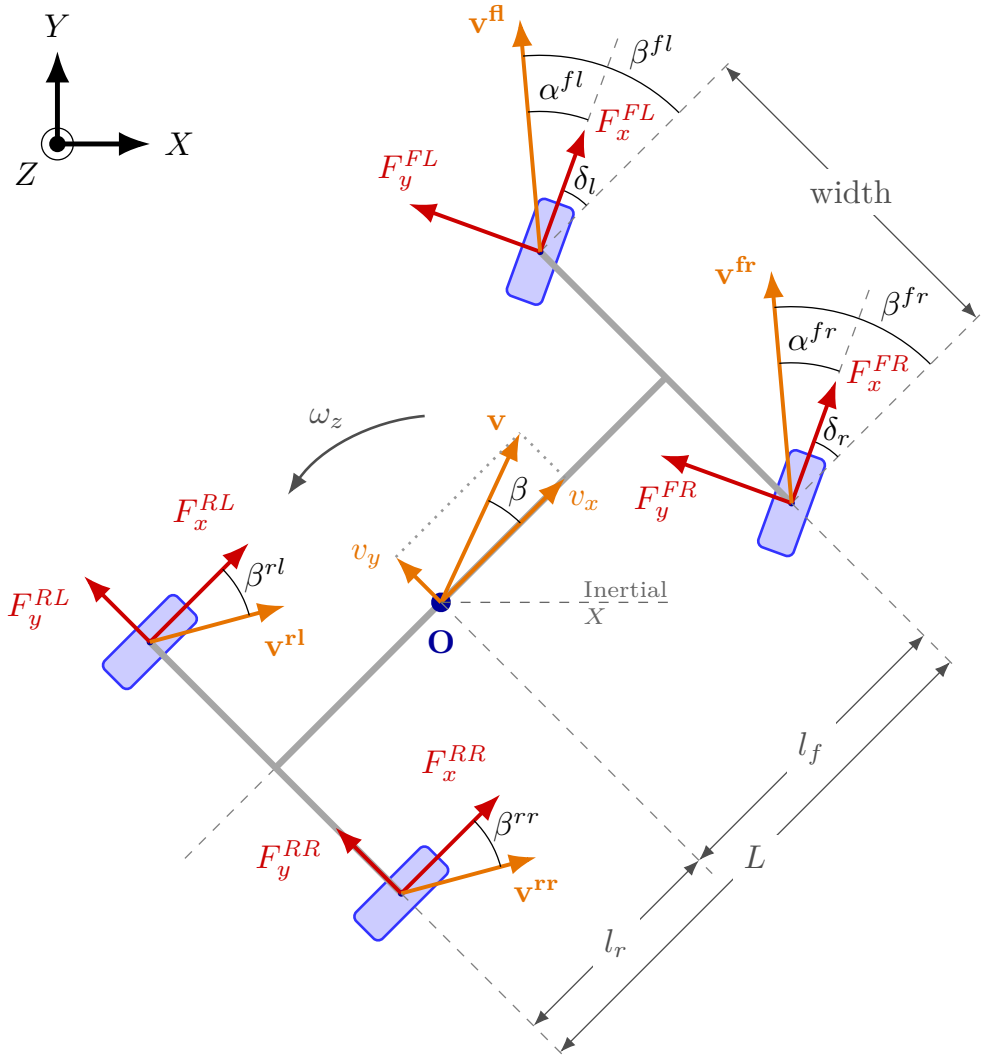

Figure 3.9: The four-wheel (two-track) vehicle model with individual cornering stiffness parameters per wheel.

3.5.1 State Vector and Control Inputs

The state vector is extended to include individual cornering stiffness for each wheel:

$$x = [v_x,\ v_y,\ \omega_z,\ C_{FL},\ C_{FR},\ C_{RL},\ C_{RR}]^T \tag{3.60}$$

where C_{FL}, C_{FR}, C_{RL}, and C_{RR} represent the cornering stiffness for the front left, front right, rear left, and rear right wheels, respectively.

The control inputs consist of individual steering angles for the front wheels and wheel torques for the rear axle:

Table 3.15: Control inputs for the four-wheel model

Symbol	Description	Unit
δ_{FL}	Front left steering angle	rad
δ_{FR}	Front right steering angle	rad
T_{RL}	Rear left wheel torque	Nm
T_{RR}	Rear right wheel torque	Nm

The rear steering angles are zero, and there is no front wheel drive.

3.5.2 Wheel Kinematics and Forces

The position of each wheel relative to the COG is given by:

$$\mathbf{R}_{FL} = \begin{bmatrix} l_f \\ w_{track}/2 \\ -h_{CoG} \end{bmatrix}, \quad \mathbf{R}_{FR} = \begin{bmatrix} l_f \\ -w_{track}/2 \\ -h_{CoG} \end{bmatrix} \tag{3.61}$$

$$\mathbf{R}_{RL} = \begin{bmatrix} -l_r \\ w_{track}/2 \\ -h_{CoG} \end{bmatrix}, \quad \mathbf{R}_{RR} = \begin{bmatrix} -l_r \\ -w_{track}/2 \\ -h_{CoG} \end{bmatrix} \tag{3.62}$$

The velocity at each wheel contact patch is computed using rigid body kinematics:

$$\mathbf{v}_j = \mathbf{v}_{\text{cog}} + \boldsymbol{\omega} \times \mathbf{R}_j, \quad j \in \{FL, FR, RL, RR\} \tag{3.63}$$

These velocities are then rotated into each wheel's local coordinate system using the steering angle:

$$\mathbf{v}_j = \mathbf{R}(\delta_j)^T \mathbf{v}_j, \qquad \mathbf{R}(\delta_j) = \begin{bmatrix} \cos\delta_j & \sin\delta_j \\ -\sin\delta_j & \cos\delta_j \end{bmatrix} \tag{3.64}$$

The slip angle for each wheel is obtained as:

$$\alpha_j = \tan^{-1}\left(\frac{v_{y,j}}{\max(|v_{x,j}|, \epsilon)}\right) \tag{3.65}$$

and the lateral tire force is modeled linearly:

$$F_{y,j} = -C_j \alpha_j \tag{3.66}$$

The wheel forces are then transformed back to the vehicle frame:

$$\mathbf{F}_j = \mathbf{R}(\delta_j) \begin{bmatrix} F_{x,j} \\ F_{y,j} \end{bmatrix} \tag{3.67}$$

For the rear wheels, where $\delta = 0$, this simplifies to $\mathbf{F}_j = [F_{x,j},\ F_{y,j}]^T$.

3.5.3 Equations of Motion

The total forces in the vehicle frame are summed:

$$F_x = \sum_j F_{x,j}, \qquad F_y = \sum_j F_{y,j} \tag{3.68}$$

which gives the accelerations:

$$\dot{v}_x = \frac{F_x}{m} + v_y \omega_z \tag{3.69}$$

$$\dot{v}_y = \frac{F_y}{m} - v_x \omega_z \tag{3.70}$$

The yaw moment includes contributions from both lateral and longitudinal forces:

$$M_z = l_f(F_{y,FL} + F_{y,FR}) - l_r(F_{y,RL} + F_{y,RR}) + \frac{b}{2}(F_{x,FR} - F_{x,FL} + F_{x,RR} - F_{x,RL}) \tag{3.71}$$

and the yaw acceleration follows as:

$$\dot{\omega}_z = \frac{M_z}{J_z} \tag{3.72}$$

3.5.4 Measurement Model

The measurement vector includes all four wheel speeds, providing additional information compared to the single-track model:

$$z_k = \begin{bmatrix} a_x & a_y & v_x & v_y & \omega_z & \omega_{FL} & \omega_{FR} & \omega_{RL} & \omega_{RR} \end{bmatrix}^T \tag{3.73}$$

The wheel angular velocities are derived from the longitudinal component of each wheel's local velocity:

$$\omega_j = \frac{v_{j,x}}{R_w}, \quad j \in \{FL, FR, RL, RR\} \tag{3.74}$$

3.6 Extension to Tractor-Trailer Configuration

This section extends the single-track tractor model from Section 3.3.4 to include a trailer unit as illustrated in Figure 3.10. Only the additional states, parameters, and dynamics introduced by the trailer are described here. The underlying tractor model, UKF framework, and sensor models remain unchanged unless explicitly noted.

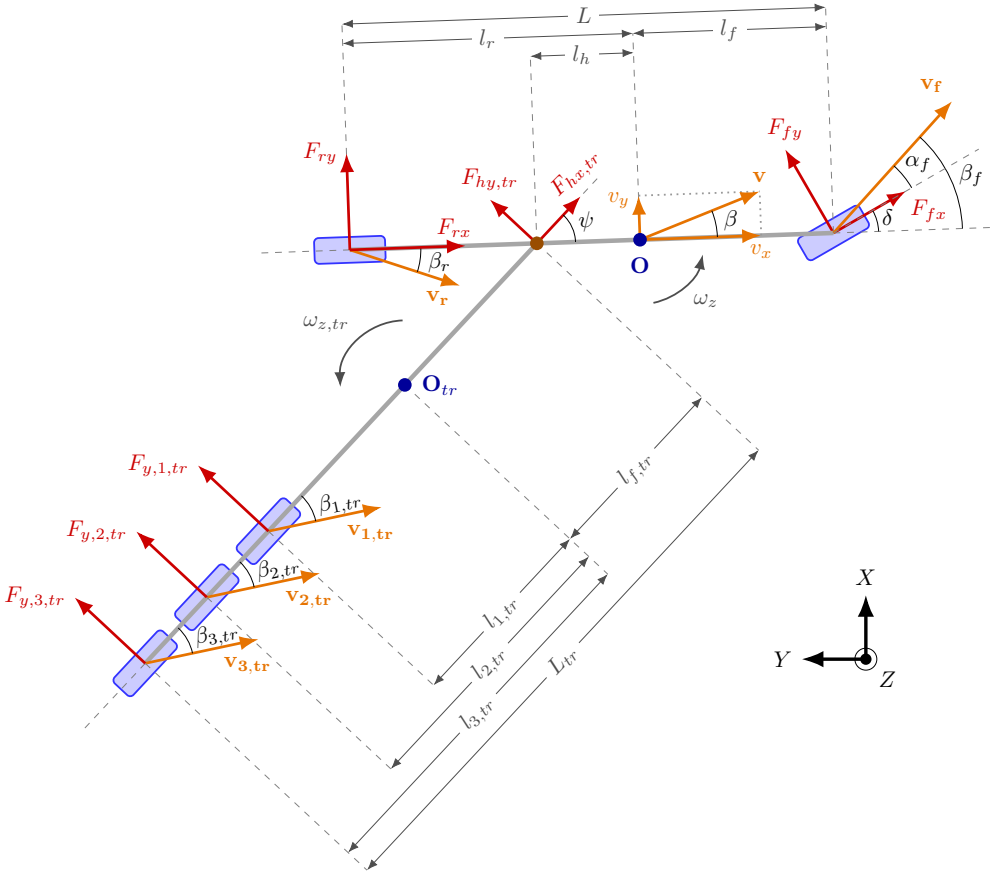

Figure 3.10: The single-track vehicle model, extended to a trailer configuration.

3.6.1 Additional States

Compared to the tractor-only model, the following three new states are added to the state vector:

Table 3.16: Additional states introduced by the trailer

Symbol	Description	Unit
ψ	Articulation angle (trailer relative to tractor)	rad
$\omega_{z,tr}$	Trailer yaw rate	rad/s
$C_{r,tr}$	Trailer equivalent cornering stiffness	1/N

The articulation angle ψ describes the relative orientation between tractor and trailer, defined as positive when the trailer rotates counter-clockwise relative to the tractor.

The trailer yaw rate $\omega_{z,tr}$ represents the rotational velocity of the trailer, and $C_{r,tr}$ is the equivalent cornering stiffness for the trailer's axles.

The full extended state vector thus becomes:

$$x = [v_x,\ v_y,\ \omega_z,\ C_f,\ C_r,\ \psi,\ \omega_{z,tr},\ C_{r,tr}]^T \tag{3.75}$$

3.6.2 Modified Control Inputs

The trailer introduces an additional control input compared to the tractor-only model:

Table 3.17: Modified control input signals from IPG TruckMaker

Symbol	Description	Unit	Change
δ	Tractor steering angle	rad	Unchanged
T_{RL}	Rear left wheel torque	Nm	Unchanged
T_{RR}	Rear right wheel torque	Nm	Unchanged
$F_{hx,tr}$	Longitudinal force at trailer hitch	N	**New input**

The longitudinal trailer hitch force $F_{hx,tr}$ is provided by the TruckMaker model and represents the longitudinal interaction between tractor and trailer. This force affects the tractor dynamics as an external force.

3.6.3 Additional Measurements

Three additional measurement signals are introduced with the trailer:

Table 3.18: Additional measurement signals from the trailer

Symbol	Description	Sensor	Unit
$\omega_{2,tr}$	Trailer middle left wheel speed	Wheel speed sensor	rad/s
$\omega_{2,tr}$	Trailer middle right wheel speed	Wheel speed sensor	rad/s
$F_{hy,tr}$	Trailer lateral force at hitch	IPG TruckMaker	N

The full measurement vector contains 10 signals: the previous 7 from the tractor model plus these 3 trailer measurements.

3.6.4 New Constant Parameters

The trailer introduces the following constant parameters:

Table 3.19: Additional constant parameters for the trailer

Symbol	Description	Unit
m_{tr}	Trailer mass	kg
$J_{z,tr}$	Trailer yaw inertia	kg·m^2
$l_{f,tr}$	Distance from hitch to trailer CoG	m
$l_{1,tr}$	Distance from CoG to trailer front axle	m
$l_{2,tr}$	Distance from CoG to trailer middle axle	m
$l_{3,tr}$	Distance from CoG to trailer rear axle	m
L_{tr}	Total wheelbase (hitch to rear axle)	m
$h_{cog,tr}$	Trailer CoG height	m
$h_{hitch,tr}$	Trailer hitch height	m

3.6.5 Hitch Coupling

The tractor and trailer are connected at the hitch point as shown in Figure 3.10. The hitch force vector consists of a longitudinal component $F_{hx,tr}$ (input) and a lateral component $F_{hy,tr}$ (measured). The hitch force is transformed from the trailer coordinate system to the tractor frame using the estimated articulation angle ψ:

$$\mathbf{F}_h = \mathbf{R}(\psi) \begin{bmatrix} F_{hx,tr} \\ F_{hy,tr} \end{bmatrix}, \quad \mathbf{R}(\psi) = \begin{bmatrix} \cos\psi & -\sin\psi \\ \sin\psi & \cos\psi \end{bmatrix} \tag{3.76}$$

3.6.6 Modified Tractor Dynamics

The tractor equations of motion are modified to include the hitch forces. The changes compared to the tractor-only model are highlighted below:

$$\dot{v}_x = \frac{1}{m}\left(F_{rx} - F_{fy}\sin\delta - F_{hx}\right) + v_y\omega_z \tag{3.77}$$

$$\dot{v}_y = \frac{1}{m}\left(F_{fy}\cos\delta + F_{ry} - F_{hy}\right) - v_x\omega_z \tag{3.78}$$

$$\dot{\omega}_z = \frac{1}{J_z}\left(l_f F_{fy}\cos\delta - l_r F_{ry} + l_h F_{hy}\right) \tag{3.79}$$

The hitch forces appear as additional external forces acting on the tractor as shown in Figure 3.10.

3.6.7 Modified Normal Forces on the Tractor

The attachment of a trailer even introduces an additional vertical load at the hitch point F_{hz}, which alters the load distribution on the tractor. The modified vertical loads on the front and rear axles are:

$$F_{fz} = \frac{mgl_r}{L} - \frac{ma_x h_{CoG}}{L} + \frac{F_{hz}(l_{hitch} - l_r)}{L} - \frac{F_{hx,}h_{hitch}}{L} \tag{3.80}$$

$$F_{rz} = \frac{mgl_f}{L} + \frac{ma_x h_{CoG}}{L} + \frac{F_{hz}(l_f - l_{hitch})}{L} + \frac{F_{hx}h_{hitch}}{L} \tag{3.81}$$

where l_{hitch} is the distance from COG to the hitch point, and h_{hitch} is the tractor hitch height. These expressions replace the load transfer equations (3.38, 3.39) and ensure that the trailer's influence on the tractor's vertical load distribution is accounted for.

3.6.8 Trailer Kinematics and Dynamics

The trailer is equipped with three axles, as illustrated in Figure 3.10. The vertical load is assumed to be equally distributed among the three axles. Each axle is modeled individually with its own slip angle and lateral force calculation.

The kinematics of the trailer are derived from the hitch point.

3.6.8.1 Hitch Velocity Transformation

The velocity at the hitch point, expressed in tractor coordinates, is transformed to the trailer coordinate system using the articulation angle ψ:

$$\mathbf{v}_{hitch,tr} = \mathbf{R}(\psi)^T \mathbf{v}_{hitch} \tag{3.82}$$

where $\mathbf{v}_{hitch} = \mathbf{v}_{cog} + \boldsymbol{\omega} \times \mathbf{R}_{hitch}$. Where $\mathbf{R}_{hitch}$ is the position vector from tractor CoG to the tractor hitch.

3.6.8.2 Trailer Axle Velocities and Slip Angles

The velocity at the trailer center of gravity CoG is computed by:

$$\mathbf{v}_{CoG,tr} = \mathbf{v}_{hitch,tr} - \boldsymbol{\omega}_{tr} \times \mathbf{R}_{CoG,tr} \tag{3.83}$$

After that the velocities at each axle are then obtained by adding the rotational contribution from the trailer yaw rate:

$$\mathbf{v}_{s,tr} = \mathbf{v}_{CoG,tr} + \boldsymbol{\omega}_{tr} \times \mathbf{R}_{s,tr} \quad s \in \{1, 2, 3\} \tag{3.84}$$

$$\tag{3.85}$$

where $\mathbf{R}_{s,tr}$ is the position vectors from the trailer CoG_{tr} to respective trailer axles.

The slip angle for each axle is computed from the longitudinal and lateral velocities:

$$\alpha_{s,tr} = \tan^{-1}\left(\frac{v_{y,s,tr}}{\max(|v_{x,s,tr}|, \epsilon)}\right) \tag{3.86}$$

3.6.8.3 Trailer Load Transfer

The vertical loads on the hitch and trailer are obtained by solving the static equilibrium equations based on the axle geometry. For a trailer with three axles at positions $l_{1,tr}$, $l_{2,tr}$, $l_{3,tr}$ relative to the CoG_{tr}, and the trailer hitch at distance $l_{f,tr}$ from the CoG_{tr}, force and moment equilibrium give:

$$F_{hz,tr} = \frac{m_{tr} g (l_{1,tr} + l_{2,tr} + l_{3,tr})}{l_{1,tr} + l_{2,tr} + l_{3,tr} + 3l_{f,tr}} \tag{3.87}$$

$$F_{z,axle} = \frac{l_{f,tr} m_{tr} g}{l_{1,tr} + l_{2,tr} + l_{3,tr} + 3l_{f,tr}} \tag{3.88}$$

The vertical load per axle $F_{z,axle}$ is the same for all three axles under the equal load distribution assumption.

3.6.8.4 Trailer Lateral Forces

The lateral tire force at each axle is modeled using a linear tire model, where the cornering stiffness scales with the vertical load:

$$F_{y,s,tr} = -C_{r,tr} \alpha_{s,tr} F_{z,axle} \tag{3.89}$$

3.6.8.5 Lateral Hitch Force

The resulting lateral hitch force is obtained from moment equilibrium about the trailer CoG, considering the contributions from all three axles.

$$F_{hy,tr} = \sum_{i}^{3} \frac{l_{i,tr} Fy, i, tr}{l_{f,tr}} \quad i \in \{1, 2, 3\} \tag{3.90}$$

Note that $F_{hy,tr}$ is the lateral hitch force computed from the model, which is compared to the measured $F_{hy,tr}$ in the UKF measurement update steg. This provides a direct link between the model and the measurement for estimating $C_{r,tr}$.

3.6.8.6 Trailer Dynamics

The trailer contributes two additional differential equations to the system. The articulation angle dynamics describe how the relative angle changes:

$$\dot{\psi} = \omega_{z,tr} - \omega_z \tag{3.91}$$

The trailer yaw acceleration is determined by the moment from the hitch force and the tire forces about the trailer COG:

$$\dot{\omega}_{z,tr} = \frac{1}{J_{z,tr}} \left(l_{f,tr} F_{hy,tr} - l_{1,tr} F_{y,1,tr} - l_{2,tr} F_{y,2,tr} - l_{3,tr} F_{y,3,tr} \right) \tag{3.92}$$

3.6.8.7 Trailer Wheel Speed Measurements

The trailer wheel speeds are modeled similarly to the tractor rear wheels, using the longitudinal velocity at the middle axle:

$$\omega_{2,tr} = \frac{v_{x,2,tr} - \omega_{z,tr} \cdot b_{tr}/2}{R_w} \tag{3.93}$$

$$\omega_{2,tr} = \frac{v_{x,2,tr} + \omega_{z,tr} \cdot b_{tr}/2}{R_w} \tag{3.94}$$

These wheel speed measurements provide additional information for estimating the trailer's longitudinal velocity and yaw rate.

3.6.9 Discretization

For digital implementation on a computer, the continuous-time vehicle model must be discretized. The UKF operates in discrete time, requiring a discrete-time representation of the system dynamics.

The continuous-time state-space model is given by:

$$\dot{x}(t) = f_c(x(t), u(t); p) + w(t), \quad w(t) \sim \mathcal{N}(0, Q_c) \tag{3.95}$$

$$z(t) = h_c(x(t), u(t); p) + v(t), \quad v(t) \sim \mathcal{N}(0, R_c) \tag{3.96}$$

Using Euler forward discretization with a fixed sampling time T_s, the discrete-time model becomes:

$$x_{k+1} = x_k + T_s \cdot f_c(x_k, u_k; p) + w_k, \quad w_k \sim \mathcal{N}(0, Q_d) \tag{3.97}$$

$$z_k = h_c(x_k, u_k; p) + v_k, \quad v_k \sim \mathcal{N}(0, R_d) \tag{3.98}$$

The discrete-time noise covariances are related to their continuous-time counterparts by:

$$Q_d \approx Q_c \cdot T_s \tag{3.99}$$

$$R_d = R_c \tag{3.100}$$

This first-order approximation is sufficient for the sampling rates used in this work ($T_s = 0.01$ s), as the vehicle dynamics are significantly slower than the sampling frequency. The discretized model forms the basis for the UKF prediction step, where each sigma point is propagated forward in time using the discretized dynamics.

3.6.9.1 Consistency Evaluation Using NEES

The NEES is computed for each time step using the estimated state $\hat{x}_k$, the true reference state x_k, and the filter covariance $\hat{P}_k$. The NEES value is then calculated as:

$$(NEES)_k = (x_k - \hat{x}_k)^T P_k^{-1} (x_k - \hat{x}_k) \tag{3.101}$$

Values exceeding a threshold (e.g., $(NEES)_k > 100$) are discarded to avoid numerical outliers.

The NEES results are visualized using two plots:

1. **Time series plot:** The NEES values are plotted over time together with the theoretical chi-squared confidence bounds. The bounds are computed using the inverse chi-squared cumulative distribution function, which in MATLAB is implemented as `chi2inv`:

   $$\text{Lower bound} = \chi^{-2}_{n,\alpha/2}, \quad \text{Upper bound} = \chi^{-2}_{n,1-\alpha/2} \tag{3.102}$$

   where α is the significance level ($\alpha = 0.01$ or $\alpha = 0.05$).

2. **Histogram plot:** The empirical probability density function of NEES is compared to the theoretical chi-squared PDF. The theoretical PDF is computed using the MATLAB function `chi2pdf`.

   This provides a visual assessment of how well the empirical distribution matches the theoretical distribution.

If the NEES values predominantly lie within the confidence bounds and the empirical PDF follows the theoretical chi-squared distribution, the filter is considered consistent.

4

Results

The following sections shows the results from evaluating the estimators described in the methodology, presented in the following order:

1. Estimation results from the real-world data estimator in section 3.1.
2. Results for the One-Track tractor model described in section 3.3.4.
3. Two-Track Model estimation results for the model in section 3.5.
4. Finally, the results for the full articulated vehicle configuration from section 3.6.

4.1 MUSE Results

This section contains the results from running the MUSE-based estimator described in section 3.1. Each of the five states has a corresponding figure, showing the estimate as a function of time with uncertainty and ground truth (if available).

Figure 4.1 shows the longitudinal acceleration. The ground truth measurements are rather noisy when compared to the estimated value, making it difficult to tell whether the estimate is accurate or not. It seems to follow the moving average of the ground truth, and the uncertainty bounds of a_x are within the noise peaks of the ground truth.

Lateral acceleration on the other hand, shown in figure 4.2, has uncertainty bounds that are almost the double of the largest amplitude of the noise peaks, with an estimate that shows similar noise characteristics to that of the ground truth. Despite that, both estimates follow the apparent mean and trend of their corresponding reference. Both figures 4.1 and 4.2 show a significantly reduced uncertainty between 50 s to 60 s, with notable fluctuations towards the end.

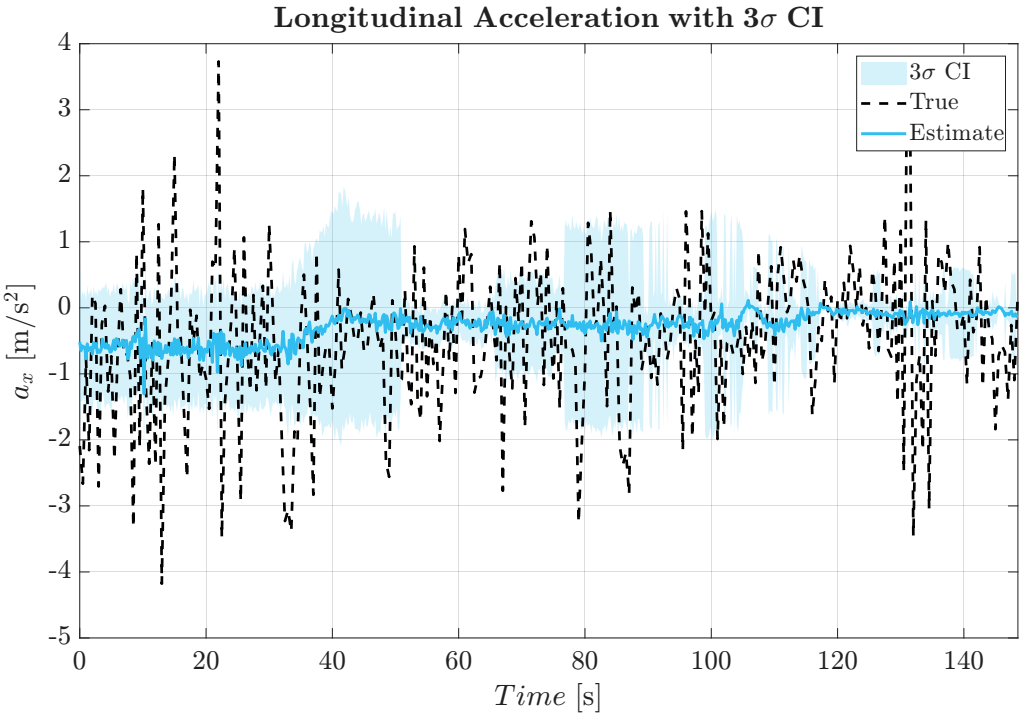

Figure 4.1: Experimental estimation results for a_x. The dashed line shows the ground truth measurements, while the blue line shows the estimated state. The shaded region around the blue estimate shows the 3σ confidence interval.

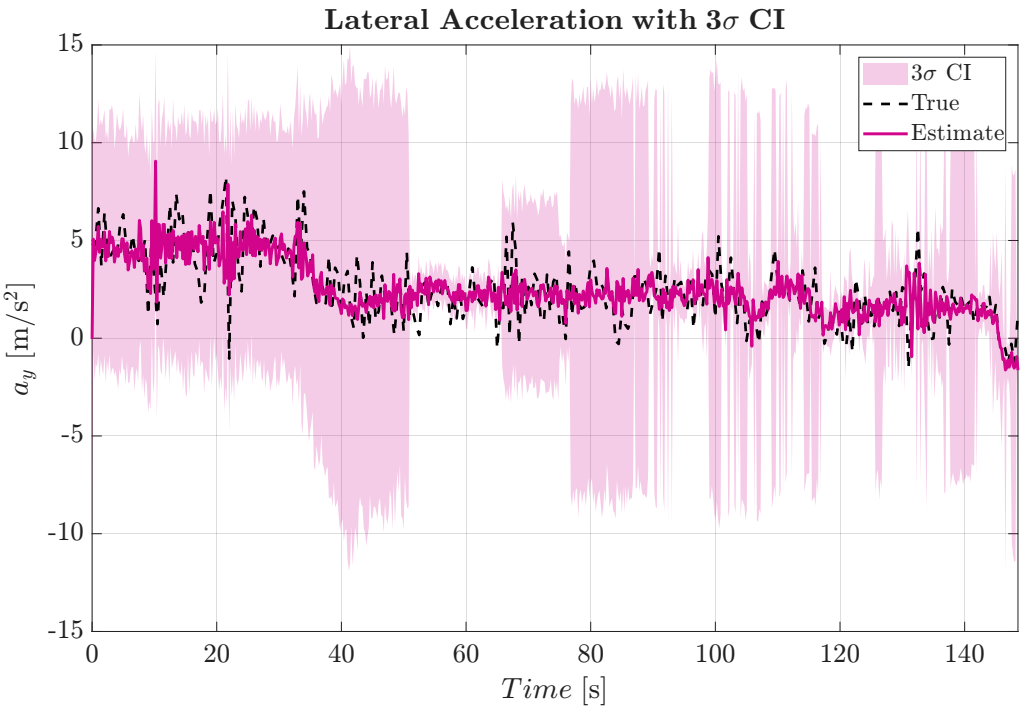

Figure 4.2: Experimental estimation results for a_y. Ground truth measurements are shown by the black dashed line, while the pink line shows the estimated state. The shaded region around the estimate shows the 3σ confidence interval.

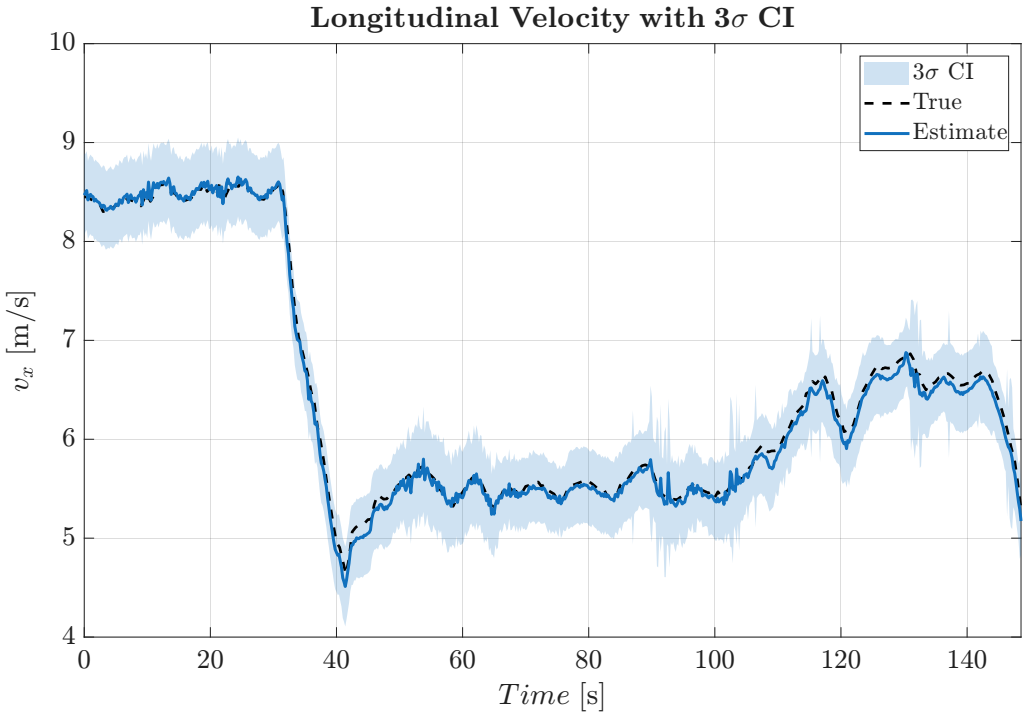

Figure 4.3: Experimental estimation results for v_x. Ground truth as the black dashed line, with the estimated state in blue. The shaded region around the estimate shows the 3σ confidence interval.

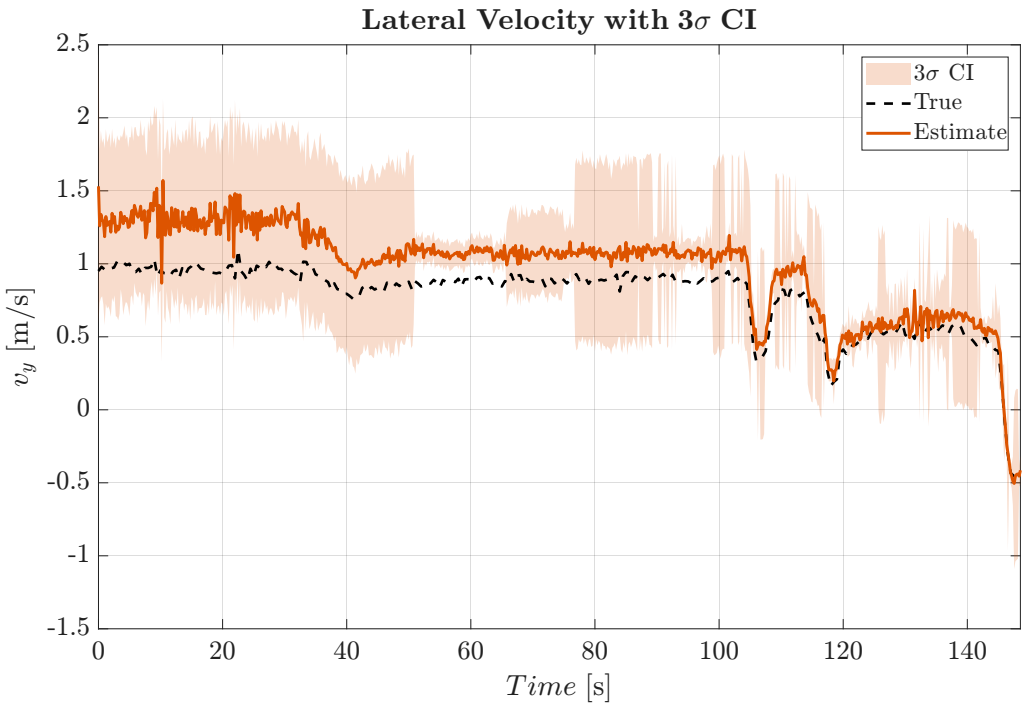

Figure 4.4: Experimental estimation results for v_y. Ground truth as the black dashed line, with the estimated state in orange. The shaded region around the estimate shows the 3σ confidence interval.

Estimation of v_x is shown in figure 4.3. The estimate follows ground truth accurately, except for minor deviations at $t = 40\,\text{s}$ and towards the end at $t > 110\,\text{s}$. Uncertainty seems to be maintained throughout. The same does not apply to the lateral velocity v_y in figure 4.4. Considering now v_y, a notable offset is present in the steady-state maneuvers between 0 s to 30 s and 40 s to 100 s. The estimate trend seems to follow that of the ground truth, despite the mean having a significant offset to the ground truth. Interestingly, it seems like the fast-paced lateral acceleration at time $> 100\,\text{s}$ reduces the mean offset almost down to zero, aligning with the ground truth mean briefly during changes of velocity.

The results for the yaw rate estimate, plotted in figure 4.5, is similar to v_y. The mean value has an offset throughout the steady-state driving between 0 s to 30 s and 40 s to 100 s, while the trend follows the ground truth. Also for this estimate does the mean offset seen during steady-state driving vanish when the vehicle undergoes fast lateral acceleration after time $> 100\,\text{s}$, similarly to figure 4.4.

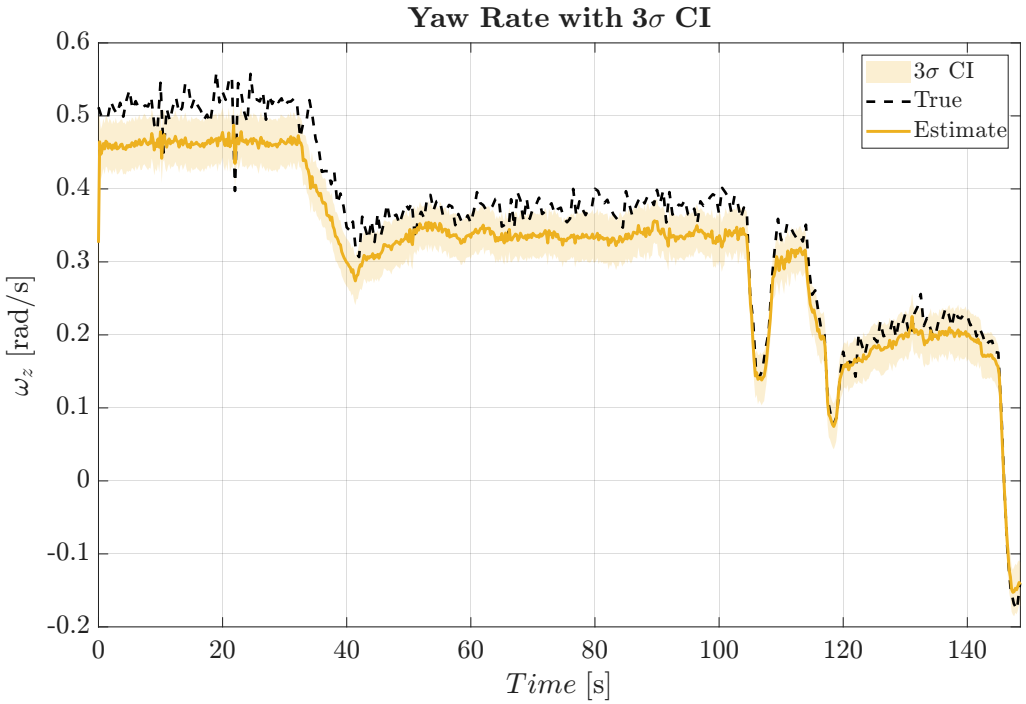

Figure 4.5: Experimental estimation results for ω_z. Ground truth as the black dashed line, with the estimated state in yellow. The shaded region around the estimate shows the 3σ confidence interval.

Figures 4.6 and 4.7 show the results for the tire cornering stiffness (TCS) parameters to be estimated. There are clear trends, both upwards and downwards, respectively. In both cases, the slope seems related to the lateral acceleration in figure 4.2, and the estimate does not converge during the logged time period. There was no ground truth data to compare to, hence why the figures do not contain any reference to compare the estimate to. Worth to keep in mind is that neither TCS parameter is normalized with the vertical force for this estimator.

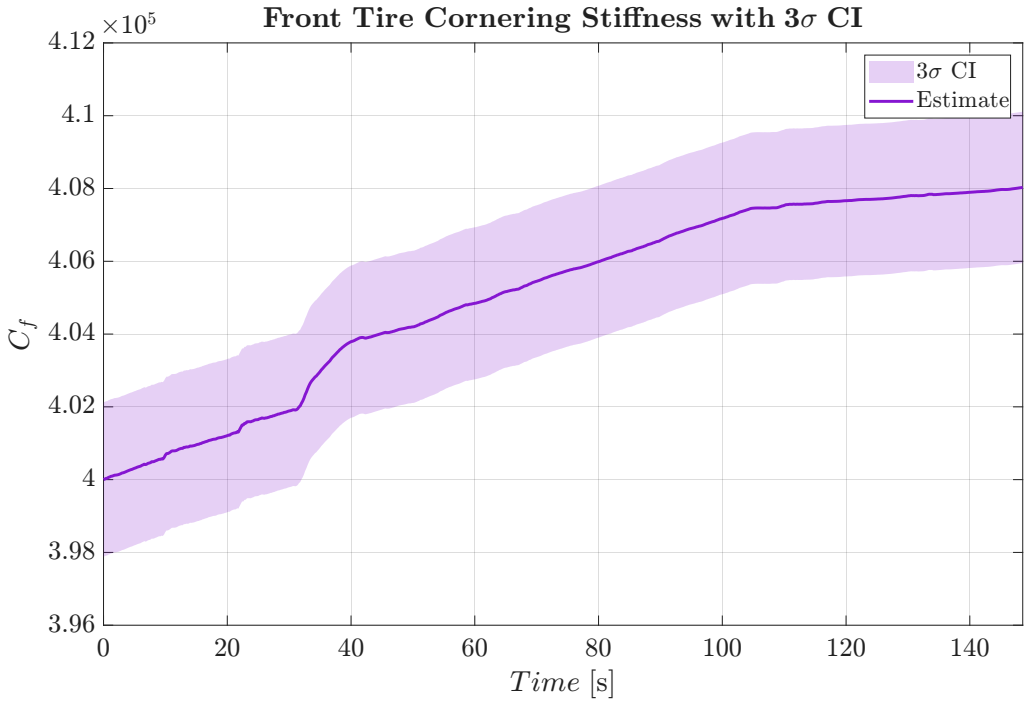

Figure 4.6: Experimental estimation results for the lumped cornering stiffness C_f. The shaded region around the estimate shows the 3σ confidence interval.

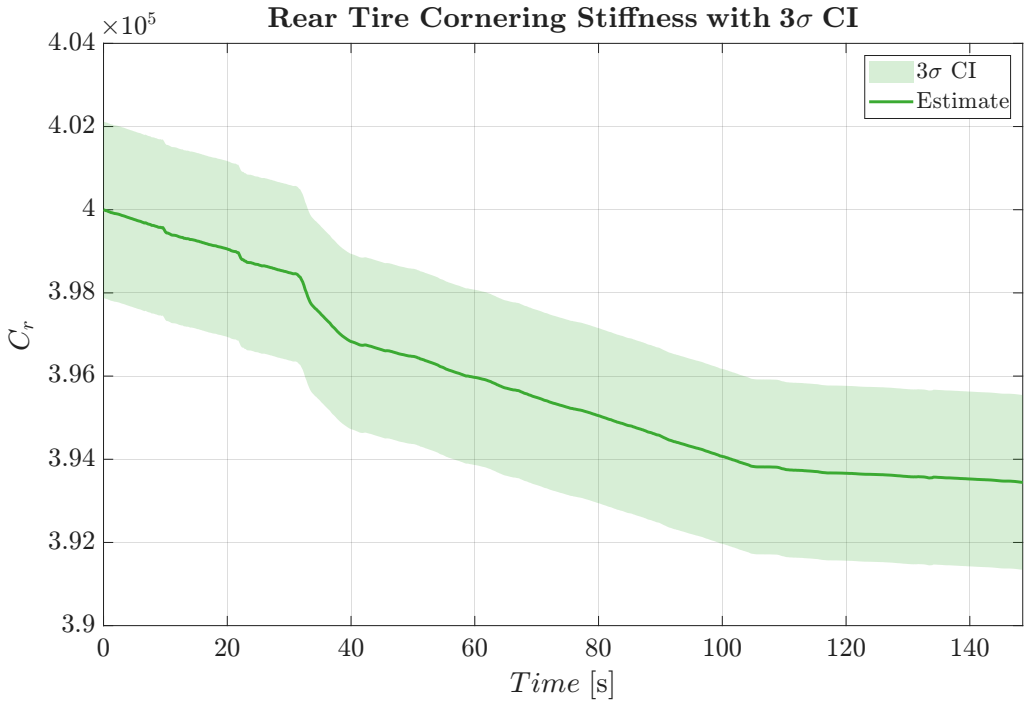

Figure 4.7: Experimental estimation results for the rear-axle lumped cornering stiffness C_r. The shaded region around the estimate shows the 3σ confidence interval.

4.2 One Track Tractor Model Results

This section presents the estimation results obtained using the single track tractor model implemented in IPG TruckMaker together with the estimator formulation described in section 3.3.4. The primary results considered the adaptive measurement vector z_k described in section 3.3.3.3. A comparison to always having velocity measurements available is also presented.

The results towards the end of this section show the truck being driven around Route 2 (circle) at varying velocities, to evaluate excitation requirements, followed by the results from testing the update strategy described in section 3.4 at the very end.

This results are obtain by having a constant process and measurement noise mentioned in table 3.10 and table 3.13.

4.2.1 Estimation with Degraded Sensing Conditions

The evaluated maneuver in the following results corresponds to the scenario 1-2-3 (Route 0) presented in section 3.2.5. Estimator performance is presented as figures and evaluated for tractor longitudinal velocity, lateral velocity, yaw rate, and lumped tire cornering stiffness parameters. To evaluate estimator robustness under degraded sensing conditions, direct velocity measurements are disabled at $t \geq 95\,\mathrm{s}$.

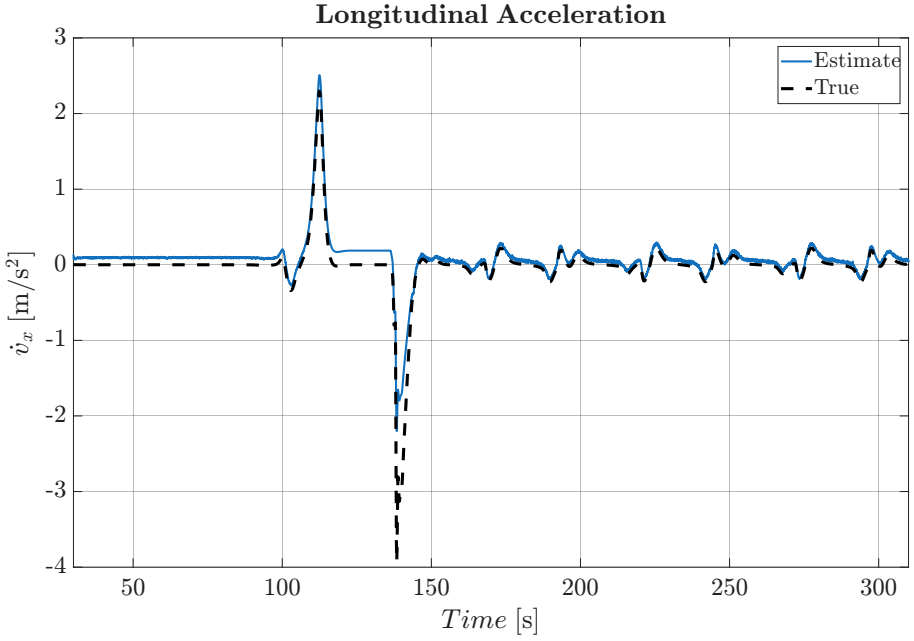

Figure 4.8: Comparison between the estimated longitudinal acceleration a_x (blue solid line) and its simulated true value (black dashed line).

Figure 4.8 illustrates the estimated longitudinal acceleration together with the true acceleration obtained directly from the simulation environment. It can be observed

that there is a varying deviation between the estimated and true signals. This deviation correlates with the different maneuvers of Route 0, which are described in Section 3.2.5.

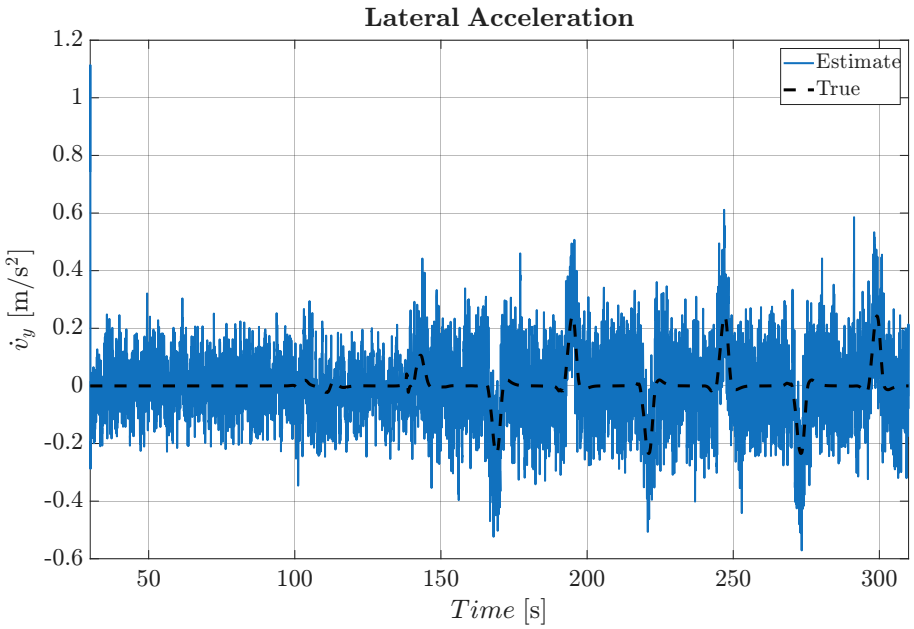

Figure 4.9: Comparison between the lateral acceleration estimate (blue solid line) and the true simulated reference (black dashed line).

Figure 4.9 illustrates the estimated lateral acceleration together with the reference signal. It can be observed that the estimate follows the reference signal well however, it exhibits higher fluctuations compared to the reference signal obtained from the simulation environment.

Figure 4.10 depicts the estimated yaw acceleration together with the reference signal. It can be observed that the estimate follows the reference signal and captures the yaw dynamics well.

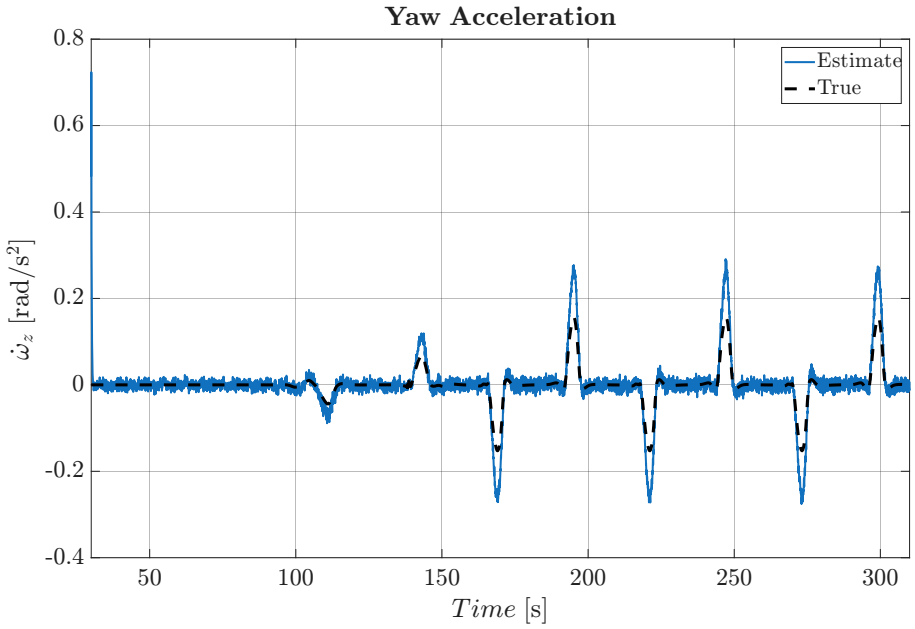

Figure 4.10: Comparison between the estimated (blue solid line) and true (black dashed line) yaw acceleration.

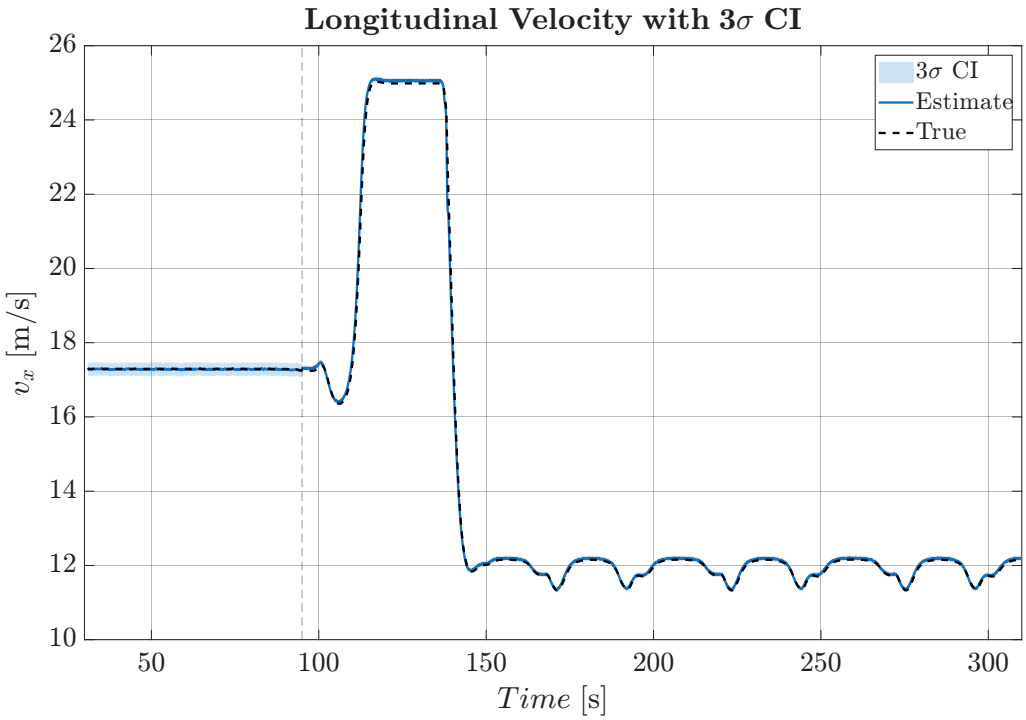

Figure 4.11: Comparison between the estimated (blue solid line), true (black dashed line), and $\pm 3\sigma$ bounds of the tractor longitudinal velocity. The vertical dashed line indicates the time at which velocity measurements become unavailable.

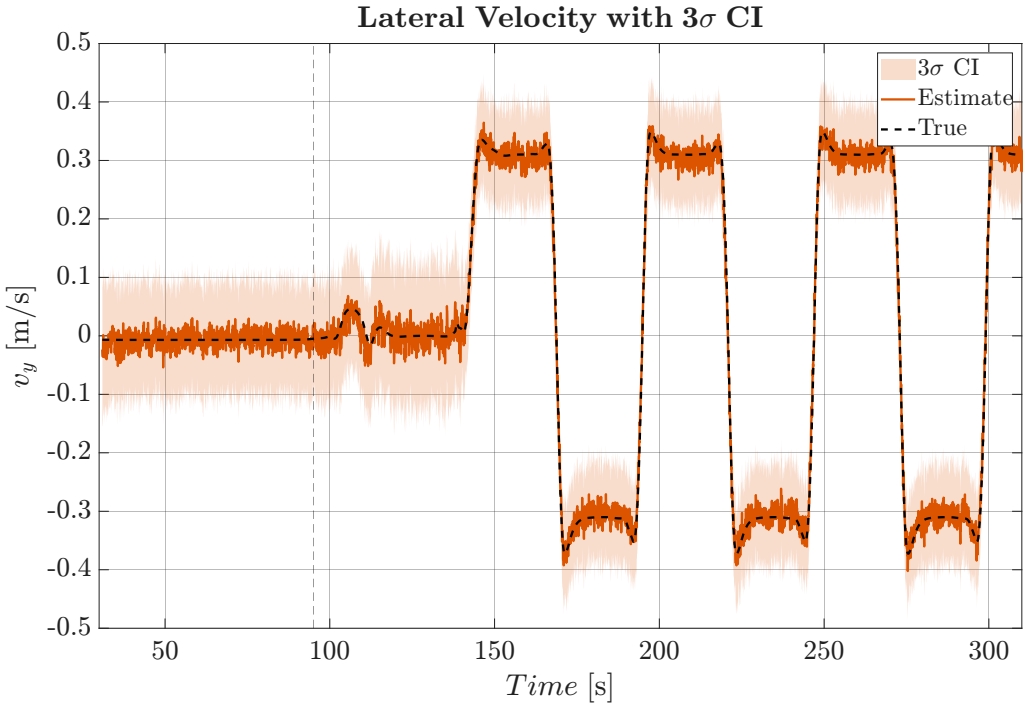

Figure 4.12: Comparison between the estimated (orange solid line), true (black dashed line), and $\pm 3\sigma$ bounds of the tractor lateral velocity. The vertical dashed line indicates the time at which velocity measurements became unavailable.

The estimated longitudinal velocity is shown in figure 4.11, together with the true velocity obtained directly from the simulation environment. It can be observed that the estimate follows the true signal very well during the entire Route 0 maneuver. It can also be observed that the uncertainty is relatively large for $t \leq 95\,\text{s}$, despite the availability of direct velocity measurements, and decreases after the velocity measurements are disabled for $t > 95\,\text{s}$.

Figure 4.12 illustrates the estimated lateral velocity together with the true signal. It can be observed that the estimate follows the true signal very well during the entirety of Route 0.

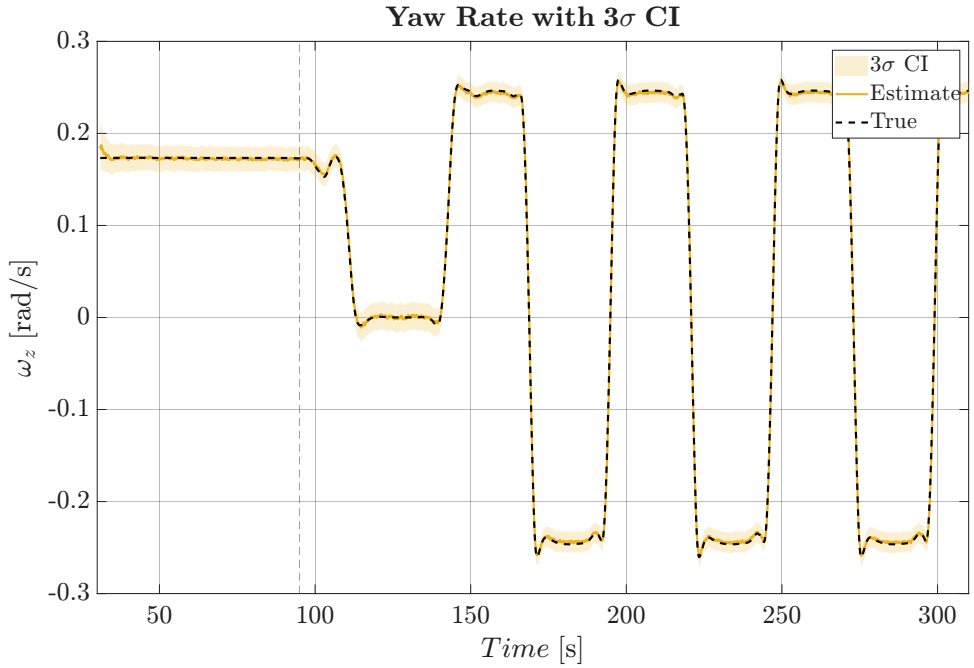

Figure 4.13: Comparison between the estimated (yellow solid line), true (black dashed line), and $\pm 3\sigma$ bounds of the tractor yaw rate.

The estimated yaw rate is shown in figure 4.13 together with the true signal. As seen in the figure, the estimate follows the true signal very well during the entire Route 0 maneuver.

Figure 4.14 illustrates the estimated front tire cornering stiffness together with the corresponding reference interval obtained from the simulation environment and the estimated 3σ confidence interval. As can be seen in the figure, the estimated front TCS remains within the reference interval and stays nearly constant throughout the maneuver, consistent with the model assumptions.

Figure 4.15 illustrates the estimated rear tire cornering stiffness together with the corresponding reference interval obtained from the simulation environment and the estimated 3σ confidence interval. As can be seen in the figure, the estimated rear TCS remains within the reference interval and stays nearly constant throughout the maneuver, consistent with the model assumptions.

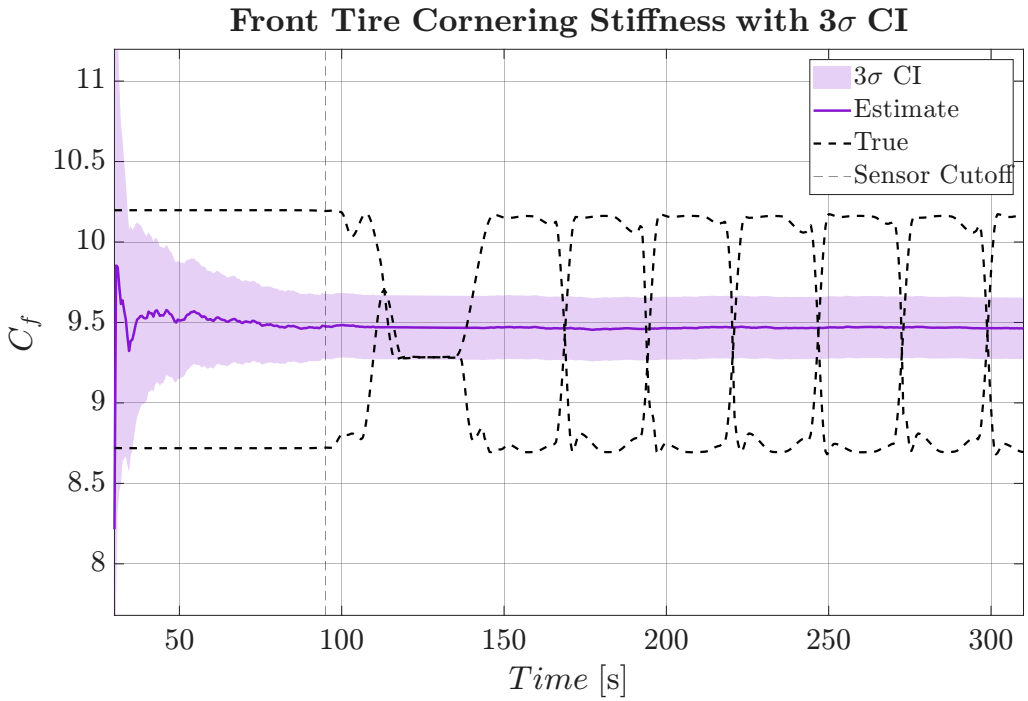

Figure 4.14: Estimated tractor front tire cornering stiffness (purple solid line) together with the corresponding reference interval (black solid lines) and $\pm 3\sigma$ confidence bounds.

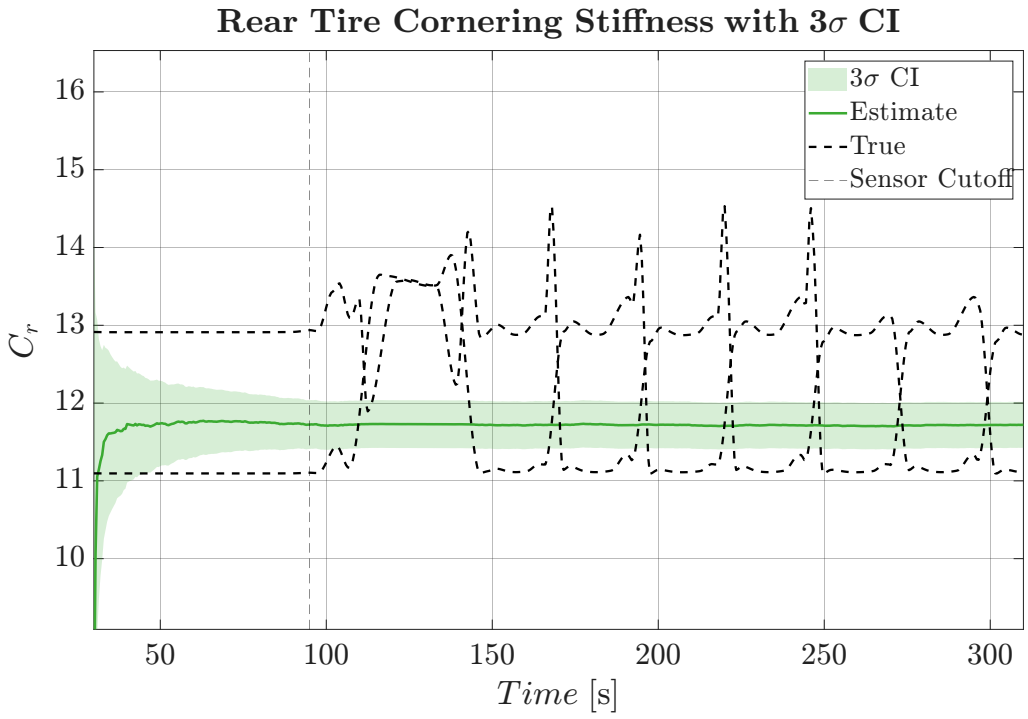

Figure 4.15: Estimated tractor rear tire cornering stiffness (green solid line) together with the corresponding reference interval (black solid lines) and 3σ confidence bounds.

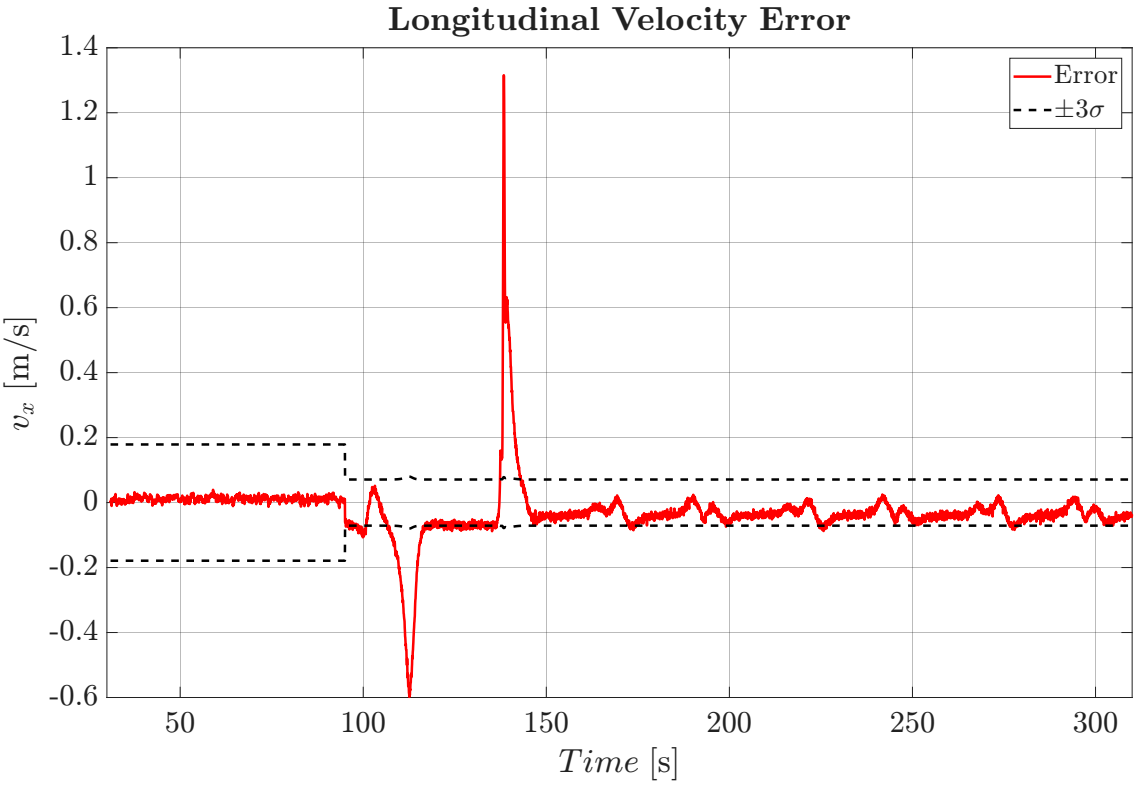

Figure 4.16: Tractor longitudinal velocity estimation error (red solid line) with $\pm 3\sigma$ confidence bounds (black dashed lines).

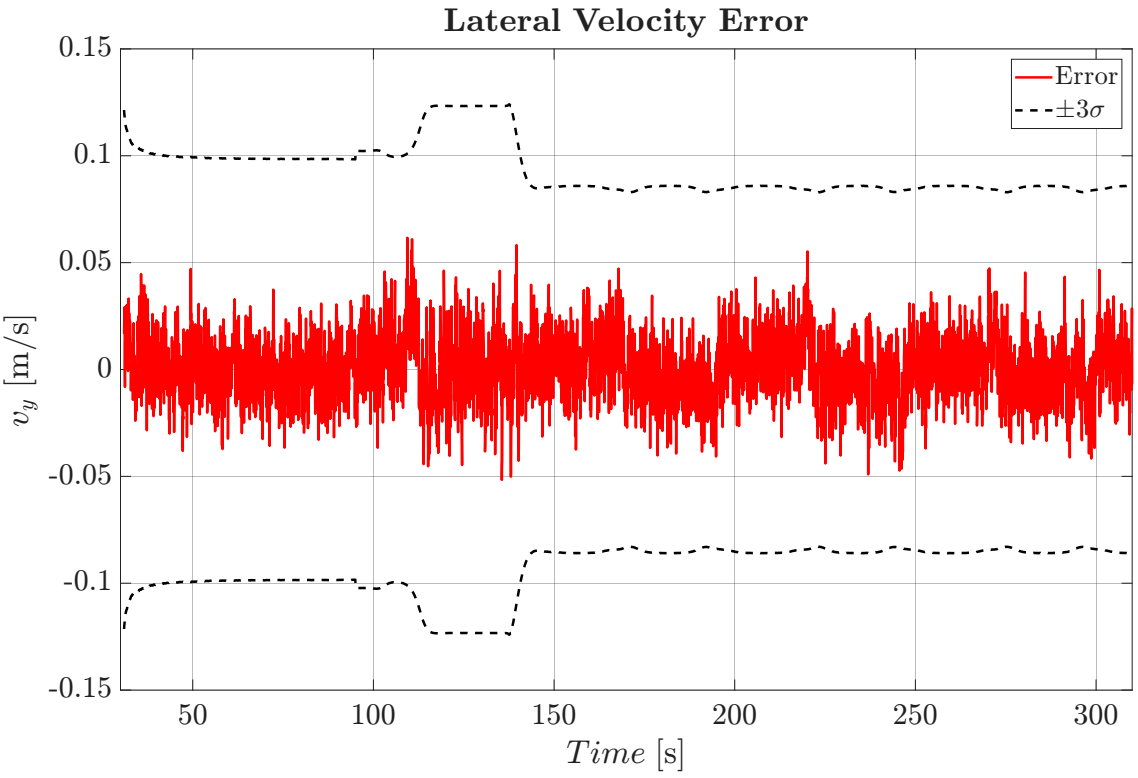

Figure 4.17: Tractor lateral velocity estimation error (red solid line) with $\pm 3\sigma$ bounds (black dash lines).

Figure 4.16 illustrates the error between the estimated and true longitudinal velocity together with the $\pm 3\sigma$ confidence interval. It can be observed that the estimation error remains close to zero and stays within the $\pm 3\sigma$ bounds for most of the maneuver, except for a few transient peaks.

Figure 4.17 illustrates the error between the estimated and true lateral velocity together with the $\pm 3\sigma$ confidence interval. It can be observed that the estimation error remains close to zero and stays within the $\pm 3\sigma$ bounds for the entire maneuver.

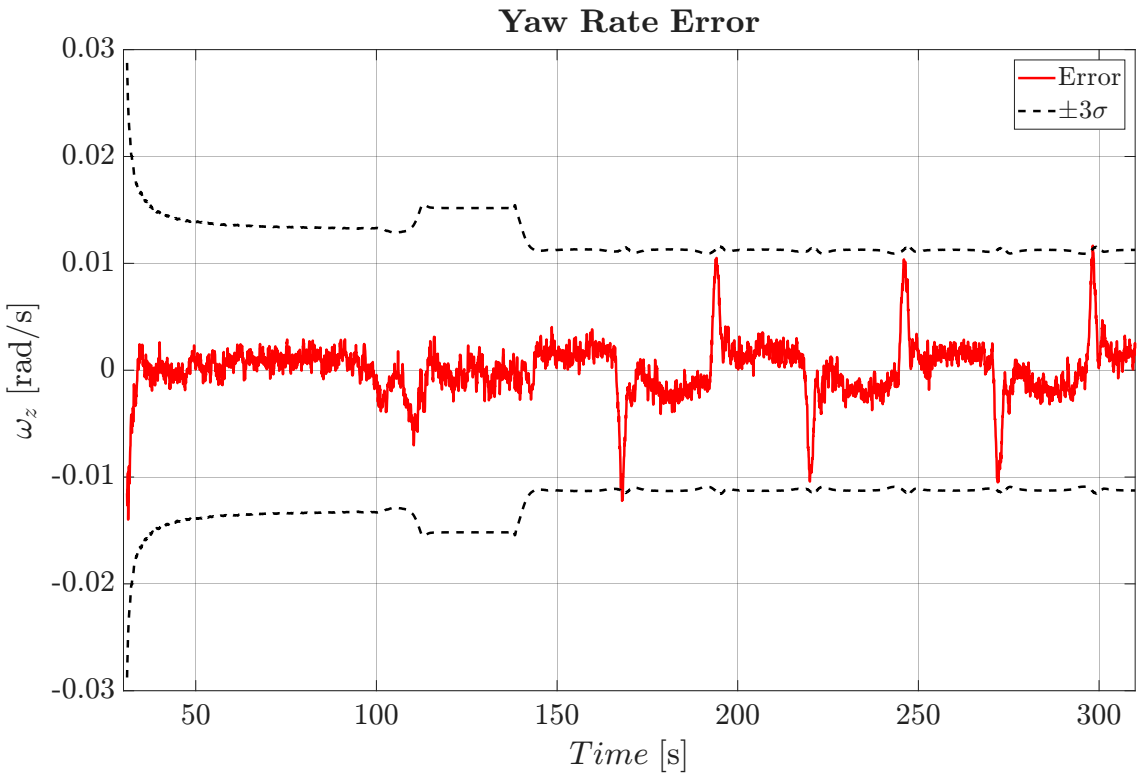

Figure 4.18: Tractor yaw rate estimation error (red solid line) with $\pm 3\sigma$ bounds (black dash line).

Figure 4.18 illustrates the error between the estimated and true yaw rate together with the $\pm 3\sigma$ confidence interval. It can be observed that the estimation error remains close to zero and stays within the $\pm 3\sigma$ bounds for the entire maneuver.

Figure 4.19 illustrates the NEES consistency test for the estimated vehicle states. It can be observed that the NEES remains within the theoretical confidence bounds for most of the maneuver, indicating that the estimator covariance is reasonably consistent with the observed estimation errors.

Figure 4.20 illustrates the empirical NEES distribution together with the corresponding theoretical chi-square (χ^2) distribution. Although deviations can be observed, the overall distribution follows the theoretical trend reasonably well, indicating acceptable estimator consistency.

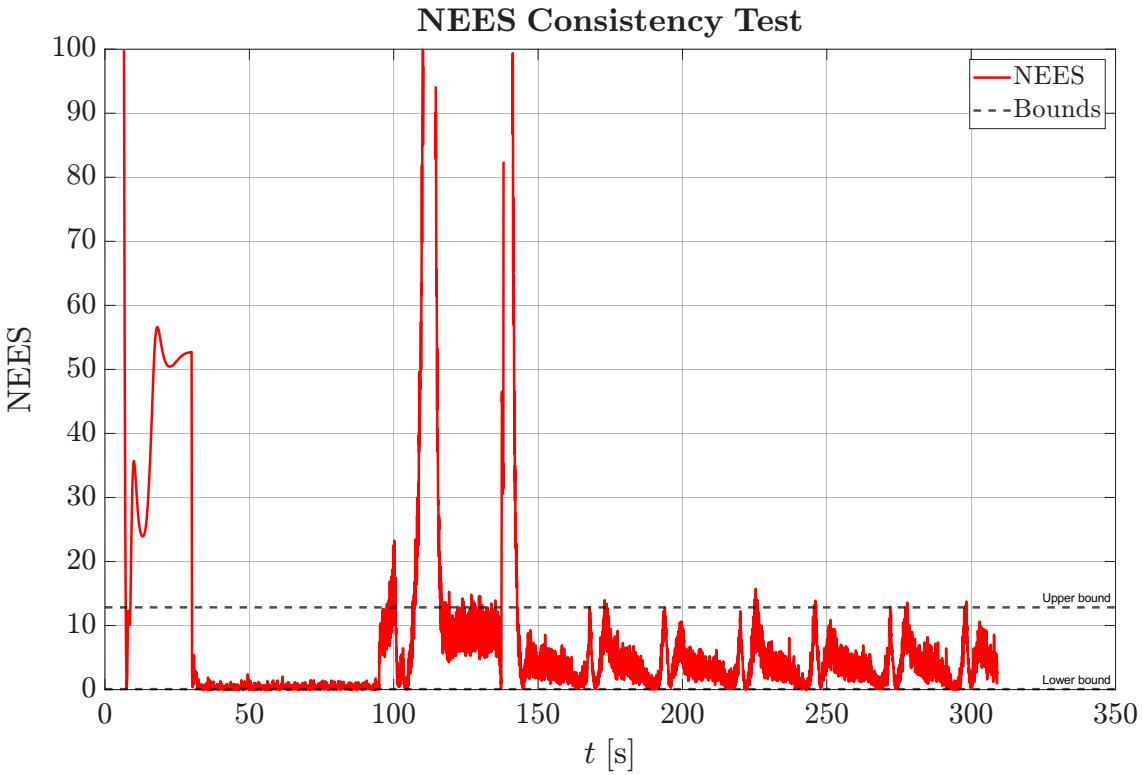

Figure 4.19: Normalized Estimation Error Squared (NEES) consistency test for the estimated vehicle states together with the corresponding confidence bounds.

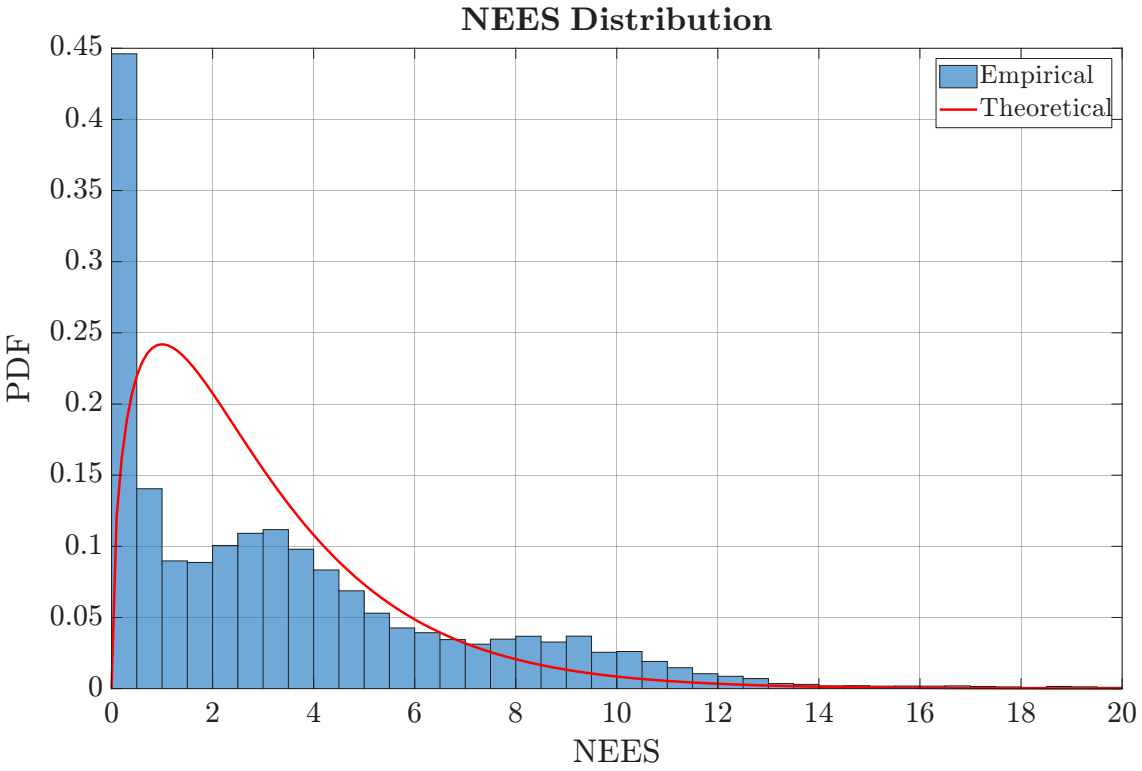

Figure 4.20: Empirical NEES distribution compared with the theoretical chi-square distribution for the considered state dimension.

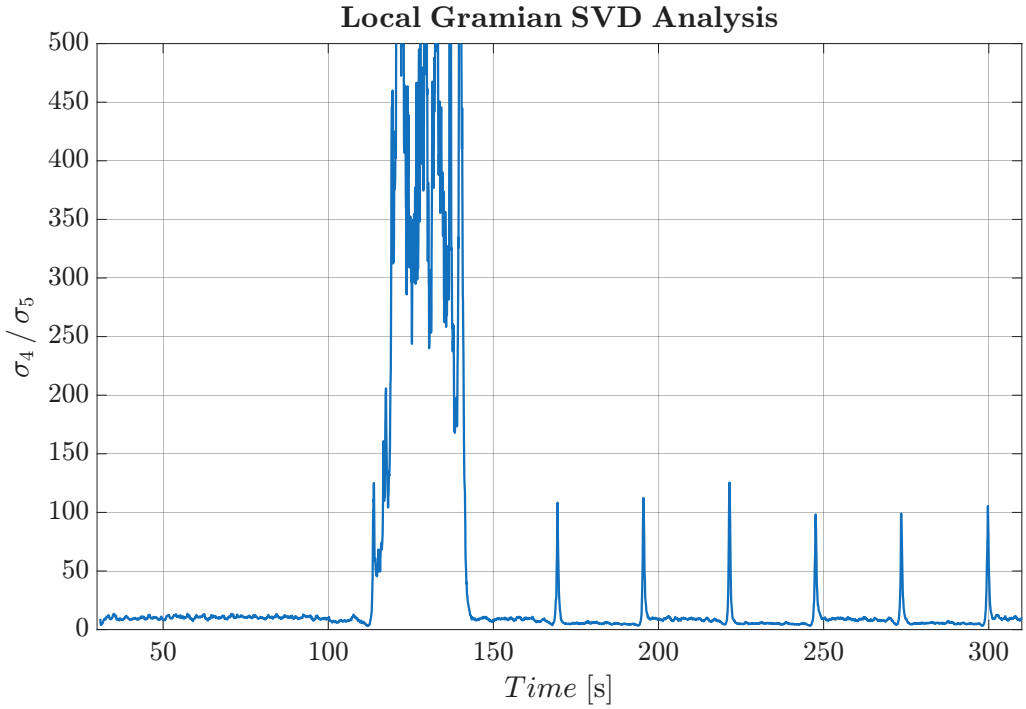

Figure 4.21: Local observability Gramian singular value analysis. Lower is better.

The observability metric from (2.59) is shown in figure 4.21. The metric seems to be a good indicator of lateral dynamics, maintaining low values during maneuvers with significant lateral dynamics while increasing by more than a magnitude during the 700 m straight at time 110 s to 140 s.

4.2.2 Estimate Comparison Between Sensing Conditions

Method section 3.3.3.3 describes two measurement vectors z_k. This section presents a comparison of running the estimator in section 3.3.4 with vs. without degraded sensing condition. The scenario was the same as in section 4.2.1, where the degraded sensing condition was used.

Figure 4.22 shows a comparison of longitudinal velocity estimate errors. Having velocity measurements available does seem to decrease the error during straight driving, compared to the degraded sensing condition. Worth noting is also that the uncertainty bounds are unchanged when there is no sensor cutoff.

The errors for the lateral dynamics stay virtually the same, as can be seen in figures 4.23 and 4.24. There is a slight difference in uncertainty for the lateral velocity v_y, but the yaw rate error difference is negligible. Comparing the estimates, there were no significant differences to the results shown in section 4.2.1, so for brevity, the estimation results for always-available velocity measurements have been omitted.

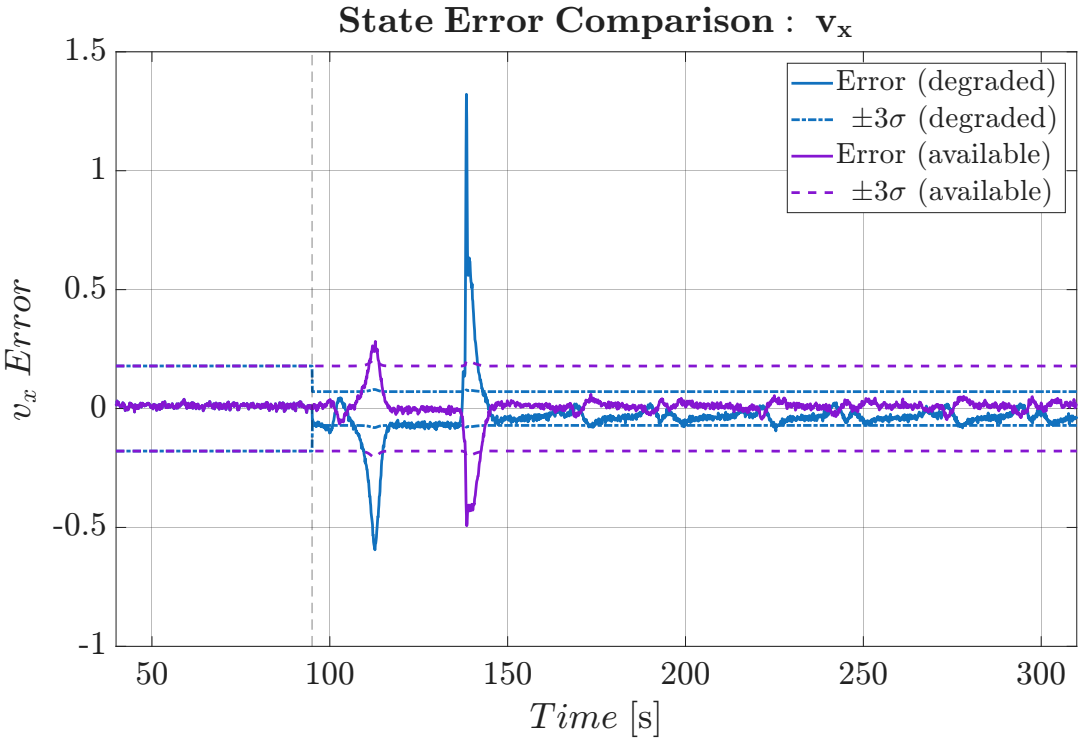

Figure 4.22: Tractor longitudinal velocity estimation error (solid lines) with $\pm 3\sigma$ confidence bounds (dashed or dash-dotted lines). The vertical dashed line shows the cutoff time 95 s for the degraded sensing condition.

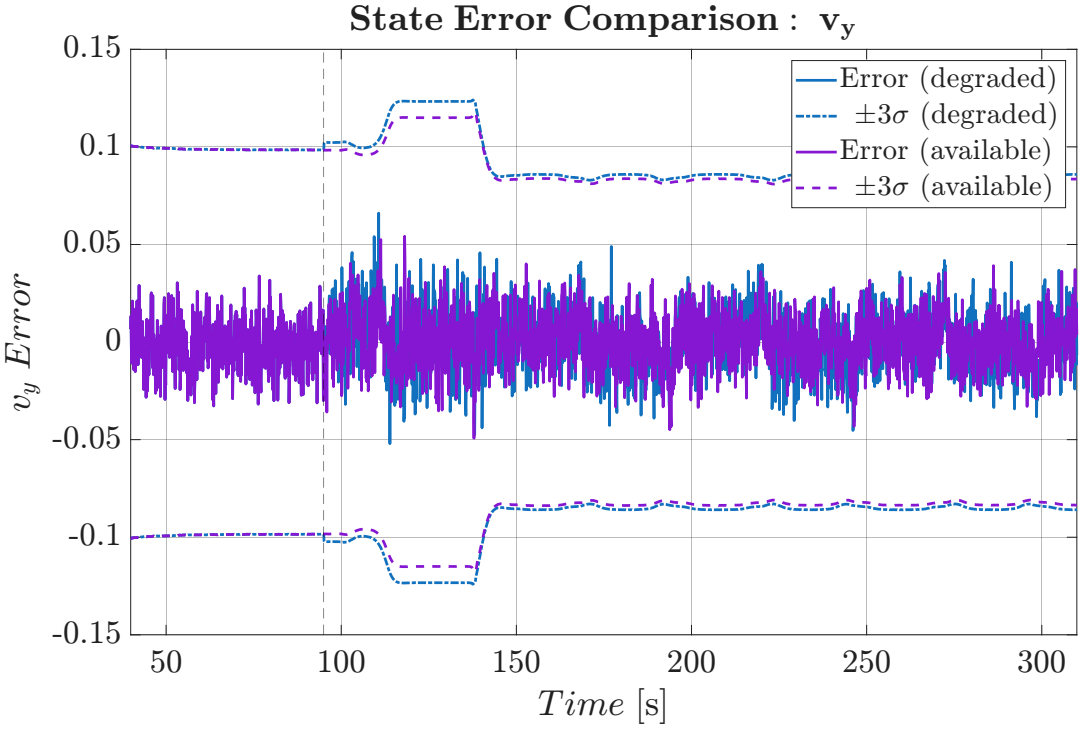

Figure 4.23: Tractor lateral velocity estimation error (solid lines) with $\pm 3\sigma$ confidence bounds (dashed or dash-dotted lines). The vertical dashed line shows the cutoff time 95 s for the degraded sensing condition.

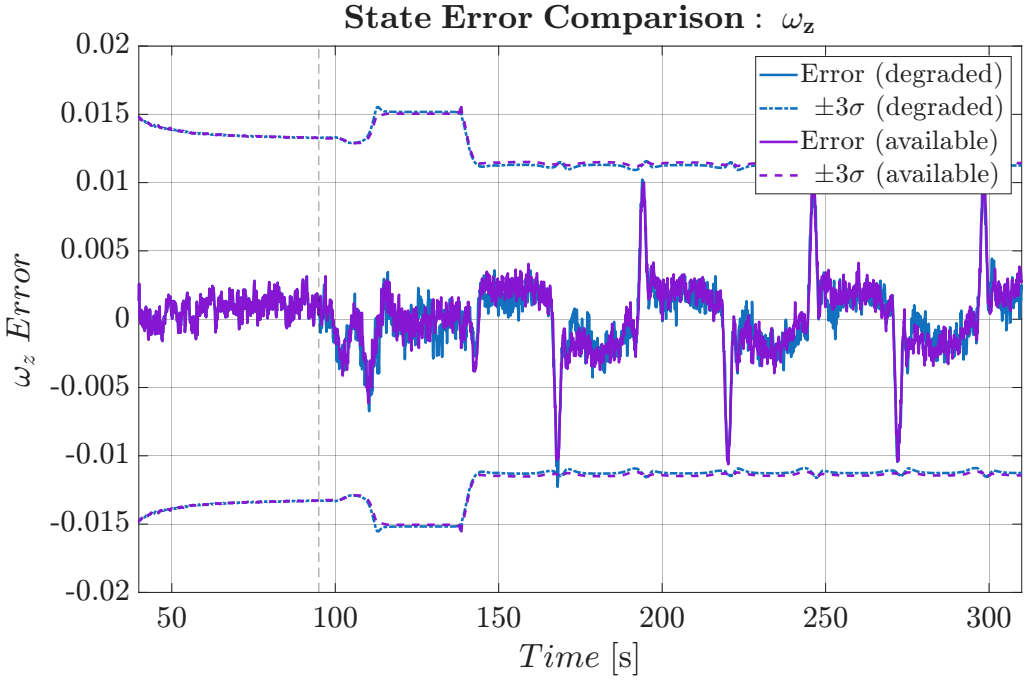

Figure 4.24: Tractor yaw rate estimation error (solid lines) with $\pm 3\sigma$ confidence bounds (dashed or dash-dotted lines). The vertical dashed line shows the cutoff time 95 s for the degraded sensing condition.

4.2.3 Varying Lateral Dynamics

This section presents results from the truck-only estimator described in section 3.3, obtained by driving the truck at varying maximum velocities in the steady-state circle Route 2 from section 3.2.5. The setup for this section did not use the adaptive measurement vector z_k; for these results velocity was always available. The figures show the estimated TCS parameters using the same visual convention as in figures 4.14 and 4.15. There is also a corresponding plot of the observability metric (2.59) to be able to compare estimate accuracy to observability.

4.2.3.1 Steady-State Circle with Fixed Speed Limit

Below are figures showing C_f and C_r estimation results from fixed steady state maneuvers, driving Route 2 at fixed speeds. The figures are scaled down in size to fit side-by-side for brevity at the expense of text readability, to more easily allow for comparison of the front and rear convergence trends.

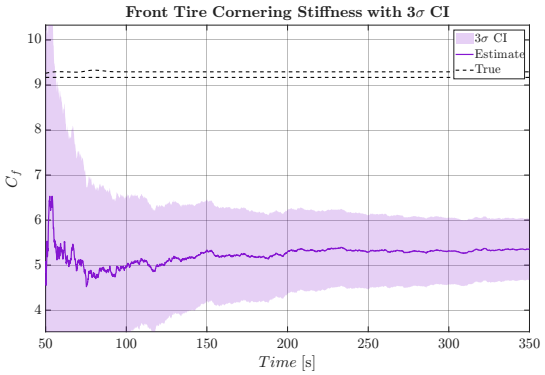

(a) Estimated tractor **front** TCS in purple and corresponding reference interval in black. The shaded region is the $\pm 3\sigma$ confidence interval.

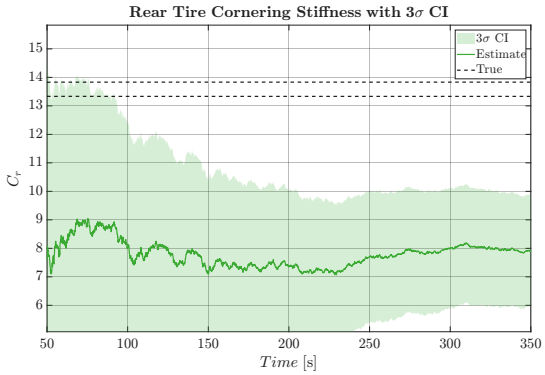

(b) Estimated tractor **rear** TCS in green and corresponding reference interval in black. The shaded region is the $\pm 3\sigma$ confidence interval.

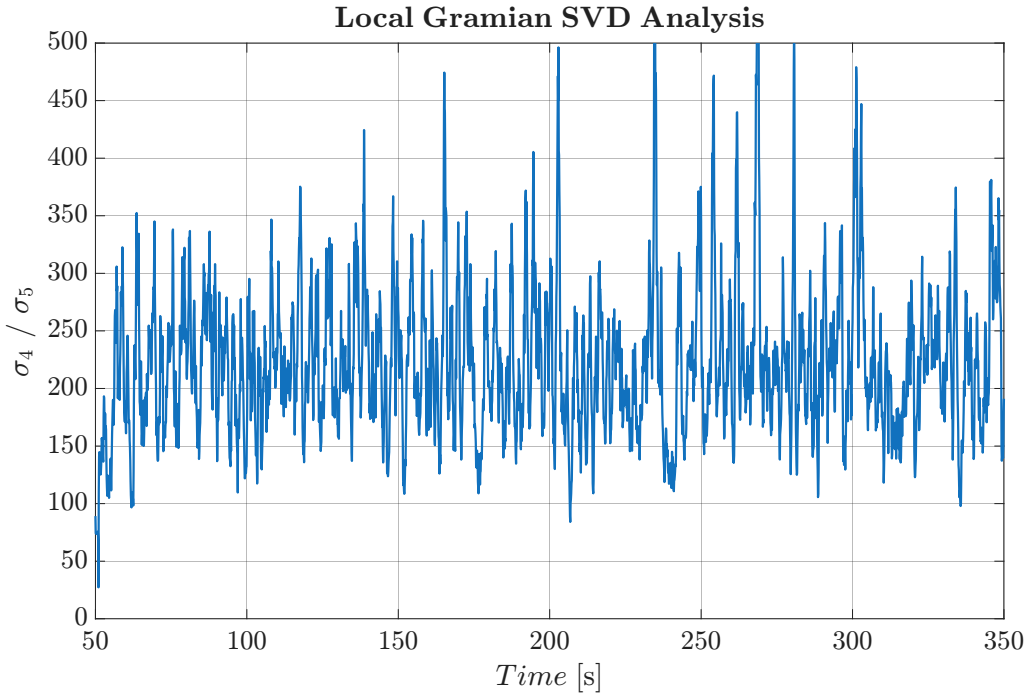

(c) Observability metric computed using (2.59). Lower values are better.

Figure 4.25: Cornering stiffness parameter estimates and the observability metric for a single truck driving a steady-state circle at $v_x = 20\,\mathrm{km/h}$.

Neither parameter in figure 4.25 shows signs of convergence, with the rear C_r being the most uncertain estimate of the two. They are both confidently outside the reference interval. The observability metric is fluctuating around a mean of ~ 225.

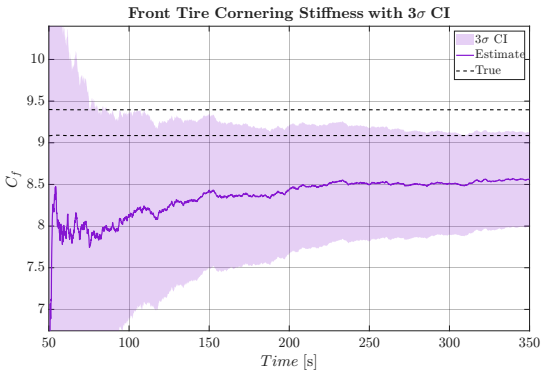

(a) Estimated tractor **front** TCS in purple and corresponding reference interval in black. The shaded region is the $\pm 3\sigma$ confidence interval.

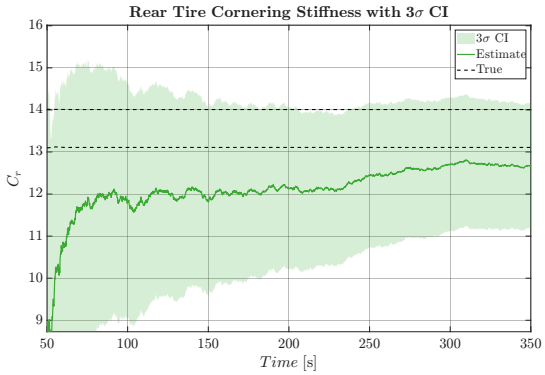

(b) Estimated tractor **rear** TCS in green and corresponding reference interval in black. The shaded region is the $\pm 3\sigma$ confidence interval.

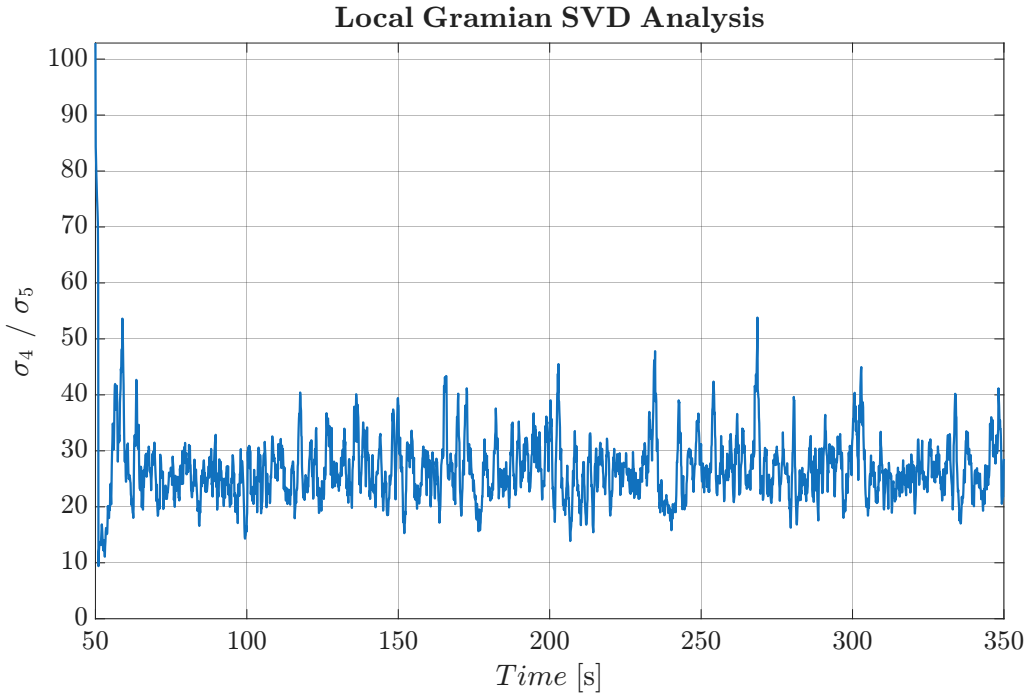

(c) Observability metric computed using (2.59). Lower values are better.

Figure 4.26: Cornering stiffness parameter estimates and the observability metric for a single truck driving a steady-state circle at $v_x = 30\,\mathrm{km/h}$.

The uncertainty intervals of both figures 4.26a and 4.26b overlap with at least one reference value most of the time. The estimates seem to begin converging towards a stable value after $\sim 250\,\mathrm{s}$. The observability metric in figure 4.26c is fluctuating around a mean of ~ 30.

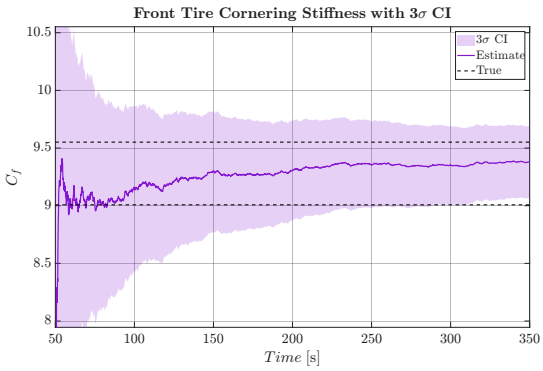

(a) Estimated tractor **front** TCS in purple and corresponding reference interval in black. The shaded region is the $\pm 3\sigma$ confidence interval.

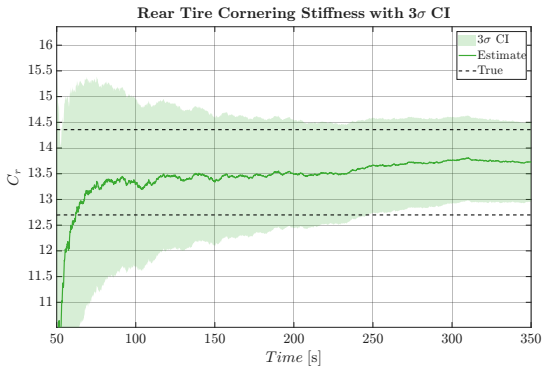

(b) Estimated tractor **rear** TCS in green and corresponding reference interval in black. The shaded region is the $\pm 3\sigma$ confidence interval.

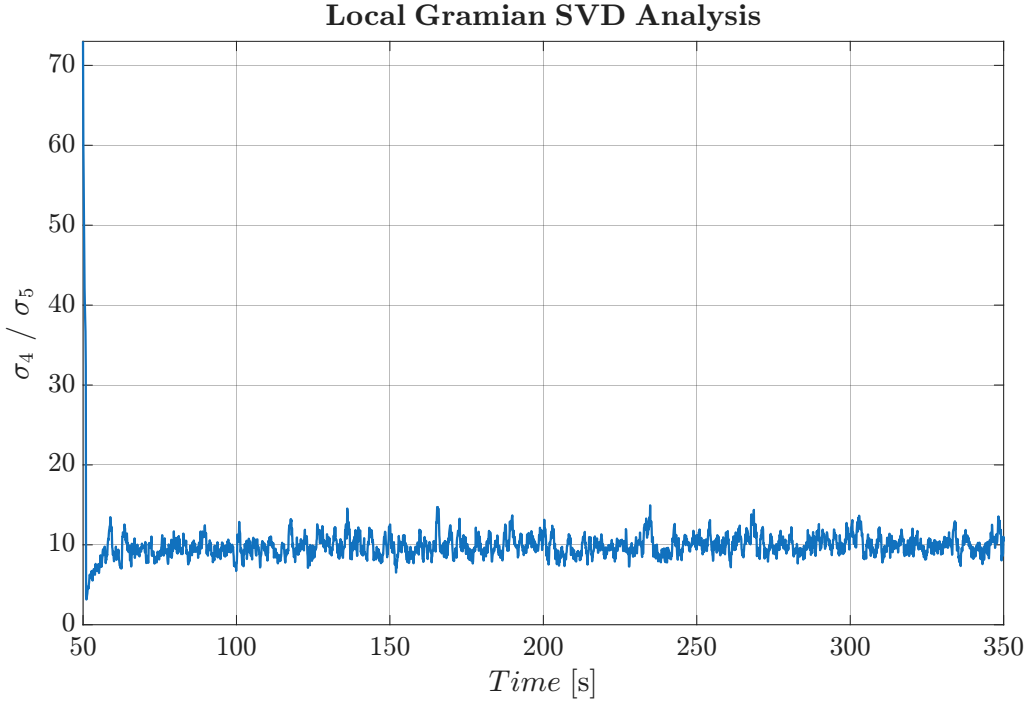

(c) Observability metric computed using (2.59). Lower values are better.

Figure 4.27: Cornering stiffness parameter estimates and the observability metric for a single truck driving a steady-state circle at $v_x = 40\,\mathrm{km/h}$.

Both estimates in figure 4.27 converge to within the reference interval, but they do so quite slowly. Uncertainty decreases slowly compared to higher speeds. The observability metric in figure 4.27c is hovering around 10.

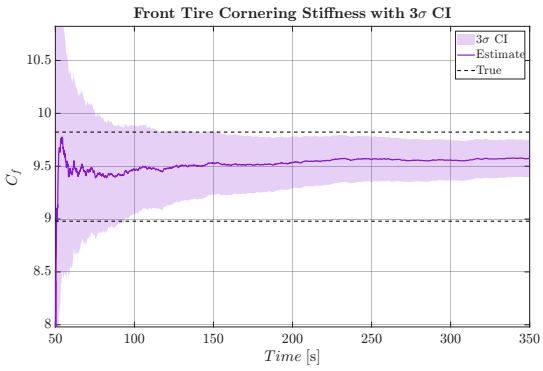

(a) Estimated tractor **front** TCS in purple and corresponding reference interval in black. The shaded region is the $\pm 3\sigma$ confidence interval.

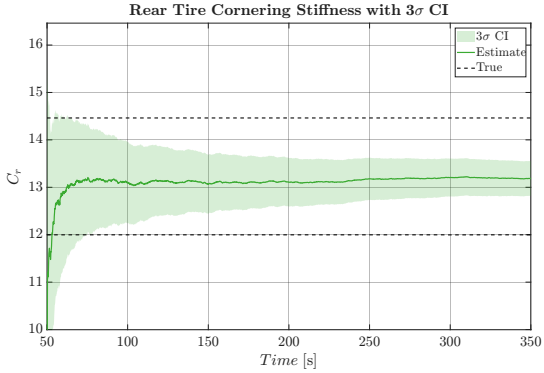

(b) Estimated tractor **rear** TCS in green and corresponding reference interval in black. The shaded region is the $\pm 3\sigma$ confidence interval.

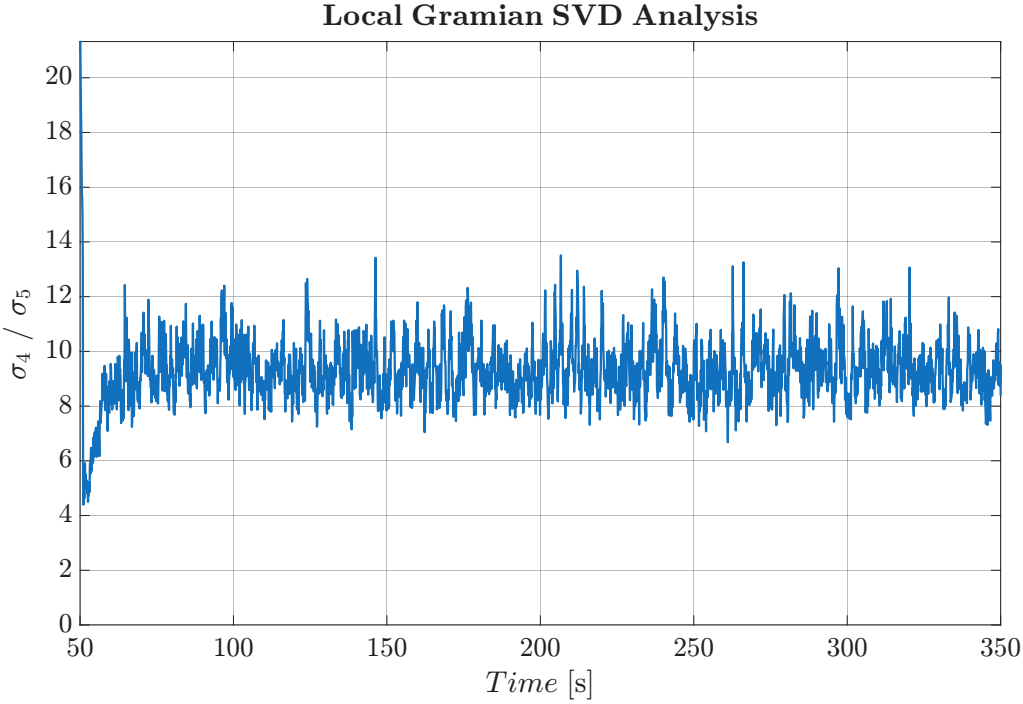

(c) Observability metric computed using (2.59). Lower values are better.

Figure 4.28: Cornering stiffness parameter estimates and the observability metric for a single truck driving a steady-state circle at $v_x = 50\,\mathrm{km/h}$.

Convergence is clear in figure 4.28, with C_f stabilizing towards the upper bound of the reference interval. The observability metric hovers around 10, similarly to when $v_x = 40\,\mathrm{km/h}$.

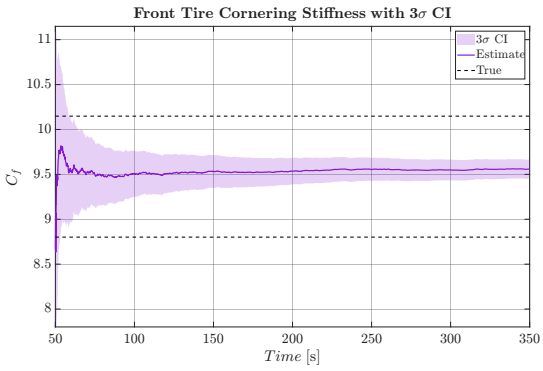

(a) Estimated tractor **front** TCS in purple and corresponding reference interval in black. The shaded region is the $\pm 3\sigma$ confidence interval.

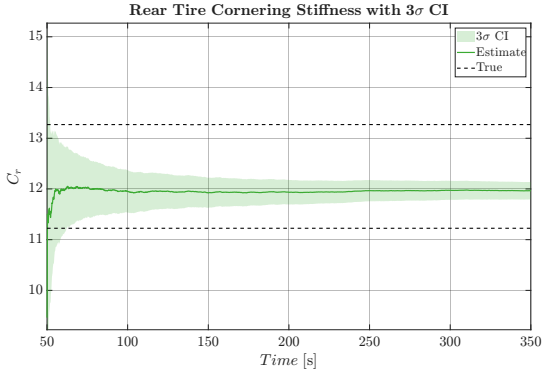

(b) Estimated tractor **rear** TCS in green and corresponding reference interval in black. The shaded region is the $\pm 3\sigma$ confidence interval.

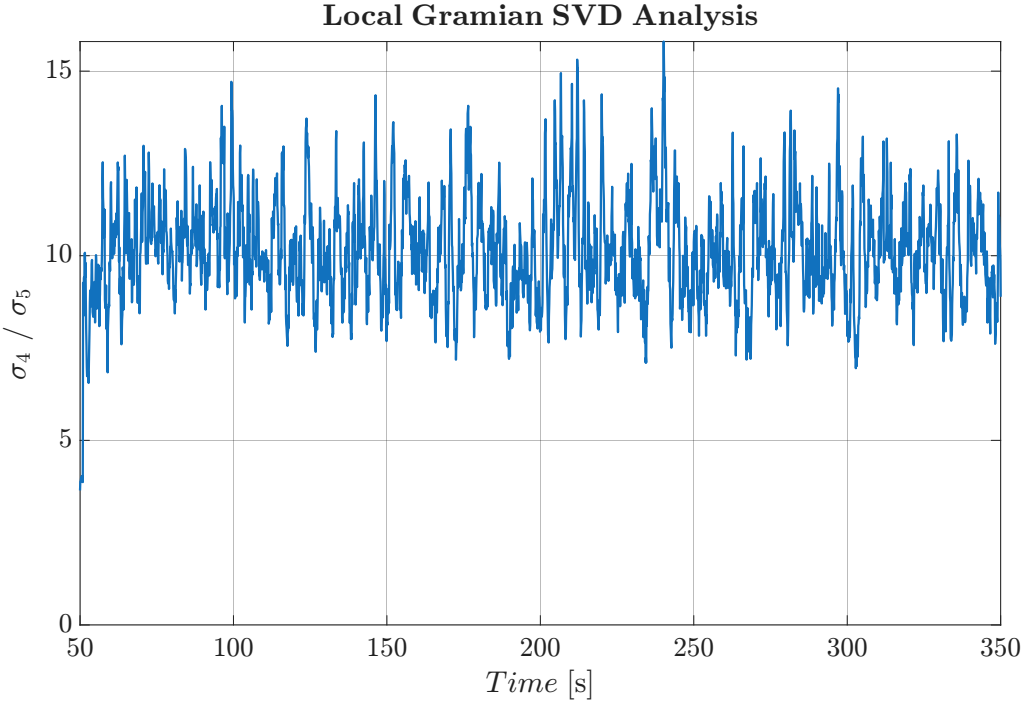

(c) Observability metric computed using (2.59). Lower values are better.

Figure 4.29: Cornering stiffness parameter estimates and the observability metric for a single truck driving a steady-state circle at $v_x = 60\,\mathrm{km/h}$.

The fixed velocity of $v_x = 60\,\mathrm{km/h}$ was close to the limiting speed the truck could drive at around Route 2 without rollover. The estimates for this speed, presented in figure 4.29, show a clear converging trend with high certainty established within the simulated time frame. The corresponding observability metric fluctuates around 10, but notably with a higher amplitude than for $v_x = 50\,\mathrm{km/h}$.

4.2.3.2 Variable Speed Limits

This section shows the estimated stiffness parameters from driving the truck around Route 2 from section 3.2.5 while changing the maximum speed at multiples of 100 s, varying the speed in both ascending and descending order. Related observability metric plots are presented at the end of this section.

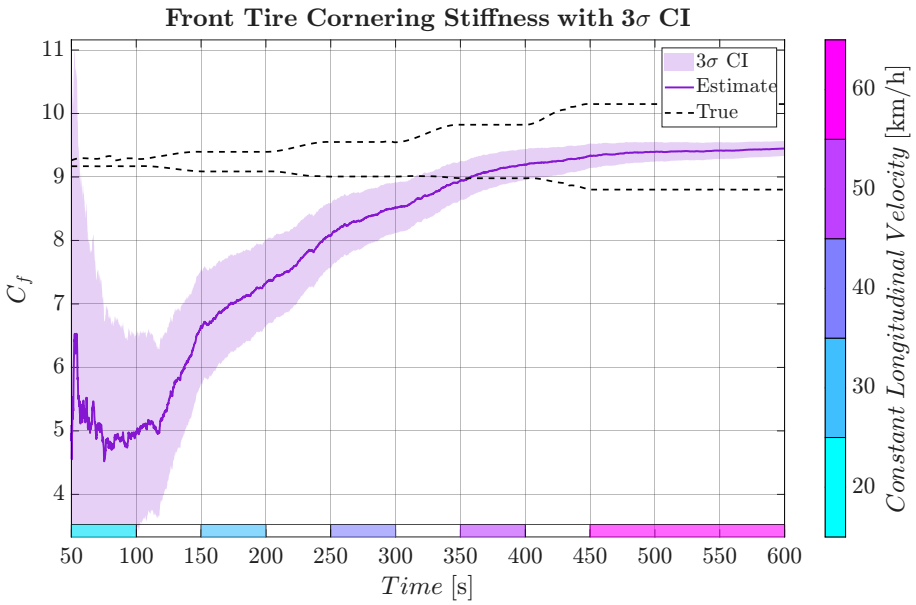

Figure 4.30: Estimated tractor **front** TCS in purple and corresponding reference interval in black. The shaded region is the $\pm 3\sigma$ confidence interval. Time intervals of constant speed are indicated by the color patches.

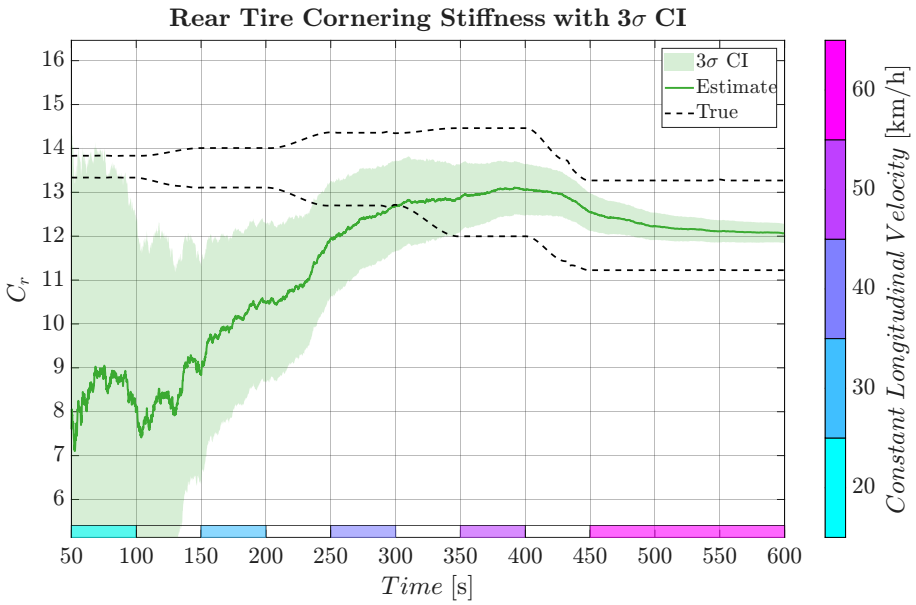

Figure 4.31: Estimated tractor **rear** TCS in green and corresponding reference interval in black. The shaded region is the $\pm 3\sigma$ confidence interval. Time intervals of constant speed are indicated by the color patches.

For the case of varying the speed limit in ascending order, shown in figures 4.30 and 4.31, both estimates seem to follow a random walk, maintaining large uncertainties. At in the transition $v_x \to 30\,\mathrm{km\,h^{-1}}$, both estimates begin trending up towards the reference interval. The rear stiffness C_r does so with more fluctuations when compared to C_f. Worth noting is the time 130 s in figure 4.30 and the time 150 s in figure 4.31, at which the last significant trend downwards occurs for each estimate. From figure 4.31, it seems like the estimator is able to adapt to the change in reference interval that occurred when going from $50\,\mathrm{km\,h^{-1}}$ to $60\,\mathrm{km\,h^{-1}}$. It is difficult to tell whether this is the case for C_f as well when increasing the velocity, since the estimate in figure 4.30 didn't converge in time for the last speed increment.

The observability metric in figure 4.32 fluctuates a lot in the beginning, despite having a moving-average low-pass filter applied to it. There is a clear improvement just in the first transition $20\,\mathrm{km\,h^{-1}} \to 30\,\mathrm{km\,h^{-1}}$, dropping from a peak of ~ 200 to ~ 30. Interestingly, there seems to be a sweet-spot for the chosen observability metric at $v_x = 50\,\mathrm{km\,h^{-1}}$, judging from the increased noise level and slightly higher mean towards the end of the simulation at max speed.

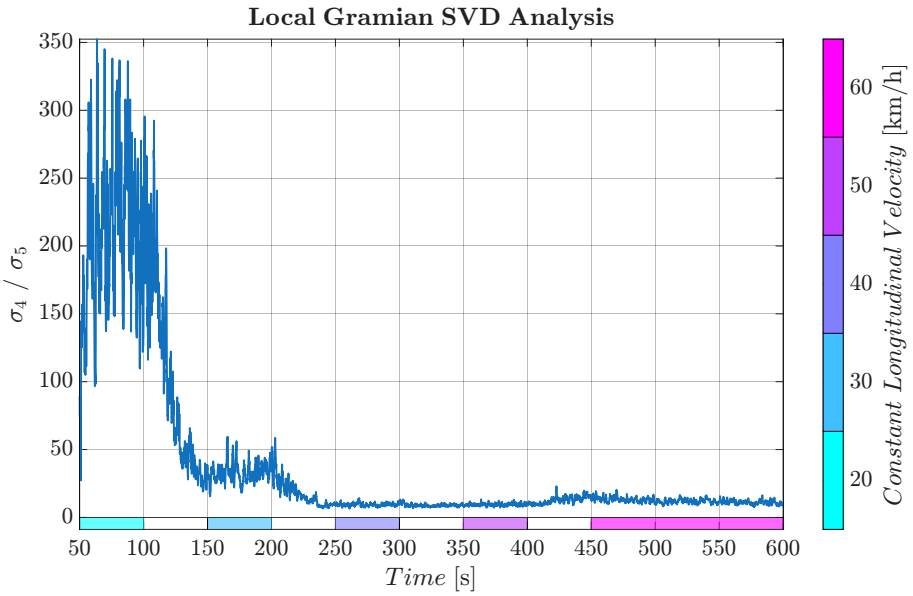

Figure 4.32: Observability metric computed using (2.59). Lower values are better.

Figures 4.33 and 4.34 show the results from varying the speed in descending order. Both estimates stabilize in the initial steady-state for time < 50 s. After the first speed transition to $50\,\mathrm{km\,h^{-1}}$, it seems like C_f has difficulty staying bounded by the reference interval, eventually not even having overlapping reference and estimate confidence interval. The result in figure 4.34 shows that the estimate begins adapting to the new reference interval after the first speed transition, but has difficulty doing so fast enough before the second speed transition. It seems like both C_f and C_r stop evolving when there is insufficient information about the lateral dynamics, judging by figures 4.33 and 4.34. They also seem to begin trending slightly downwards towards the end of the simulation. If that is a continuing trend is difficult to tell without simulating the maneuver for a significantly longer duration.

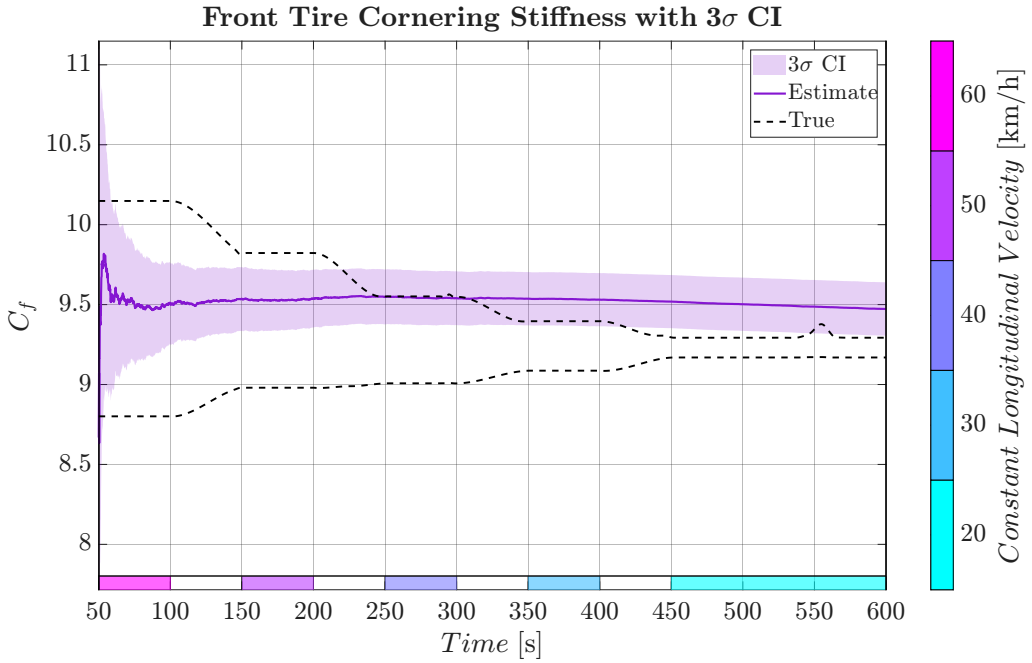

Figure 4.33: Estimated tractor **front** TCS in purple and corresponding reference interval in black. The shaded region is the $\pm 3\sigma$ confidence interval. Time intervals of constant speed are indicated by the color patches.

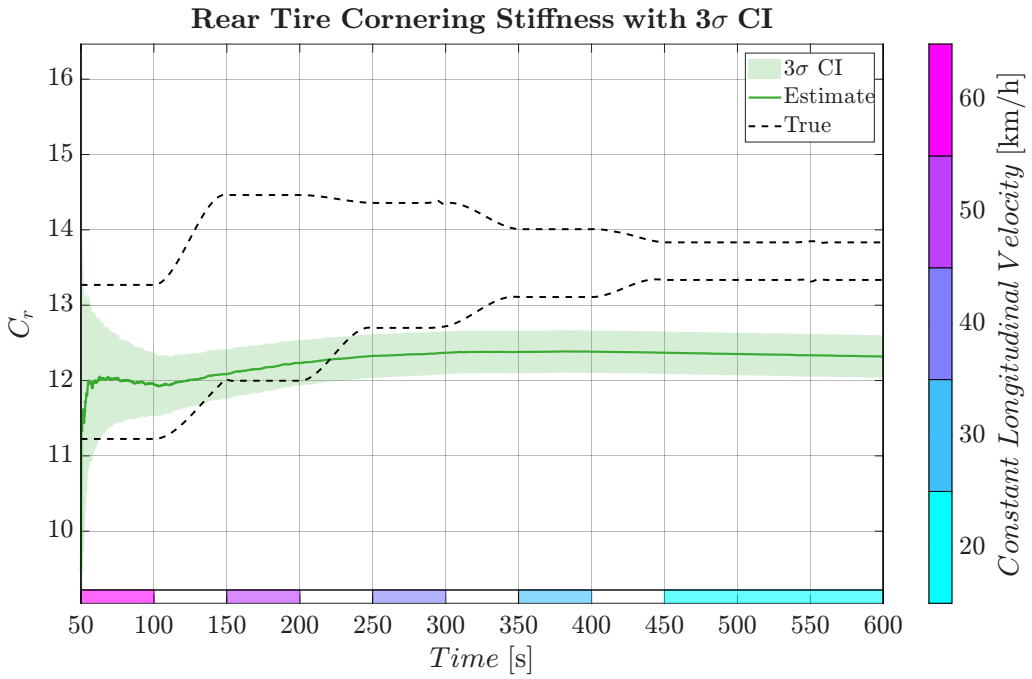

Figure 4.34: Estimated tractor **rear** TCS in green and corresponding reference interval in black. The shaded region is the $\pm 3\sigma$ confidence interval. Time intervals of constant speed are indicated by the color patches.

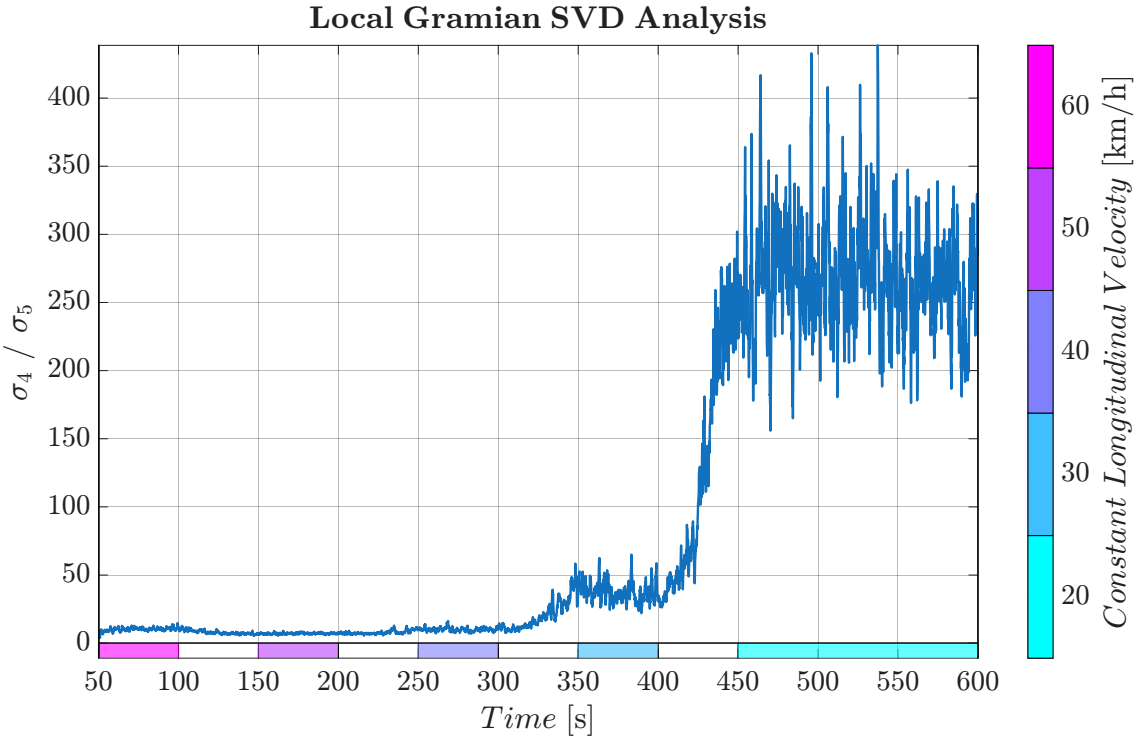

Figure 4.35: Observability metric computed using (2.59). Lower values are better.

The observability metric in figure 4.35 shows a mirrored version of figure 4.32, which is expected. Similar to the the increasing velocity, there seems to be an optimum for this metric when driving the truck at $50\,\mathrm{km\,h^{-1}}$ in a steady-state circle with radius of 100 m. Table 4.1 gives a lateral acceleration $a_y = 1.94\,\mathrm{m\,s^{-2}}$ for the case when the observability metric assumes its lowest value during the two variable speed maneuvers presented in this section.

As mentioned earlier, when looking at C_f and C_r from figures 4.30 and 4.31, both estimates started trending upwards when the longitudinal velocity was $v_x = 50\,\mathrm{m\,s^{-1}}$. The corresponding lateral acceleration was $a_y = 0.7\,\mathrm{m\,s^{-2}}$ shown in table 4.1.

Table 4.1: Steady-state values for lateral acceleration a_y, measured by the body-mounted IMU with gravity corrections, driving around Route 2 at varying longitudinal velocities v_x. Each value was taken as the sample mean μ over the corresponding time-intervals marked by colors in the figures of this section. Gray cells show the largest standard deviation σ.

	v_x [km/h]	20	30	40	50	60
a_y	μ [m/s^2]	3.10E−1	6.99E−1	1.24	1.94	2.80
	σ [m/s^2]	1.18E−2	1.06E−4	7.95E−3	4.86E−5	2.98E−5

Table 4.2: Steady-state values for side-slip angle (SSA) α and normal force F_z measured at the contact patch of each corresponding wheel, driving around Route 2 at varying longitudinal velocities v_x. The quantities are expressed in the wheel reference frame. Each value was taken as the sample mean μ over each respective 50 s steady-state interval. Gray cells indicate the largest standard deviation σ.

(a) Value for the **front left** wheel.

	v_x [km/h]	20	30	40	50	60
α	μ [rad]	−1.16E−4	−4.41E−3	−1.04E−2	−1.79E−2	−2.74E−2
	σ [rad]	1.93E−5	5.59E−5	6.13E−5	6.18E−5	6.78E−5
F_z	μ [N]	2.33E4	2.28E4	2.20E4	2.10E4	1.97E4
	σ [N]	2.47	6.99	8.42	8.05	8.35

(b) Value for the **front right** wheel.

	v_x [km/h]	20	30	40	50	60
α	μ [rad]	−6.78E−3	−1.10E−2	−1.69E−2	−2.43E−2	−3.36E−2
	σ [rad]	2.83E−5	6.45E−5	6.60E−5	6.39E−5	6.83E−5
F_z	μ [N]	2.41E4	2.46E4	2.54E4	2.63E4	2.75E4
	σ [N]	2.61	7.32	8.92	8.21	8.41

(c) Value for the **rear left** wheel.

	v_x [km/h]	20	30	40	50	60
α	μ [rad]	−2.29E−3	−5.27E−3	−9.53E−3	−1.56E−2	−2.45E−2
	σ [rad]	1.59E−5	4.00E−5	4.69E−5	5.44E−5	6.82E−5
F_z	μ [N]	9.01E3	8.30E3	7.31E3	6.05E3	4.52E3
	σ [N]	4.20	1.01E1	1.22E1	1.08E1	1.09E1

(d) Value for the **rear right** wheel.

	v_x [km/h]	20	30	40	50	60
α	μ [rad]	−2.25E−3	−5.16E−3	−9.34E−3	−1.52E−2	−2.40E−2
	σ [rad]	1.53E−5	3.84E−5	4.51E−5	5.24E−5	6.57E−5
F_z	μ [N]	1.02E4	1.09E4	1.19E4	1.32E4	1.48E4
	σ [N]	4.04	9.78	1.16E1	1.06E1	1.09E1

Table 4.2 shows the quantities related to side-slip extracted from IPG TruckMaker during simulation of the varying speed maneuver. The slip angle grows with velocity, reaching $\alpha = -0.0336$ rad at most out of all four wheels. For the front wheels, the

difference in vertical force goes from 800 N to 7800 N. For the rear axle, the difference goes from 1200 N to 10 300 N. It indicates a lateral load transfer at $v_x = 60\,\mathrm{km\,h^{-1}}$ equivalent to 790 kg at the front axle and 1050 kg at the rear axle.

4.2.4 Observability-Driven Update Strategy

This section presents results from the truck-only estimator described in section 3.3, using the update strategy described in section 3.4 to conditionally perform the UKF update step for the stiffness estimates C_f and C_r.

Figures 4.36 and 4.37 show a comparison of the observability metric to front- and rear stiffness parameter estimates for the truck driving Route 0 with always available velocity measurements. The update indicator signal (3.58) seems to correctly identify the straight driving maneuver based on the observability metric (2.59).

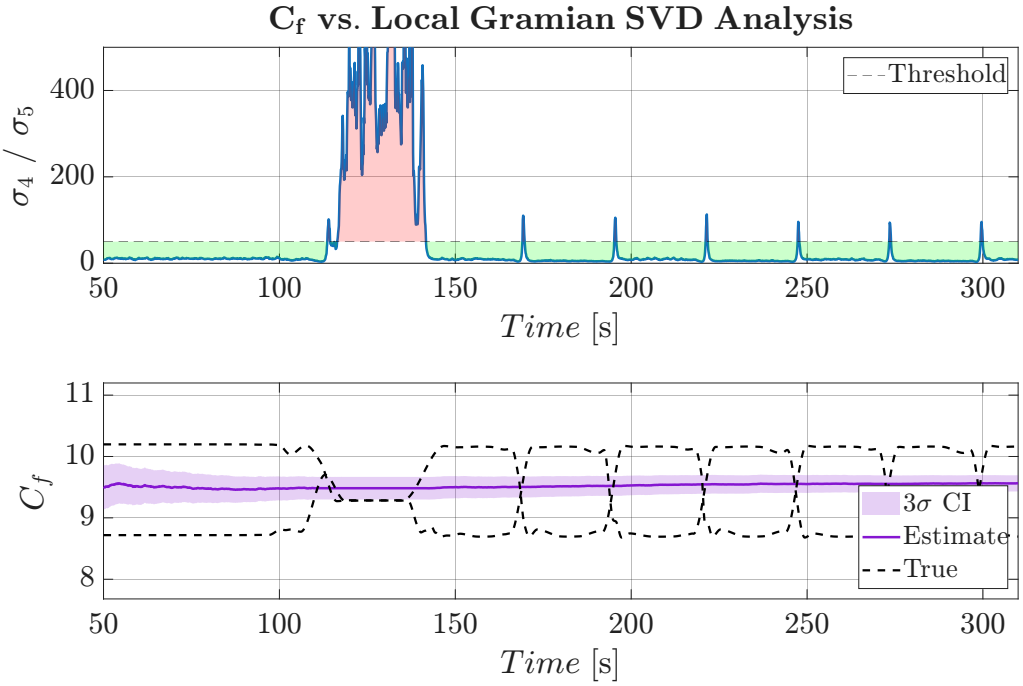

Figure 4.36: Tractor driving Route 0. The top graph shows (2.59). The threshold is indicated by the dashed line, and the boolean update signal is shown as shaded regions: green when updating the estimate, red when keeping the old estimate. The bottom graph shows the estimated tractor **front** TCS in purple and corresponding reference interval in black. The shaded region is the $\pm 3\sigma$ confidence interval.

There is no significant difference to not using the update strategy in this case, since the estimates converge early in the steady-state circle of Route 0. Both estimates look almost identical to their counter-parts in figures 4.14 and 4.15.

Trying the update strategy while varying the longitudinal velocity yielded figures 4.38 and 4.39. It's clear that the estimates maintain their initial values while driving at $v_x = 20\,\mathrm{km\,h^{-1}}$ with insufficient lateral dynamics. Interestingly, the uncertainty goes

down, precisely due to the estimates maintaining their values. The C_f estimate in figure 4.38 breaks the lower reference line about 25 s earlier than its counter-part in figure 4.30. The story is reversed for the rear estimate. C_r in figure 4.39 enters the reference interval around 20 s later than shown in figure 4.31 when not using the update strategy.

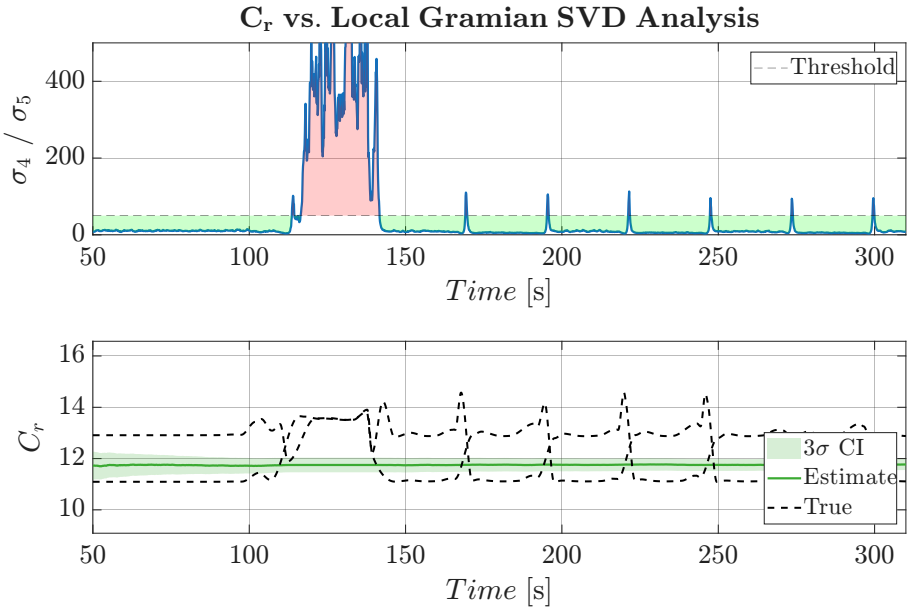

Figure 4.37: Tractor driving Route 0. The top graph shows (2.59). The threshold is indicated by the dashed line, and the boolean update signal is shown as shaded regions: green when updating the estimate, red when keeping the old estimate. The bottom graph shows the estimated tractor **rear** TCS in green and corresponding reference interval in black. The shaded region is the $\pm 3\sigma$ confidence interval.

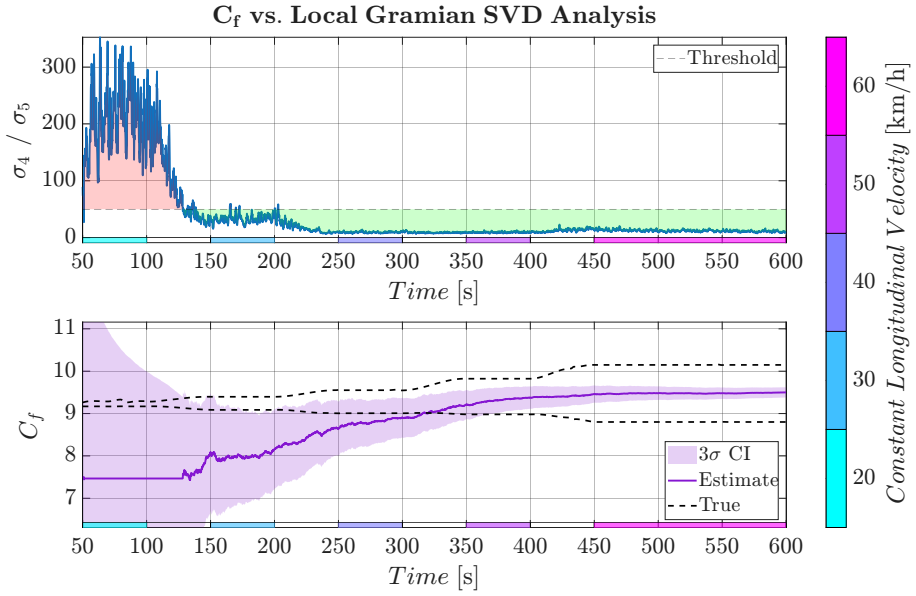

Figure 4.38: Tractor driving Route 2 at increasing velocities. The top graph shows (2.59). The threshold is indicated by the dashed line, and the boolean update signal is shown as shaded regions: green when updating the estimate, red when keeping the old estimate. The bottom graph shows the estimated tractor **front** TCS in purple with corresponding reference interval in black, driving a steady-state circle at varying velocities. The shaded region is the $\pm 3\sigma$ confidence interval. Steady-state velocities are indicated by colored patches on the horizontal axis.

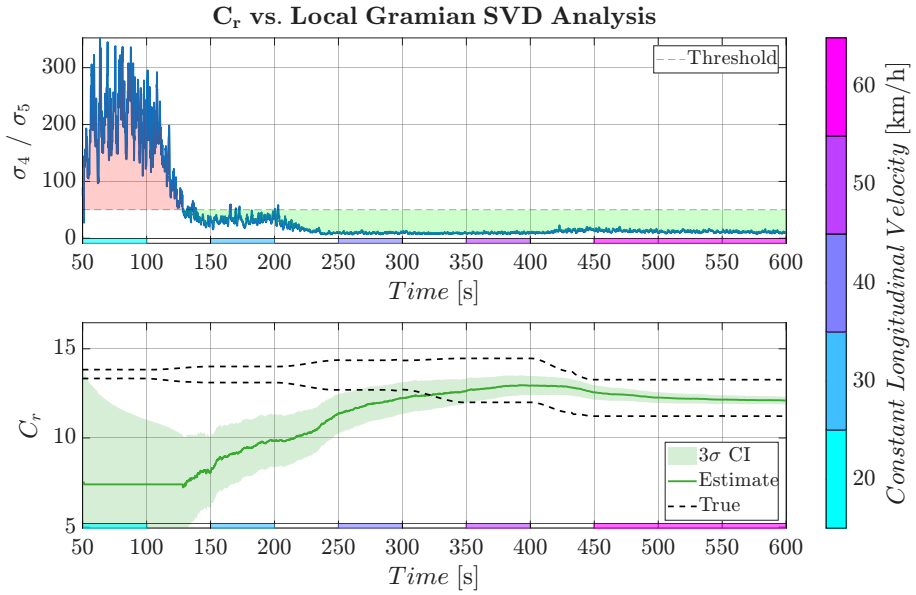

Figure 4.39: Tractor driving Route 2 at increasing velocities. The top graph shows (2.59). The threshold is indicated by the dashed line, and the boolean update signal is shown as shaded regions: green when updating the estimate, red when keeping the old estimate. The bottom graph shows the estimated tractor **rear** TCS in green with corresponding reference interval in black, driving a steady-state circle at varying velocities. The shaded region is the $\pm 3\sigma$ confidence interval. Steady-state velocities are indicated by colored patches on the horizontal axis.

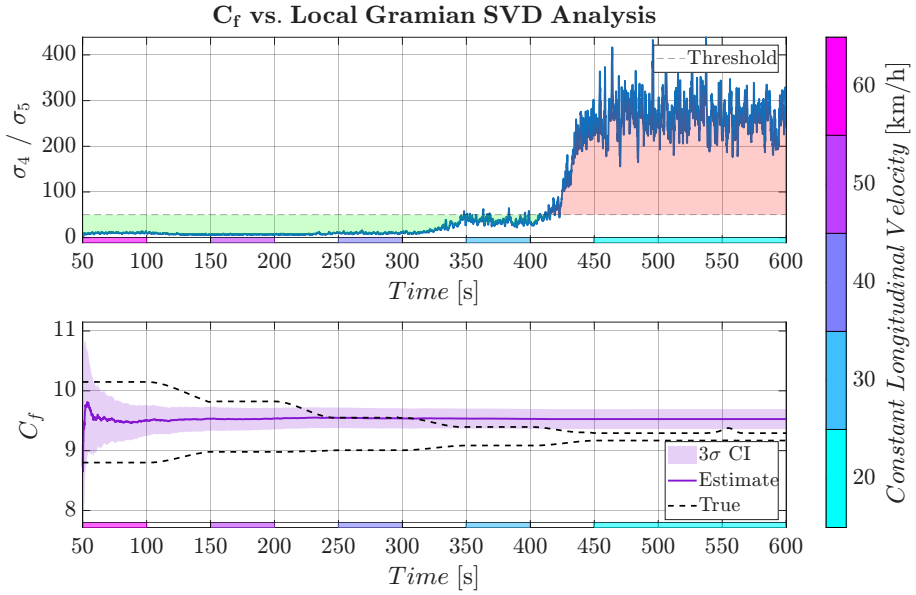

Figure 4.40: Tractor driving Route 2 at decreasing velocities. The top graph shows (2.59). The threshold is indicated by the dashed line, and the boolean update signal is shown as shaded regions: green when updating the estimate, red when keeping the old estimate. The bottom graph shows the estimated tractor **front** TCS in purple with corresponding reference interval in black, driving a steady-state circle at varying velocities. The shaded region is the $\pm 3\sigma$ confidence interval. Steady-state velocities are indicated by colored patches on the horizontal axis.

Figures 4.40 and 4.41 show the estimated stiffness parameters compared to the observability metric, while driving Route 2 at decreasing velocities. The estimates converge in the beginning while driving at $v_x = 60\,\mathrm{km\,h^{-1}}$, but as the velocity decreases, they fail to adapt. Once the velocity hits $20\,\mathrm{km\,h^{-1}}$ and the update indicator signal turns of, the estimates maintain values that are outside the reference interval until the end of the simulation.

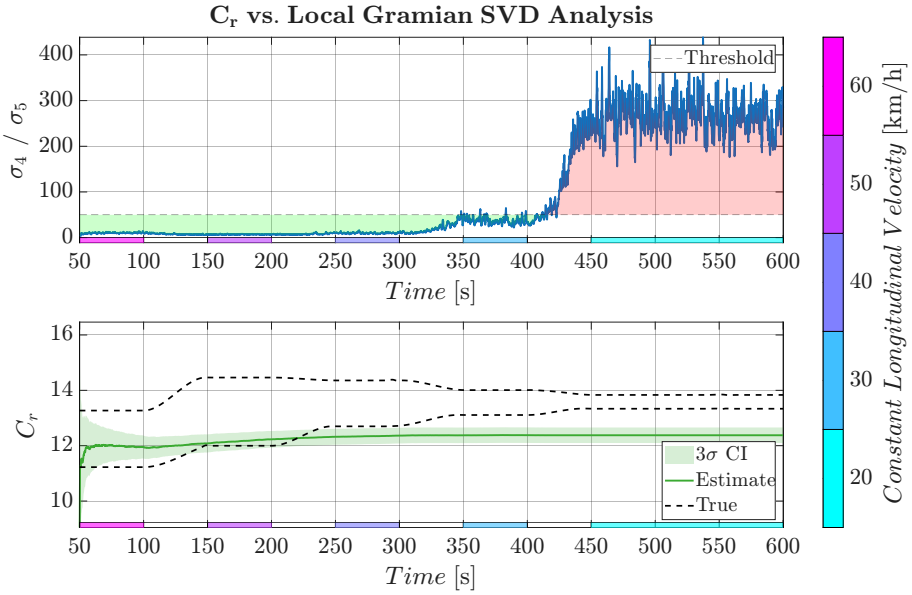

Figure 4.41: Tractor driving Route 2 at decreasing velocities. The top graph shows (2.59). The threshold is indicated by the dashed line, and the boolean update signal is shown as shaded regions: green when updating the estimate, red when keeping the old estimate. The bottom graph shows the estimated tractor **rear** TCS in green with corresponding reference interval in black, driving a steady-state circle at varying velocities. The shaded region is the $\pm 3\sigma$ confidence interval. Steady-state velocities are indicated by colored patches on the horizontal axis.

4.3 Stiffness Estimation Error Propagation

This section presents the results from the error propagation study described in section 3.4.3. The states C_f and C_r are constant during simulation. The estimates for lateral velocity v_y and lateral acceleration a_y (force-equivalent) are shown in figures 4.42 and 4.43, respectively. The results have been sliding-window-averaged for visual clarity, at the expense of accuracy.

The estimated value for C_r was around 11.75, as shown in figure 4.15. The estimated v_y for $C_r = 10$, a difference of 1.75 compared to ground truth, was deviating from the true value by $0.05\,\mathrm{m\,s^{-1}}$ as shown in figure 4.42. The deviation shows up during the steady state circle from time 50 s to 100 s and in the figure eight after time 140 s.

Lateral acceleration, shown in figure 4.43, tells a similar story. The intermediate state shows a deviation of $-0.2\,\mathrm{m\,s^{-2}}$ for $C_r = 10$, compared to the reference CoG acceleration during the steady-state circle. For $C_r = 14$, which is a stiffness difference of -2.25 compared to ground truth, a_y deviates $0.2\,\mathrm{m\,s^{-2}}$. Figure 4.43 seems to indicate that the best value for C_r is between 11 and 12 when keeping $C_f = 9.5$ for Route 0 and always-available velocity measurements, at least in terms of lateral acceleration.

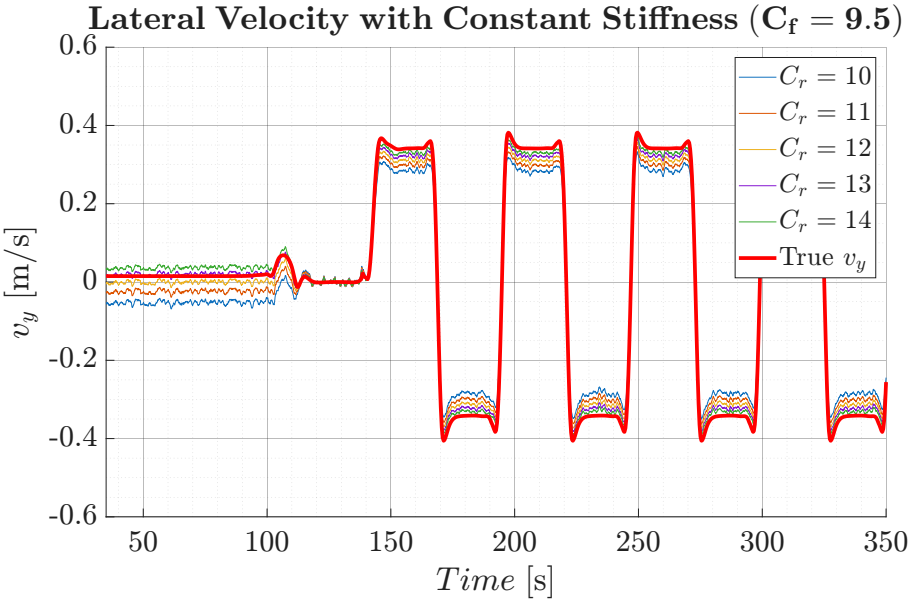

Figure 4.42: Truck-only lateral velocity estimates while keeping cornering stiffness constant, driving Route 0 with no speed limit. The true lateral velocity as given by the simulation environment is shown in red.

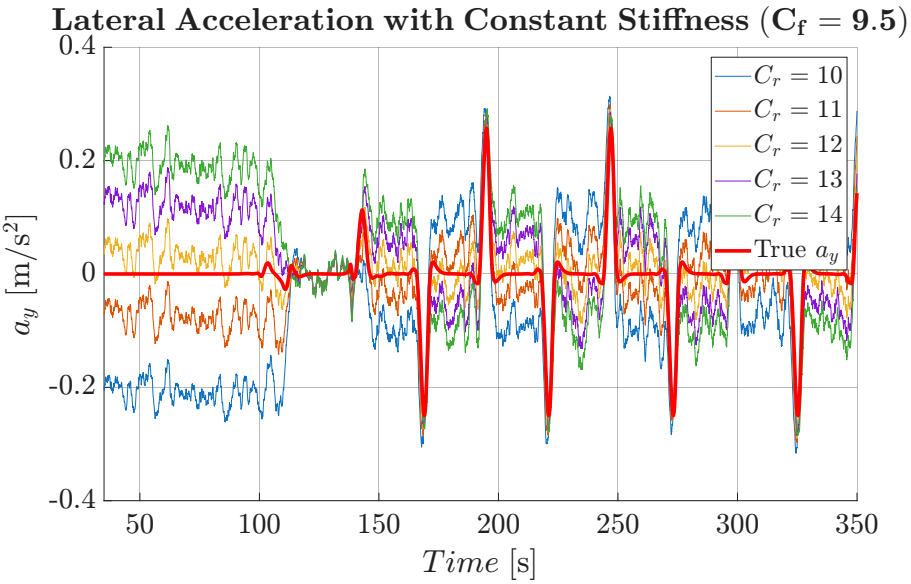

Figure 4.43: Truck-only lateral acceleration intermediate state when keeping cornering stiffness constant, driving Route 0 with no speed limit. The true lateral acceleration from the vehicle's CoG, given by the simulation environment, is shown in red.

4.4 Two-Track Model Estimation Results

This section presents the estimation results obtained using the two-track tractor model implemented in IPG TruckMaker together with the estimator formulation described in section 3.5. Compared to the single-track formulation, the two-track model separately estimates the left and right tire cornering stiffness. The evaluated maneuver is identical to the one used for the single-track model, with one major difference regarding the availability of velocity measurements. In this case, the velocity measurements remain available during the entire test scenario. The estimator performance is evaluated for tractor longitudinal velocity, lateral velocity, yaw rate, and individual tire cornering stiffness estimation for all four tractor wheels. However, only the tire cornering stiffness estimation results are presented in this section, while the remaining vehicle state estimation results are provided in Appendix A.

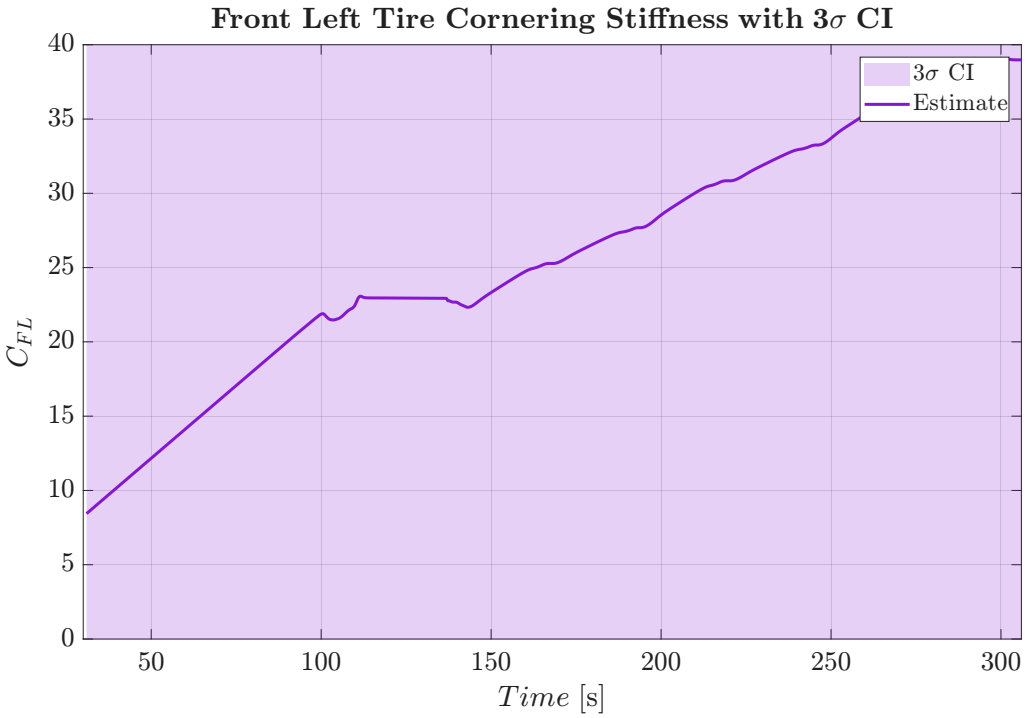

Figure 4.44: Estimated front-left cornering stiffness together with the estimated 3σ confidence interval.

Figure 4.44 illustrates the estimated front-left tire cornering stiffness together with the corresponding 3σ confidence interval. As can be seen, the estimate does not converge to a single steady-state value. The 3σ confidence interval reaches approximately ± 300. For improved visibility, the plotted axis range is clipped to better highlight the estimator behavior.

Figure 4.45 shows a similar behavior for the front-right tire cornering stiffness. The estimate does not converge to a single value, and the 3σ confidence interval again reaches approximately ± 300. For improved visibility, the plotted axis range is clipped.

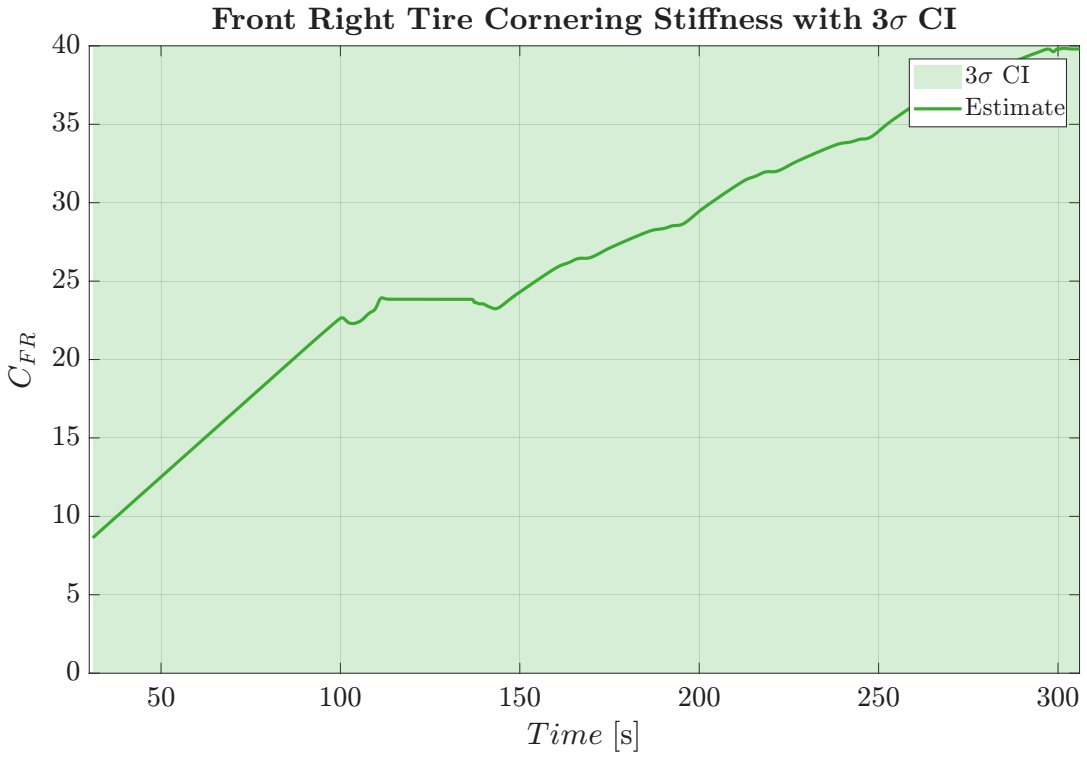

Figure 4.45: Estimated front-right cornering stiffness together with the estimated 3σ confidence interval.

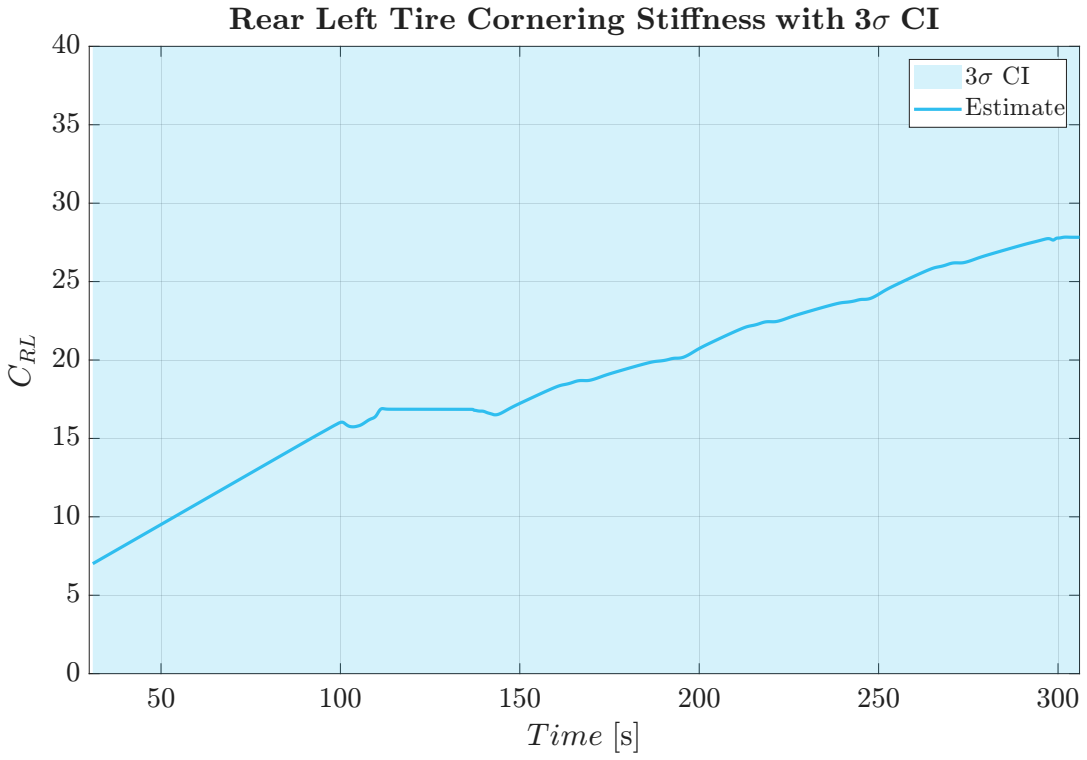

Figure 4.46: Estimated rear-left cornering stiffness together with the estimated 3σ confidence interval.

Figure 4.46 shows the same behavior for the rear-left tire cornering stiffness. The estimate remains non-convergent, and the 3σ confidence interval reaches approximately ± 300. For improved visibility, the plotted axis range is clipped.

Figure 4.47 shows the same behavior for the rear-right tire cornering stiffness. The estimate remains non-convergent, and the 3σ confidence interval reaches approximately ± 300. For improved visibility, the plotted axis range is clipped.

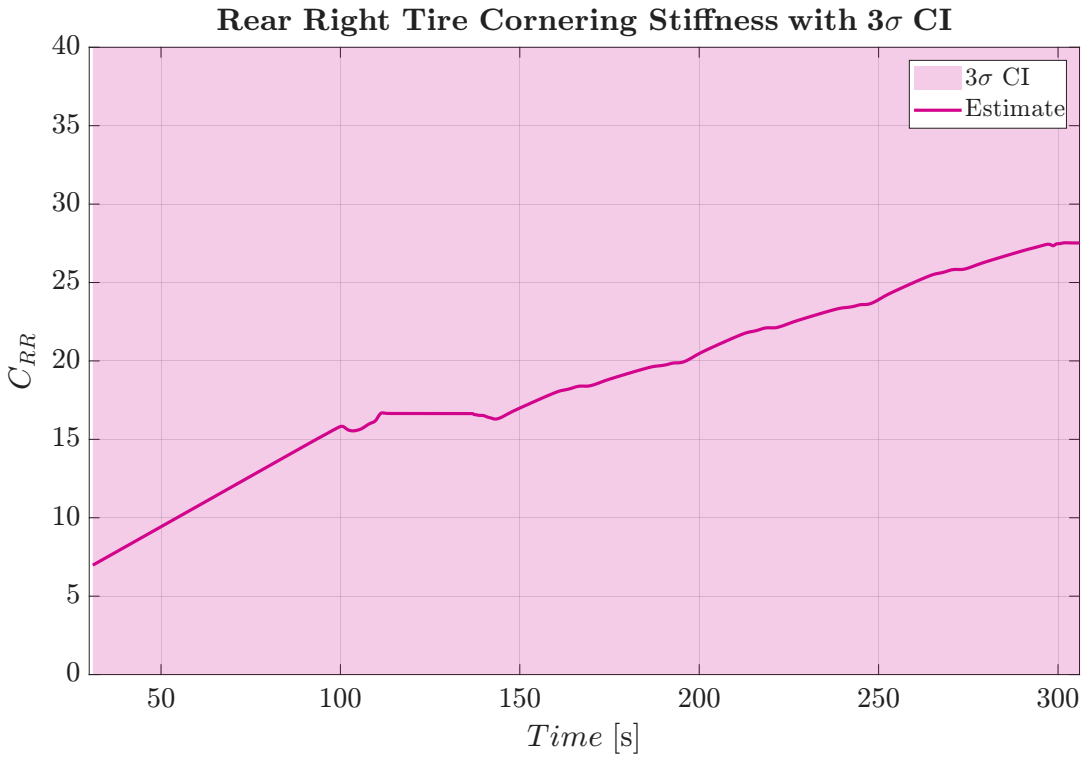

Figure 4.47: Estimated rear-right cornering stiffness together with the estimated 3σ confidence interval.

4.5 Truck and Trailer Estimation Results

This section presents the estimation results obtained using the articulated truck and trailer model implemented in IPG TruckMaker together with the estimator formulation described in Section 3.6. The evaluated maneuver is identical to the one used for the single-track model. The estimation performance is evaluated for both tractor and trailer states, including longitudinal and lateral vehicle motion, yaw dynamics, articulation angle, and tire cornering stiffness estimation. The presented results illustrate the estimator behavior under degraded sensing conditions, where direct velocity measurements are disabled at $t \geq 95\,\mathrm{s}$.

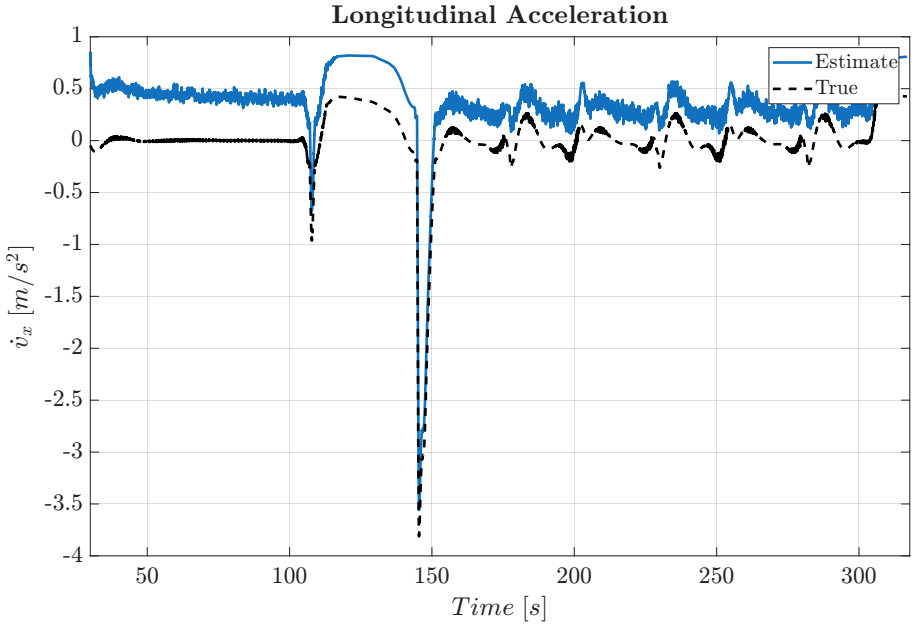

Figure 4.48: Comparison between the estimated (blue solid line) and true (black dashed line) longitudinal acceleration of the articulated vehicle.

Figure 4.48 illustrates the estimated and true longitudinal acceleration of the articulated vehicle. As can be seen, the estimated signal exhibits similar dynamic behaviour as the reference signal, although some deviations are present during parts of the maneuver. Overall, the estimator captures the longitudinal dynamics of the coupled tractor–trailer system reasonably well.

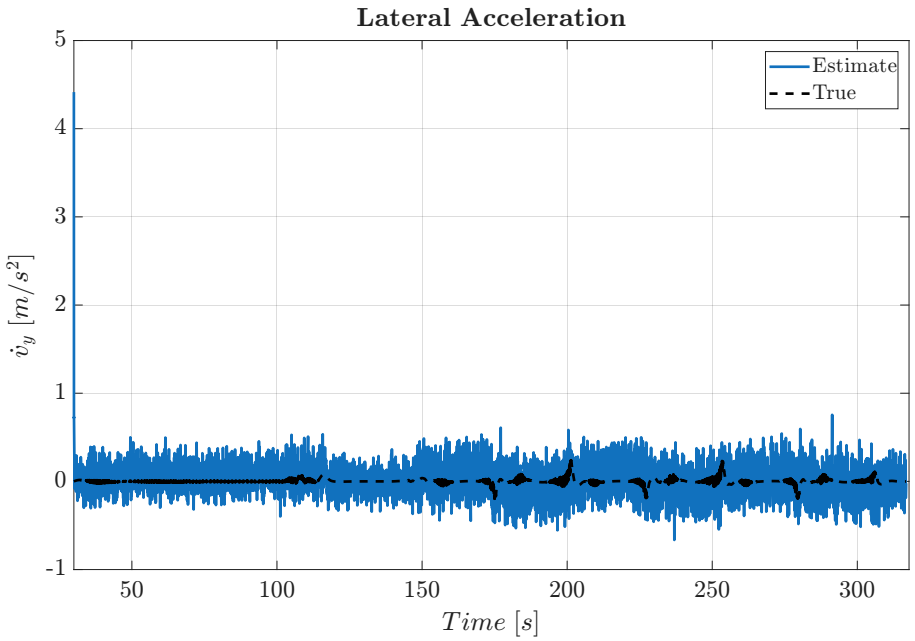

Figure 4.49: Comparison between the estimated (blue solid line) and true (black dashed line) lateral acceleration of the articulated vehicle.

Figure 4.49 illustrates the estimated and true lateral acceleration of the articulated vehicle. As can be seen, the estimated signal follows the reference closely and captures the main lateral dynamics of the coupled tractor–trailer system throughout the entire maneuver.

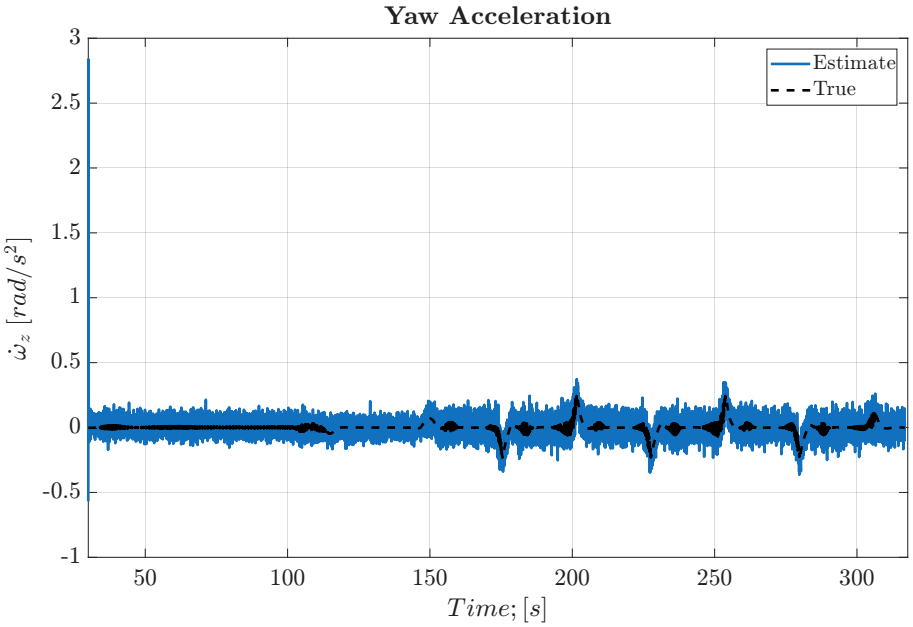

Figure 4.50: Comparison between the estimated (blue solid line) and true (black dashed line) yaw acceleration of the articulated vehicle.

Figure 4.50 illustrates the estimated and true yaw acceleration of the tractor. The estimated signal follows the reference well and captures the main rotational dynamics of the vehicle.

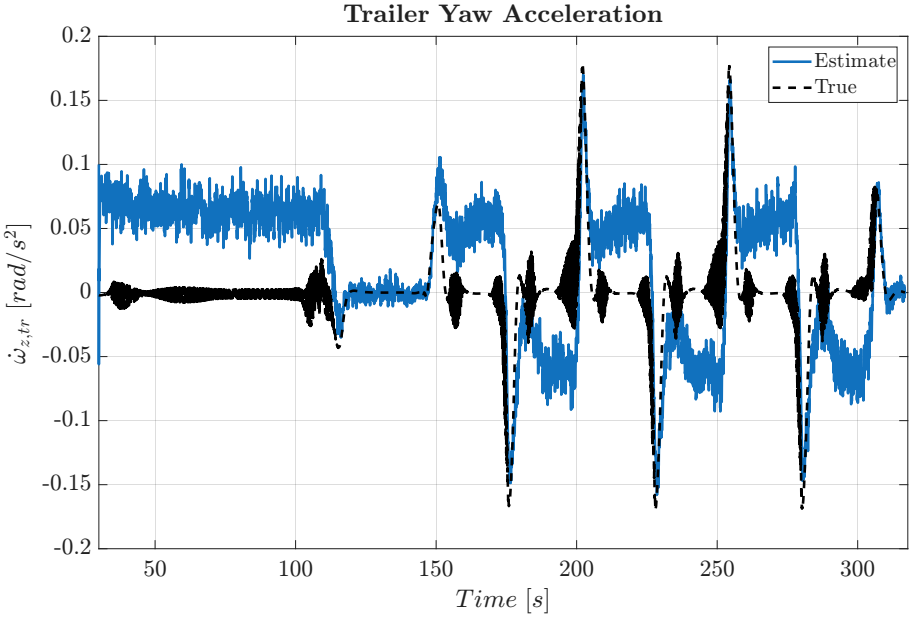

Figure 4.51: Comparison between the estimated (blue solid line) and true (black dashed line) trailer yaw acceleration of the articulated vehicle.

Figure 4.51 illustrates the estimated and true trailer yaw acceleration for the coupled tractor–trailer system. As can be seen, the estimated signal captures the trailer yaw dynamics. However, clear deviations can be observed, especially during periods of constant yaw acceleration, while the transient peaks are captured accurately by the estimator.

Figure 4.52 illustrates the estimated and true longitudinal velocity of the tractor together with the $\pm 3\sigma$ confidence interval, as well as the point in time where direct velocity measurements become unavailable, for the coupled tractor–trailer system. The estimate follows the true signal closely throughout the Route 0 maneuver. Small deviations can be observed, but overall the estimator reproduces the system dynamics well.

Figure 4.53 illustrates the estimated and true lateral velocity of the tractor together with the 3σ confidence interval. The estimate closely follows the true signal during the entire Route 0 maneuver.

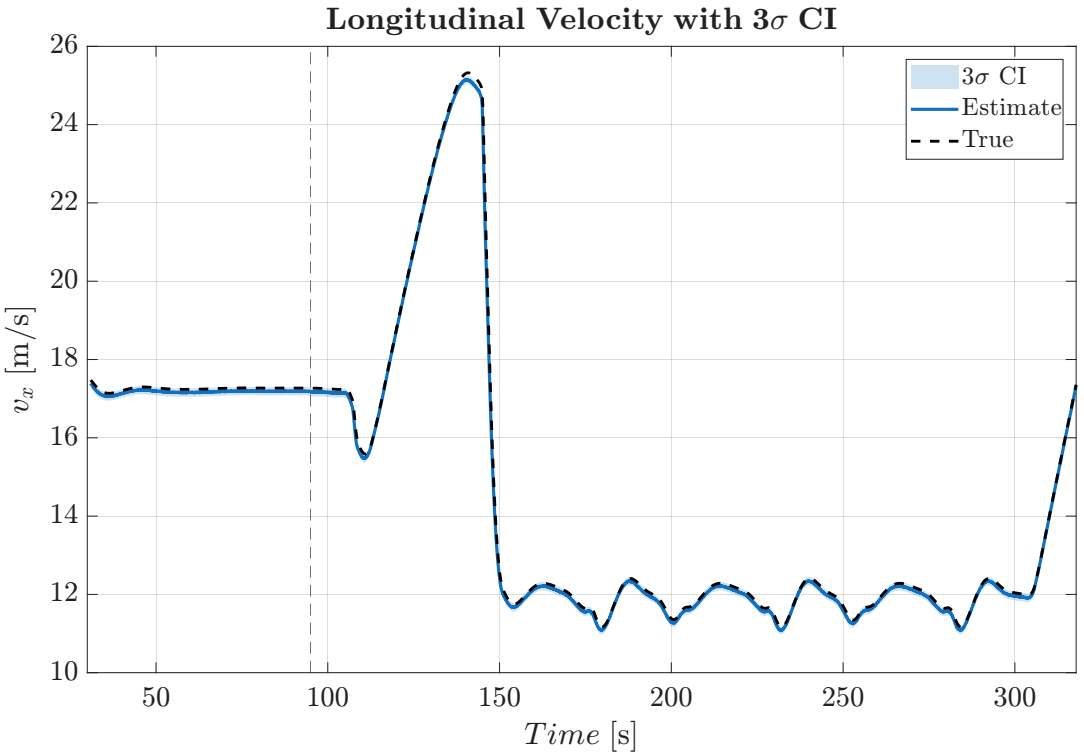

Figure 4.52: Comparison between the estimated (blue solid line), true (black dashed line), and $\pm 3\sigma$ bounds of the tractor longitudinal velocity in a coupled tractor–trailer system. The vertical dashed line indicates the time at which velocity measurements become unavailable.

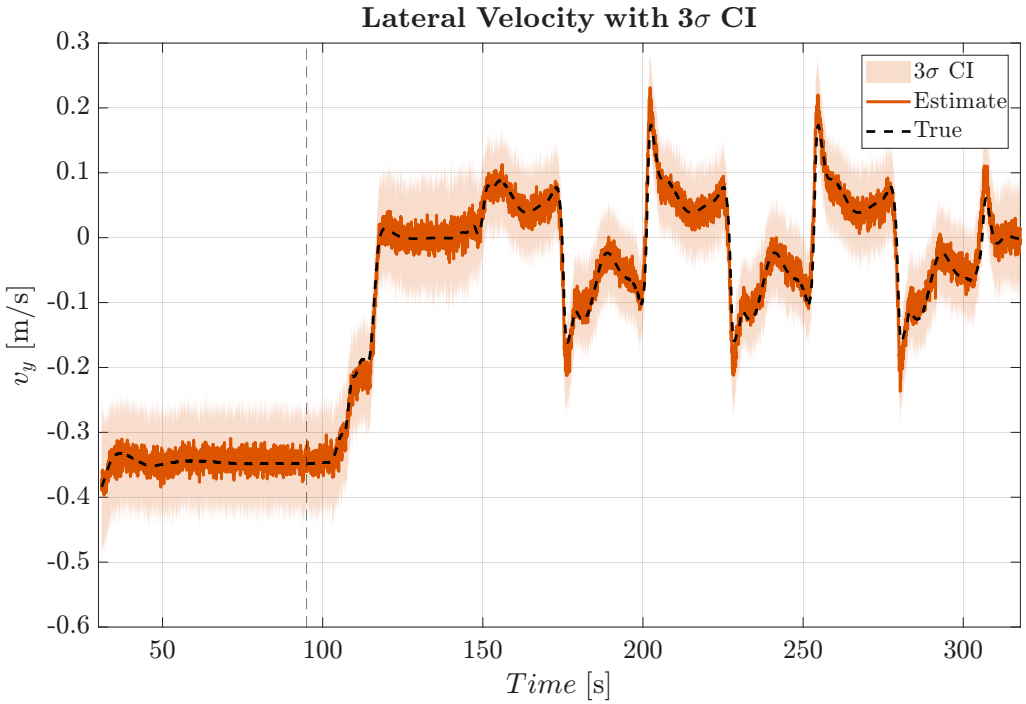

Figure 4.53: Comparison between the estimated (orange solid line), true (black dashed line), and $\pm 3\sigma$ bounds of the tractor lateral velocity in a coupled tractor–trailer system. The vertical dashed line indicates the time at which velocity measurements become unavailable.

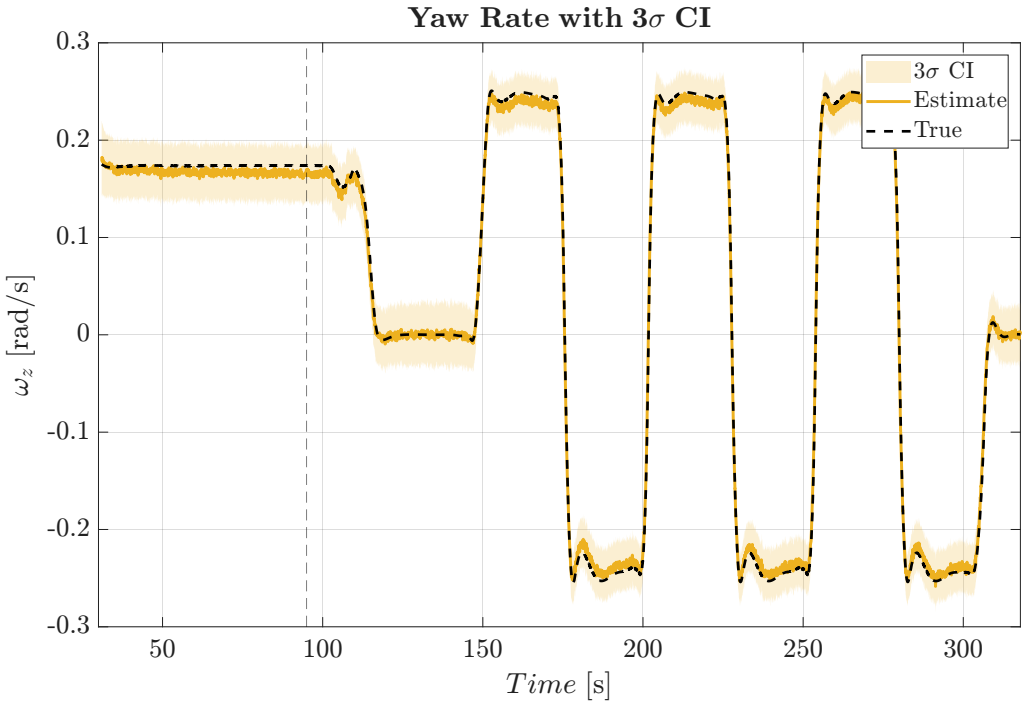

Figure 4.54: Comparison between the estimated (yellow solid line), true (black dashed line), and $\pm 3\sigma$ bounds of the tractor yaw rate in a coupled tractor–trailer system.

Figure 4.54 illustrates the tractor estimated yaw rate and the estimated 3σ confidence interval together with the true yaw rate obtained directly from the simulation environment for a coupled tractor–trailer system. Except the negligible deviation the estimate follows the true signal very well during the entire Route 0 maneuver.

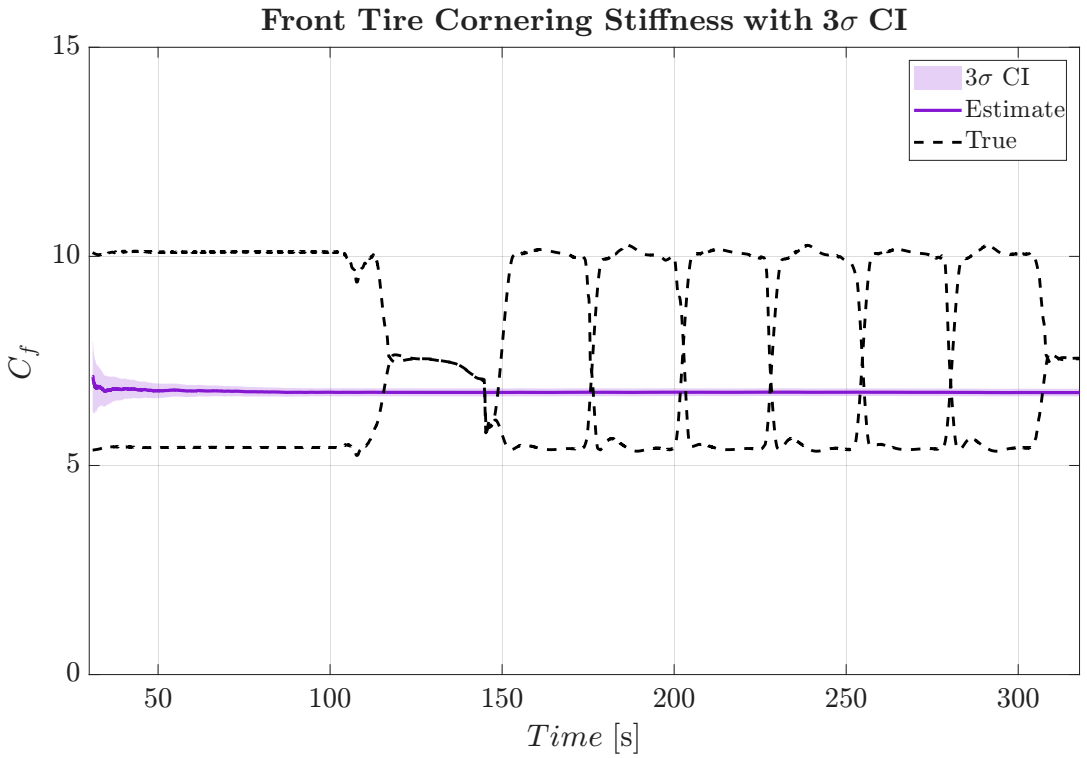

Figure 4.55: Estimated tractor front tire cornering stiffness (purple solid line) together with the corresponding reference interval (black solid lines) and $\pm 3\sigma$ confidence bounds.

Figure 4.55 illustrates the estimated front tire cornering stiffness of the tractor together with the corresponding reference interval and 3σ confidence bounds. The estimate remains within the reference interval and stays constant, consistent with the model assumptions.

Figure 4.56 illustrates the estimated rear tractor tire cornering stiffness together with the corresponding reference interval and $\pm 3\sigma$ confidence bounds. The estimate lies close to the upper boundary of the reference interval, but slight variations can be observed over time.

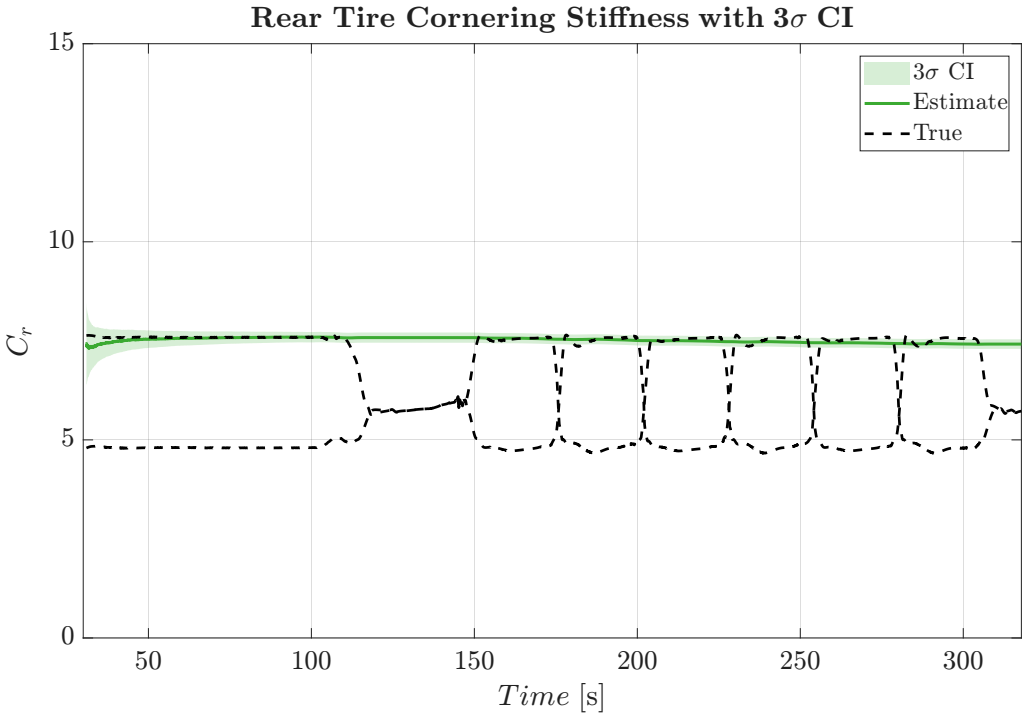

Figure 4.56: Estimated tractor rear tire cornering stiffness (green solid line) together with the corresponding reference interval (black solid lines) and $\pm 3\sigma$ confidence bounds.

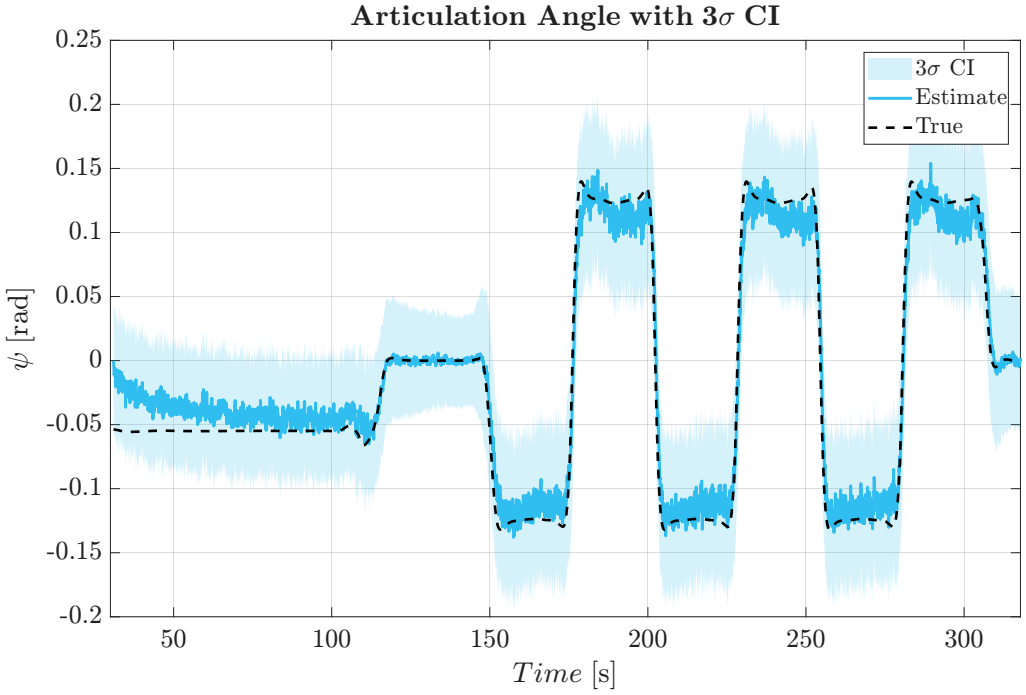

Figure 4.57: Estimated articulation angle (sky blue solid line) between the tractor and trailer together with the reference signal (black solid line) and $\pm 3\sigma$ confidence bounds.

Figure 4.57 illustrates the estimated articulation angle together with the corresponding reference signal and $\pm 3\sigma$ confidence interval. The estimator tracks the articulation dynamics of the coupled system accurately. Initially, a deviation is observed, but after a few seconds the estimate follows the reference signal well and remains stable and bounded throughout the maneuver.

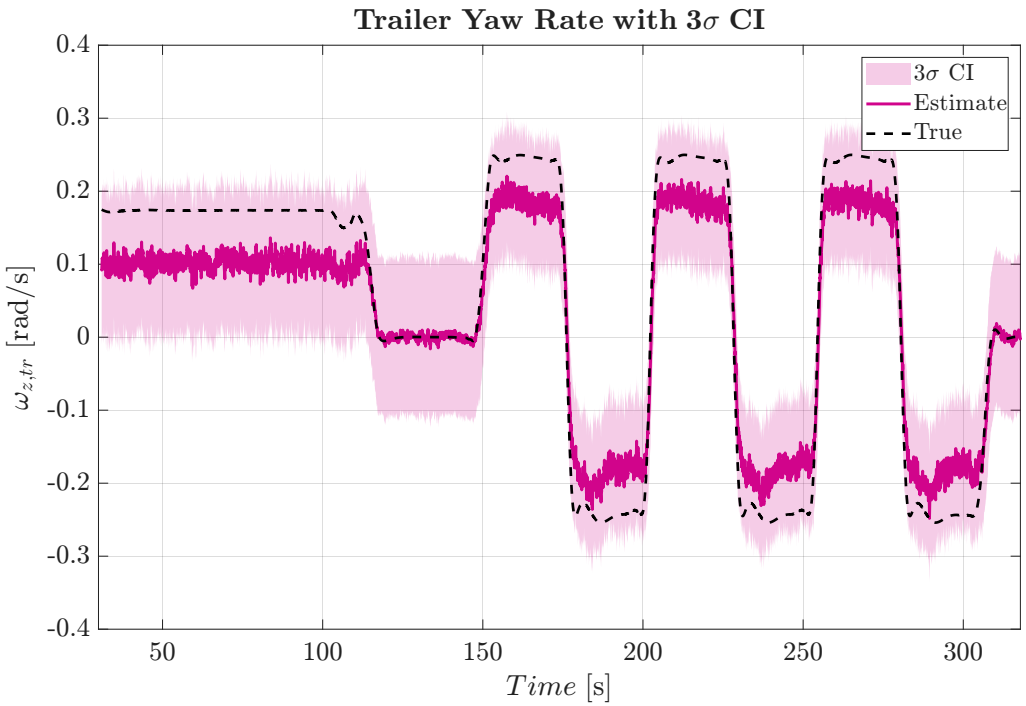

Figure 4.58: Comparison between the estimated (pink solid line), true (black dashed line), and $\pm 3\sigma$ bounds of the trailer yaw rate in the coupled tractor trailer system.

Figure 4.58 illustrates the estimated trailer yaw rate together with the corresponding reference signal and $\pm 3\sigma$ confidence interval. A clear deviation between the estimate and the reference can be observed, while the uncertainty remains bounded throughout the entire maneuver.

Figure 4.59 illustrates the estimated trailer rear tire cornering stiffness together with the corresponding reference interval and $\pm 3\sigma$ confidence bounds. The estimate exceeds the upper boundary of the reference interval and remains there for a period of time. It can be observed that the uncertainty is larger compare to the tractor case.

Figure 4.60 illustrates the longitudinal velocity estimation error together with the corresponding $\pm 3\sigma$ confidence bounds. It can be observed that the error remains inside the $\pm 3\sigma$ confidence bounds for most of the maneuver, with only small transient deviations.

Figure 4.61 illustrates the lateral velocity estimation error together with the corresponding $\pm 3\sigma$ confidence bounds. The error fluctuates around zero and remains well bounded.

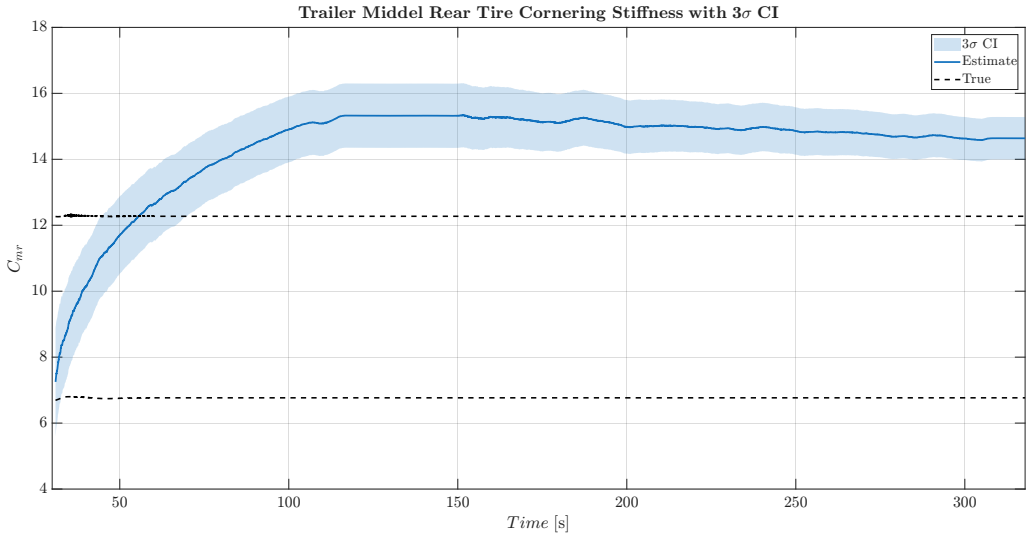

Figure 4.59: Estimated trailer rear tire cornering stiffness (blue solid line) together with the corresponding reference interval (black dash line) and $\pm 3\sigma$ confidence bounds.

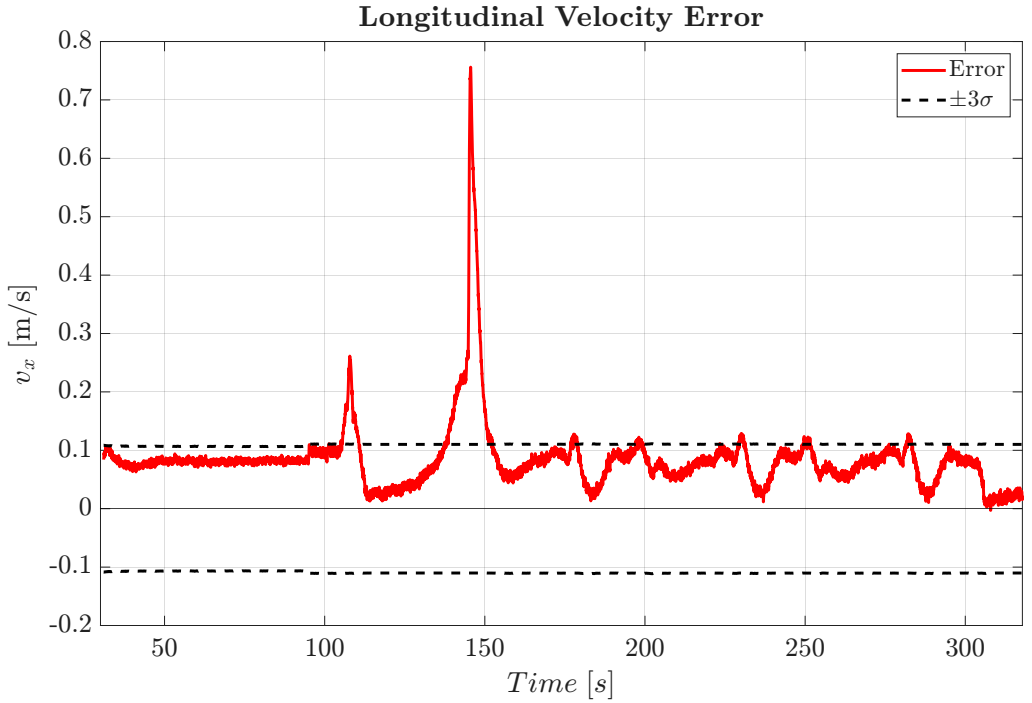

Figure 4.60: Tractor longitudinal velocity estimation error (red solid line) with $\pm 3\sigma$ confidence bounds (black dashed lines).

Figure 4.62 illustrates the yaw rate estimation error together with the corresponding $\pm 3\sigma$ confidence bounds. The error remains around zero and is generally well captured by the uncertainty bounds, with transient deviations

Figure 4.63 illustrates the NEES consistency test for the first three estimated truck states. It can be observed that the NEES remains within the theoretical confidence bounds for most of the maneuver even with the coupled tractor trailer system,

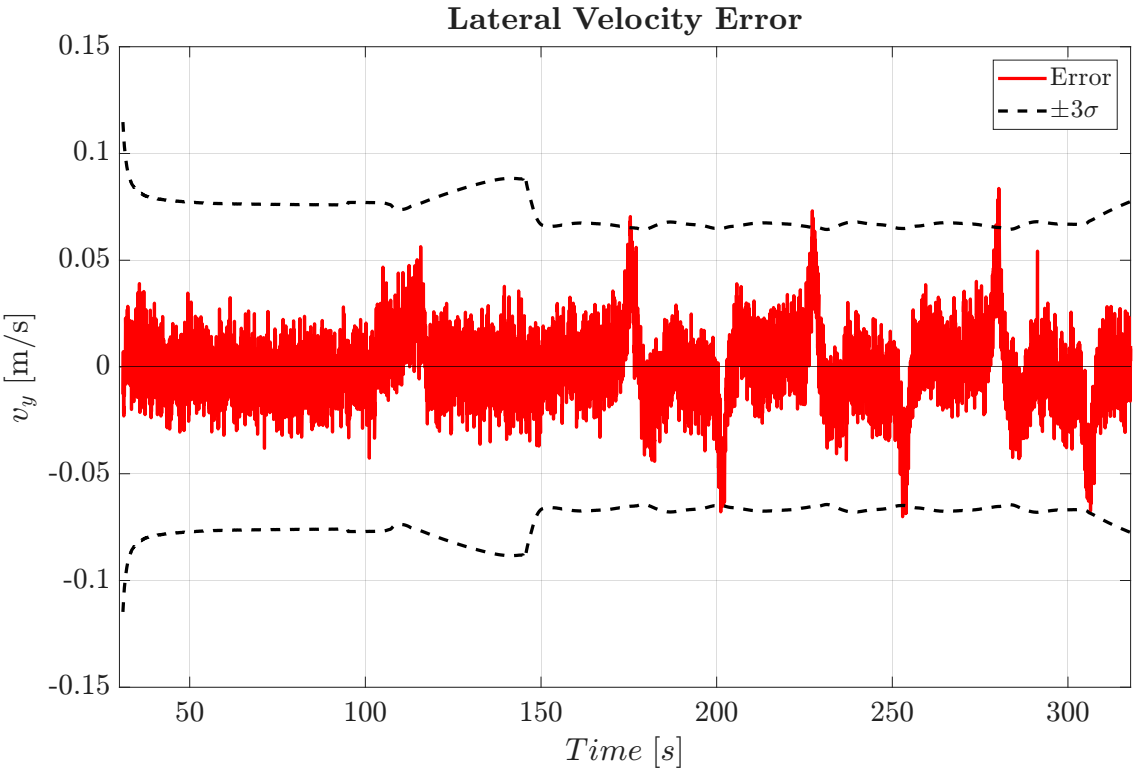

Figure 4.61: Tractor lateral velocity estimation error (red solid line) with $\pm 3\sigma$ bounds (black dash lines).

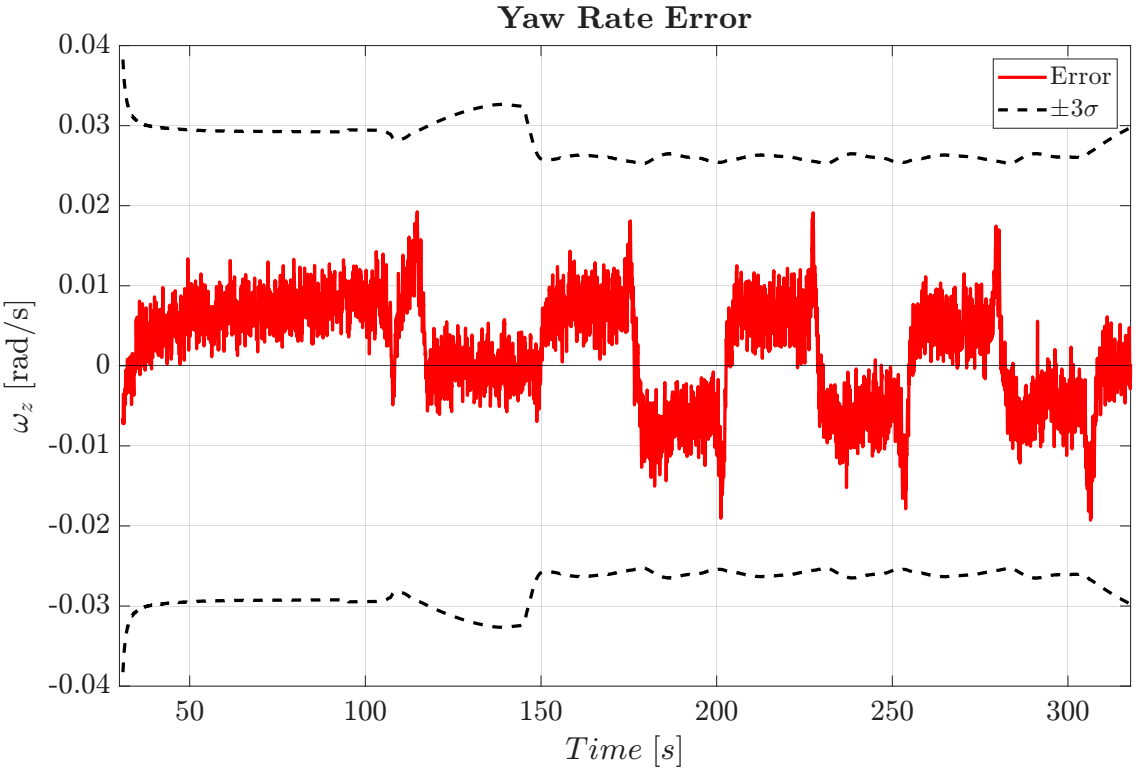

Figure 4.62: Tractor yaw rate estimation error (red solid line) with $\pm 3\sigma$ bounds (black dash line).

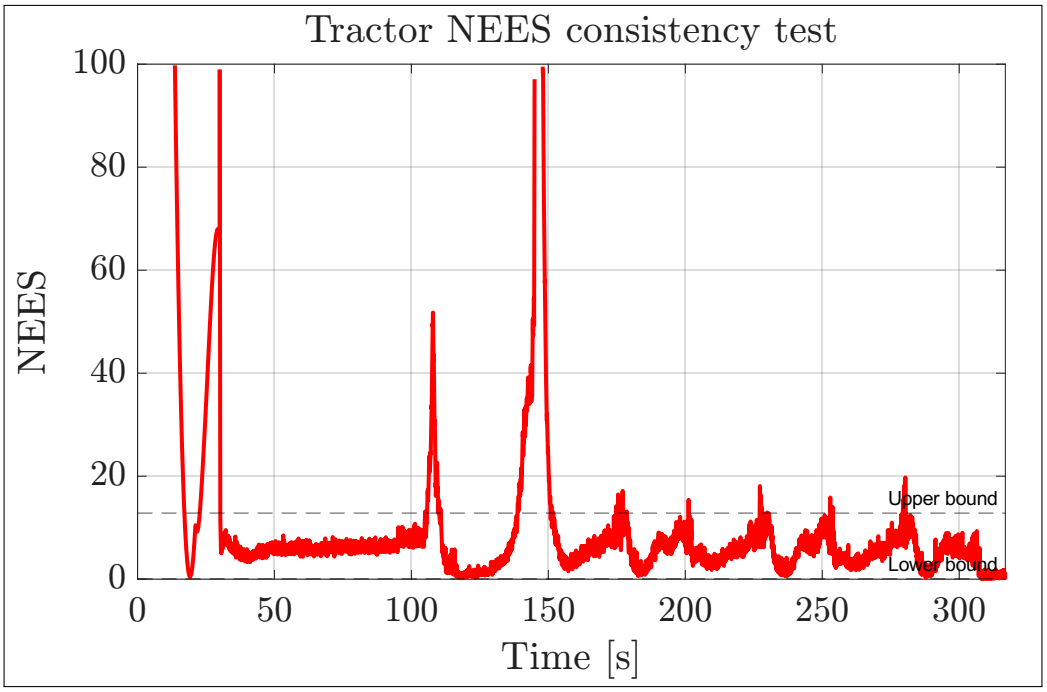

Figure 4.63: Normalized Estimation Error Squared (NEES) consistency test for the estimated tractor states together with the corresponding confidence bounds.

indicating that the estimator covariance is reasonably consistent with the observed estimation errors for the tractor.

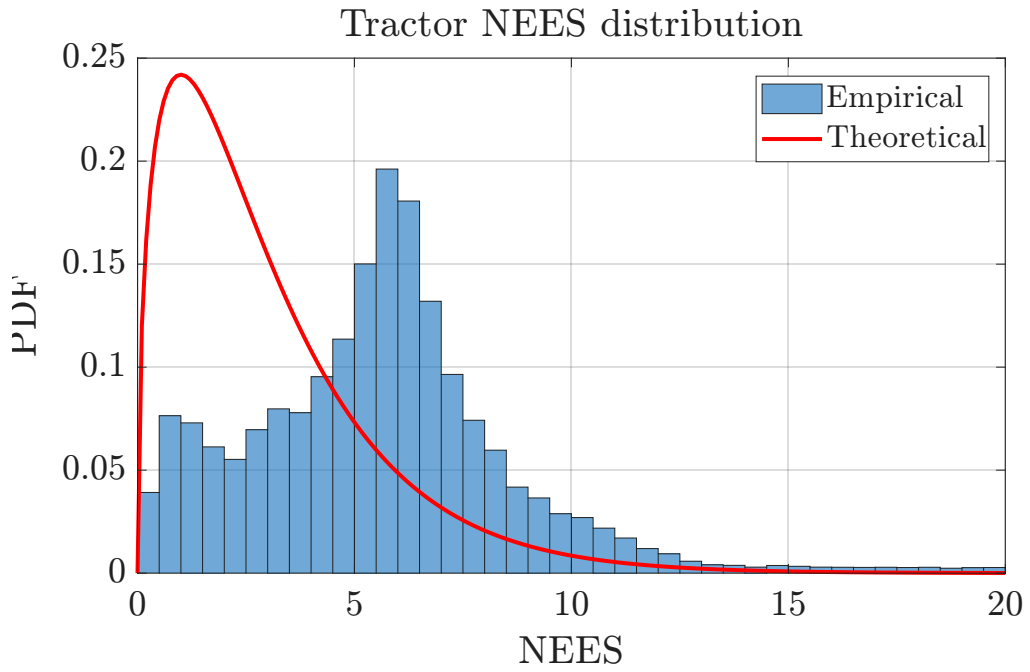

Figure 4.64: Empirical NEES distribution compared with the theoretical chi-square distribution for the considered state dimension.

Figure 4.64 illustrates the empirical NEES distribution together with the corresponding theoretical chi-square (χ^2) distribution. Here it can be observed, the overall dis-

tribution does not follows the theoretical trend reasonably well, indicating some inconsistency.

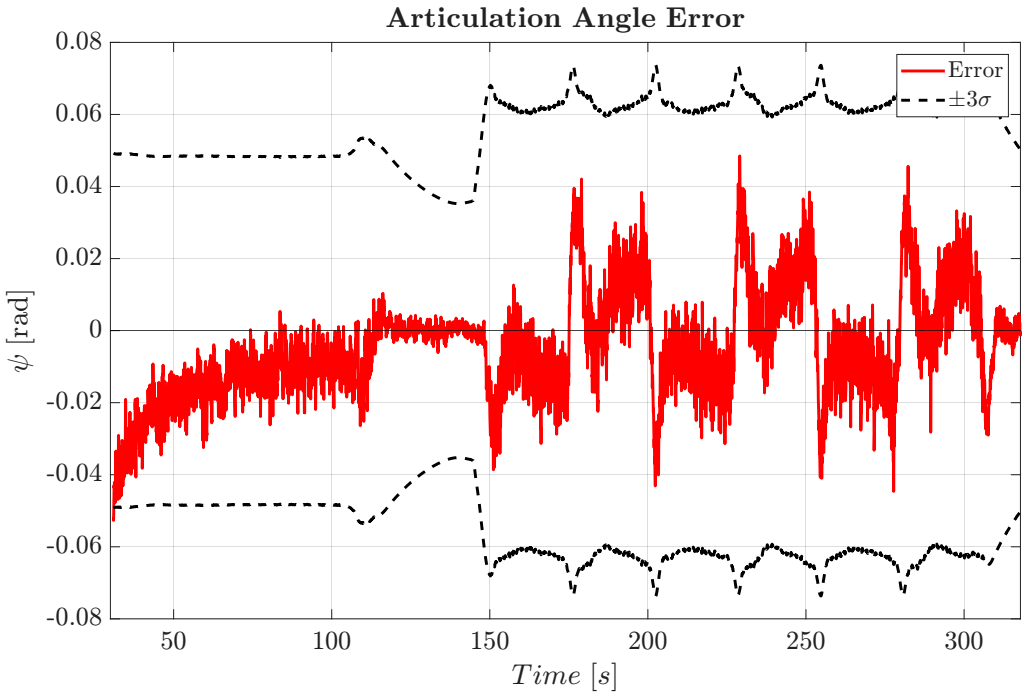

Figure 4.65: Articulation angle estimation error (red solid line) with $\pm 3\sigma$ bounds (black dash lines).

Figure 4.65 illustrates the articulation angle estimation error together with the corresponding $\pm 3\sigma$ confidence bounds. A initial deviation is visible, but it remains within the uncertainty bounds.The error stays almost around zero and remains within the confidence limits.

Figure 4.66 illustrates the trailer yaw rate estimation error together with the corresponding $\pm 3\sigma$ confidence bounds. The error shows larger deviations compared to the tractor states, but remains within the predicted uncertainty bounds.

Figure 4.67 illustrates the NEES consistency test for the estimated trailer yaw rate and articulation angle. It can be observed that the NEES is outside of the theoretical confidence bounds, indicating that the estimator covariance is not consistent with the observed estimation errors.

Figure 4.68 illustrates the empirical NEES distribution together with the corresponding theoretical chi-square (χ^2) distribution. Here it can be observed that the distribution does have completely another form of "distribution" compared to the theoretical, indicating inconsistency.

Figure 4.66: Trailer yaw rate estimation (red solid line) with $\pm 3\sigma$ bounds (black dash lines).

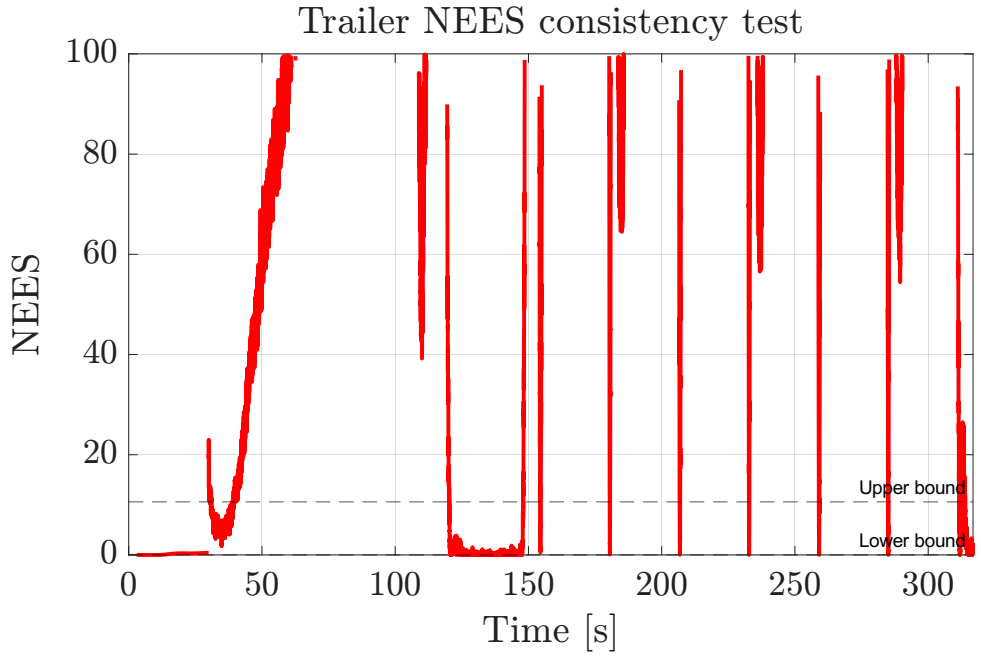

Figure 4.67: Normalized Estimation Error Squared (NEES) consistency test for the estimated trailer states together with the corresponding confidence bounds.

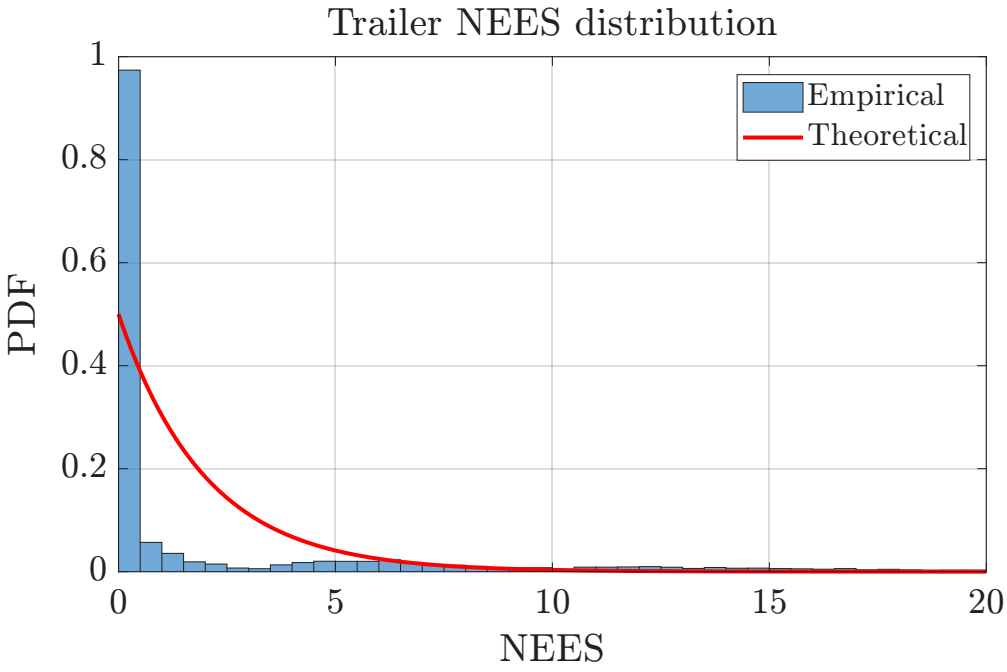

Figure 4.68: Empirical NEES distribution compared with the theoretical chi-square distribution for the considered state dimension.

5

Discussion

The findings of this study provide critical insights into the challenges and limitations of simultaneous state and parameter estimation for heavy articulated vehicles. By evaluating the proposed unscented Kalman filter (UKF) framework across both simulated environments and experimental real-world data, several fundamental behavioral characteristics of the estimator and the underlying vehicle models have been identified. The following sections will discuss each in more detail.

5.1 Model Complexity and Observability

A primary point of divergence observed in the results is the contrasting performance between the two-track and single-track models. While the single-track model successfully estimates lumped axle cornering stiffness, the two-track model struggles to identify individual tire cornering stiffnesses. This failure strongly suggests over-parameterization within the two-track framework. The driving scenario designed for this study modeled standard truck road maneuvers, but they generally lack independent lateral excitation between the left and right wheel pairs, so the individual tire stiffnesses remain practically unobservable given the current sensor suite.

This observability issue is compounded by the mathematical coupling inherent in the simultaneous estimation of lateral states (e.g., lateral velocity, v_y) and cornering stiffness parameters. This concurrent estimation architecture creates an adverse dependency: if the underlying linear vehicle model is structurally deficient—omitting essential degrees of freedom—the estimator tends to treat the cornering stiffness C as a free tuning variable to compensate for the unmodeled dynamics. Consequently, the filter can yield highly accurate lateral state estimates while converging on physically erroneous stiffness parameters. This can be seen in the stiffness estimate shown in figure 4.59: the missing dynamics in the vehicle model is compensated by a high value of C, over-shooting the reference interval.

5.2 Excitation Dependency and Update Strategy

The analysis of the local observability Gramian via Singular Value Decomposition highlights that parameter observability is strictly dependent on specific dynamic thresholds. The results indicate optimal observability occurs during maneuvers

exhibiting sufficient lateral excitation, such as cornering near $50\,\mathrm{km\,h^{-1}}$ with a lateral acceleration of approximately $1.94\,\mathrm{m\,s^{-1}}$ per table 4.1. To address parameter drift during low-excitation, straight-line driving, the implementation of a Gramian-based conditional update strategy proved highly effective. By suspending parameter updates when excitation falls below the observability threshold, the system successfully preserves previously estimated stiffness values, mitigating the vulnerability of the UKF to noise-induced drift.

5.3 Reality and the Non-Linear Assumption

Discrepancies between the IPG TruckMaker simulations and the MUSE experimental data underscore the fundamental limitations of assuming planar motion and the linear single-track assumption. Real-world heavy-duty vehicles exhibit complex roll, pitch, and suspension compliance dynamics that are inevitably omitted in simplified linear models, as was the case for the models used in this project.

This breakdown is particularly evident during fixed-radius steady-state circle maneuvers (section 4.2.3.2). As longitudinal velocity varies between $50\,\mathrm{km\,h^{-1}}$ and $60\,\mathrm{km\,h^{-1}}$, the stiffness reference interval shifts drastically, demonstrating that the assumption of a constant linear stiffness coefficient is unsuitable for shifting dynamic loads. While the estimator adapts to the required stiffness for a given maneuver—as hinted in figure 4.34 and confirmed in appendix A.2—it exhibits a distinct transient lag. This transient lag presents a major operational challenge: applications requiring accurate estimates to safely predict and execute maneuvers rely on exact parameters at the maneuver's onset. If the vehicle must perform the maneuver for an extended period to arrive at the correct axle stiffness, the predictive estimates will be inaccurate during the critical initial phase.

5.4 Articulated Dynamics and Filter Consistency

The statistical consistency of the filter, evaluated via the normalized estimation error squared (NEES) metric, reveals critical shortcomings in capturing the articulated dynamics. Specifically, the failure of the normalized estimation error squared (NEES) tests for the trailer yaw rate and articulation angle points to severe covariance underestimation or the presence of significant unmodeled nonlinearities. These inconsistencies are likely driven by complex hitch coupling forces and heavy dynamic load transfers originating from the substantial trailer mass ($31\,960\,\mathrm{kg}$). The linear tire assumption fundamentally breaks down under the severe, asymmetric load shifting characteristic of such heavy articulated configurations.

5.5 Sensor Degradation and System Resilience

The system's resilience was tested under degraded sensor conditions. When direct velocity measurements are denied, the UKF successfully maintains functionality by seamlessly transitioning to a reduced measurement set reliant on individual

wheel speeds, predicated on a zero-longitudinal-slip assumption. While this fallback mechanism introduces quantifiable differences in the longitudinal and lateral velocity error bounds compared to full sensor availability, it demonstrates the robustness of the estimator architecture in ensuring continued, albeit degraded, operation during sensor dropouts.

The error comparison for v_x, shown in figure 4.22, seems to suggest that the degraded sensor condition yielded a lower uncertainty in the longitudinal direction. We did not expect this result, and it seems erroneous. The vehicle model used a fixed tire radius to compute the longitudinal velocity based on wheel speed sensor data, while it should really have been an estimated effective wheel radius with an accompanying uncertainty. This might explain the sudden confidence during the degraded sensing condition.

5.6 Future Work

Several directions for future research and development emerge from this work. Addressing the shortcomings of the non-linear assumptions is the most prominent direction. We see that this can be done in two ways: either by increasing model complexity or by working around the most prominent issues.

5.6.1 Nonlinear Tire Models

The current linear tire approximation limits the operating range of the estimator to non-aggressive maneuvers. Future iterations should investigate the integration of nonlinear models, such as Pacejka's Magic Formula, to accurately capture tire behavior at high slip angles and heavy load transfers during emergency lane changes or high-speed cornering.

5.6.2 Stiffness Lookup Tables

To address the transient lag and shifting reference intervals discussed in section 5.3, a state-space lookup-table approach should be evaluated. The estimation framework could learn to map axle stiffness values to specific state-space positions during standard driving. Given enough information about relevant maneuvers, this would allow the system to supply accurate, on-demand parameter estimates for predictive vehicle models without the computational overhead and calibration complexity required by continuous nonlinear tire dynamics estimation.

5.6.3 Extended Experimental Validation

While this framework utilizes high-fidelity co-simulation and foundational MUSE experimental data, comprehensive experimental validation on a fully instrumented real vehicle is required. Addressing practical challenges such as sensor calibration and real-time implementation constraints is critical. Utilizing a test vehicle equipped with a synchronized IMU, RTK-GPS, individual wheel speed sensors, and a specialized

hitch load cell will provide necessary insights into isolating coupling forces and refining trailer parameter observability.

5.6.4 Extension to Alternative Vehicle Configurations

The established estimator architecture should be generalized for other heavy and articulated configurations, including buses, construction equipment, and passenger vehicles towing trailers. This requires adjusting mass and geometric parameters while potentially modifying the model structure to account for disparate suspension architectures and steering kinematics.

6

Conclusion

The estimation of tire cornering stiffness in articulated heavy-duty vehicles evaluated through an unscented Kalman filter framework establishes specific operational boundaries and model constraints. Addressing the primary research objectives:

- **Estimation Level:** Parameter identification at the simplified, lumped axle level within a single-track model demonstrates numerical convergence. Conversely, individual tire-level estimation in a two-track framework is structurally unobservable; the lack of independent lateral excitation between parallel wheel pairs renders the system over-parameterized.

- **Excitation Requirements:** Reliable estimation mandates sustained lateral excitation, optimized during steady-state cornering at distinct thresholds. There is sufficient excitation while $a_y > 0.7\,\mathrm{m\,s^{-2}}$, and the optimal excitation was found to be $a_y \approx 1.94\,\mathrm{m\,s^{-2}}$. Low-dynamic and non-dynamic straight-line maneuvers fail to excite lateral tire dynamics, generating insufficient observable data and halting parameter identification.

- **Parameter Update Strategy:** Continuous state updating during periods of low lateral excitation subjects the filter to noise-driven parameter drift. Implementing a conditional update strategy based on a local observability Gramian strictly gates parameter updates to periods of high lateral dynamics, effectively preserving converged stiffness values and stabilizing the estimator.

- **Algorithm Robustness:** The estimation architecture demonstrates structural resilience under degraded sensing conditions. Transitioning to individual wheel speed measurements—predicated on a zero-longitudinal-slip assumption—sustains lateral dynamic state tracking when direct velocity data is denied, resulting in a quantified but bounded expansion in estimation error for lateral velocity.

Despite functional validations under controlled conditions, the framework exposes critical limitations regarding the application of linear models to articulated dynamics. The planar single-track model systematically neglects roll, pitch, suspension compliance, and the massive dynamic load transfers inherent to trailer masses scaling up to 31 960 kg. Consequently, the linear tire assumption fundamentally breaks down under asymmetric load shifting. This structural

deficiency induces mathematical coupling where the estimator utilizes cornering stiffness as a free tuning variable to absorb unmodeled physical dynamics, yielding accurate lateral kinematic states but physically erroneous stiffness parameters.

Furthermore, the estimator exhibits a distinct transient lag when adapting to shifting stiffness reference intervals induced by varying longitudinal velocities. Because advanced predictive vehicle control requires exact *a priori* stiffness parameters at the absolute onset of a maneuver, this convergence delay restricts the current framework's utility for real-time model predictive applications.

Finally, trailer cornering stiffness remains weakly observable due to its strict reliance on lateral hitch forces and secondary articulation dynamics. Resolving these limitations in future architectures requires decoupling simultaneous state-parameter dependencies and integrating nonlinear tire mechanics to maintain validity during aggressive transient maneuvers.

References

[1] Z. Wu, L. Shen, S. Bai, F. Dong, and G. Yin, "Estimation of vehicle sideslip angle and tire cornering stiffness considering mass mismatch," in *2024 8th CAA International Conference on Vehicular Control and Intelligence (CVCI)*, 2024, pp. 1–7. DOI: 10.1109/CVCI63518.2024.10830268.

[2] D. Jeong, G. Ko, and S. B. Choi, "Estimation of sideslip angle and cornering stiffness of an articulated vehicle using a constrained lateral dynamics model," *Mechatronics*, vol. 85, p. 102 810, 2022, ISSN: 0957-4158. DOI: 10.1016/j.mechatronics.2022.102810. [Online]. Available: https://www.sciencedirect.com/science/article/pii/S0957415822000514.

[3] S. F. G. Ehlers, Z. Ziaukas, J.-P. Kobler, and H.-G. Jacob, "State and parameter estimation in a semitrailer for different loading conditions only based on trailer signals," in *2022 American Control Conference (ACC)*, 2022, pp. 2353–2360. DOI: 10.23919/ACC53348.2022.9867797.

[4] K. Han, M. Choi, and S. B. Choi, "Estimation of the tire cornering stiffness as a road surface classification indicator using understeering characteristics," *IEEE Transactions on Vehicular Technology*, vol. 67, no. 8, pp. 6851–6860, 2018. DOI: 10.1109/TVT.2018.2820094.

[5] J.-O. Hahn, R. Rajamani, and L. Alexander, "GPS-based real-time identification of tire-road friction coefficient," *IEEE Transactions on Control Systems Technology*, vol. 10, no. 3, pp. 331–343, 2002. DOI: 10.1109/87.998016.

[6] Y. Wang, K. Geng, L. Xu, Y. Ren, H. Dong, and G. Yin, "Estimation of sideslip angle and tire cornering stiffness using fuzzy adaptive robust cubature kalman filter," *IEEE Transactions on Systems, Man, and Cybernetics: Systems*, vol. 52, no. 3, pp. 1451–1462, 2022. DOI: 10.1109/TSMC.2020.3020562.

[7] J. Feng, Z. Gao, and B. Guo, "An adaptive vehicle stability enhancement controller based on tire cornering stiffness adaptations," *World Electric Vehicle Journal*, vol. 16, no. 7, 2025, ISSN: 2032-6653. DOI: 10.3390/wevj16070377. [Online]. Available: https://www.mdpi.com/2032-6653/16/7/377.

[8] R. Anderson and D. Bevly, "Estimation of tire cornering stiffness using GPS to improve model based estimation of vehicle states," in *IEEE Proceedings. Intelligent Vehicles Symposium, 2005.*, 2005, pp. 801–806. DOI: 10.1109/IVS.2005.1505203.

[9] F. S. Hover and M. S. Triantafyllou, *Introduction to moving-frame kinematics*, MIT OpenCourseWare, adapted in LibreTexts, 2009. [Online]. Available: https://eng.libretexts.org/Bookshelves/Mechanical_Engineering/System_Design_for_Uncertainty_(Hover_and_Triantafyllou)/09%3A_Kinematics_of_Moving_Frames/9.01%3A_Introduction_to_Moving-Frame_Kinematics.

[10] M. Fowler, *Lecture 1*, University of Virginia Physics 252 course notes, Accessed: 2026-05-04, 1998. [Online]. Available: https://galileo.phys.virginia.edu/classes/252/lecture1.htm.

[11] R. Rajamani, *Vehicle Dynamics and Control*, 2nd. New York, NY: Springer, 2011, ISBN: 978-1-4614-1432-2. DOI: https://doi.org/10.1007/978-1-4614-1433-9.

[12] F. S. Hover and M. S. Triantafyllou, *Introduction to moving-frame kinematics*, MIT OpenCourseWare, adapted in LibreTexts, 2009. [Online]. Available: https://eng.libretexts.org/Bookshelves/Mechanical_Engineering/System_Design_for_Uncertainty_(Hover_and_Triantafyllou)/09%3A_Kinematics_of_Moving_Frames/9.03%3A_Differential_Rotations.

[13] F. S. Hover and M. S. Triantafyllou, *Introduction to moving-frame kinematics*, MIT OpenCourseWare, adapted in LibreTexts, 2009. [Online]. Available: https://eng.libretexts.org/Bookshelves/Mechanical_Engineering/System_Design_for_Uncertainty_(Hover_and_Triantafyllou)/09%3A_Kinematics_of_Moving_Frames/9.02%3A_Rotation_of_Reference_Frames.

[14] MIT OpenCourseWare, *3d rigid body kinematics*, Lecture 25, 16.07 Dynamics, 2009. [Online]. Available: https://ocw.mit.edu/courses/16-07-dynamics-fall-2009/419be4d742e628d70acfbc5496eab967_MIT16_07F09_Lec25.pdf.

[15] D. Schramm, M. Hiller, and R. Bardini, "Kinematics and dynamics of the vehicle body," in *Vehicle Dynamics: Modeling and Simulation*. Berlin, Heidelberg: Springer Berlin Heidelberg, 2018, pp. 95–102, ISBN: 978-3-662-54483-9. DOI: 10.1007/978-3-662-54483-9_5. [Online]. Available: https://doi.org/10.1007/978-3-662-54483-9_5.

[16] IPG Automotive GmbH, *Truckmaker reference manual*, Version 15.0, IPG Automotive GmbH, Karlsruhe, Germany, 2025.

[17] T. D. Gillespie, *Fundamentals of Vehicle Dynamics*. Society of Automotive Engineers (SAE), 1992.

[18] M. Doumiati, A. C. Victorino, A. Charara, and D. Lechner, "Onboard real-time estimation of vehicle lateral tire–road forces and sideslip angle," *IEEE/ASME Transactions on Mechatronics*, vol. 16, no. 4, pp. 601–614, 2011. DOI: 10.1109/TMECH.2010.2048118.

[19] S. K. Clark, Ed., *Mechanics of Pneumatic Tires*. Washington, DC: U.S. Government Printing Office, 1981, U.S. Department of Transportation, National Highway Traffic Safety Administration, 931pp.

[20] H. Dugoff, P. S. Fancher, and L. Segel, "Tire performance characteristics affecting vehicle response to steering and braking control inputs," University of Michigan Highway Safety Research Institute, Tech. Rep., Aug. 1969, 105pp.

[21] R. S. Sharp and M. A. El-Nashar, "A generally applicable digital computer based mathematical model for the generation of shear forces by pneumatic tires," *Vehicle System Dynamics*, vol. 15, no. 4, pp. 187–209, 1986.

[22] W. E. Meyer and H. W. Kummer, "Mechanisms of force transmission between tire and road," SAE, Tech. Rep. 620407, 1962. DOI: 10.4271/620407.

[23] R. D. Ervin, "The state of knowledge relating tire design to those traction properties which may influence vehicle safety," University of Michigan Transportation Research Institute, Tech. Rep. UM-HSRI-78-31, Jul. 1978, 128pp.

[24] D. L. Nordeen and A. D. Cortese, "Force and moment characteristics of rolling tires," SAE International, Tech. Rep. 640028, 1963. DOI: 10.4271/640028.

[25] R. Yuan-yuan, Z. Xue-lian, and L. Xian-sheng, "Handling stability of tractor semitrailer based on handling diagram," *Discrete Dynamics in Nature and Society*, vol. 2012, Aug. 2012. DOI: 10.1155/2012/350360.

[26] A. A. Ahmed, J. Santhosh, and F. W. Aldbea, "Vehicle dynamics modeling and simulation with control using single-track model," in *2020 IEEE International Women in Engineering (WIE) Conference on Electrical and Computer Engineering (WIECON-ECE)*, IEEE, 2020, pp. 1–4. DOI: 10.1109/WIECON-ECE52138.2020.9397983.

[27] B. Shao and Y. Dai, "The cafnn-based identification technique for autonomous vehicle dynamics model," in *2024 2nd International Conference on Artificial Intelligence and Automation Control (AIAC)*, IEEE, 2024, pp. 102–106. DOI: 10.1109/AIAC63745.2024.10899583.

[28] Ubaidillah, K. Pamungkas, M. Nizam, and S. A. Mazlan, "Simulation and model verification of a vehicle handling dynamics," in *Joint International Conference on Electric Vehicular Technology and Industrial, Mechanical, Electrical and Chemical Engineering (ICEVT & IMECE)*, IEEE, 2015, pp. 280–285. DOI: 10.1109/ICEVTIMECE.2015.7496694.

[29] Y. Boukadida, A. Masmoudi, G. M. Casolino, and F. Marignetti, "A simple assessment of the dynamics of road vehicles," in *2018 Thirteenth International Conference on Ecological Vehicles and Renewable Energies (EVER)*, IEEE, 2018, pp. 1–6. DOI: 10.1109/EVER.2018.8362416.

[30] P. Yih, J. Ryu, and J. Gerdes, "Modification of vehicle handling characteristics via steer-by-wire," in *Proceedings of the 2003 American Control Conference, 2003.*, vol. 3, 2003, 2578–2583 vol.3. DOI: 10.1109/ACC.2003.1243465.

[31] H. B. Pacejka, *Tire and Vehicle Dynamics*. Elsevier, 2005.

[32] KKTSE, *Single track (bicycle) model*, Accessed: 2026-05-04, Sep. 2018. [Online]. Available: https://kktse.github.io/jekyll/update/2018/09/18/single-track-bicycle.html.

[33] W. Just and F. Vivaldi, *Dynamical systems: An ltcc course*, Last updated January 16, 2019, 2019. [Online]. Available: https://webspace.maths.qmul.ac.uk/f.vivaldi/teaching/ltcc_dyn/notes.pdf.

[34] S. Särkkä and L. Svensson, *Bayesian Filtering and Smoothing*, 2nd ed. Cambridge University Press, 2023, ISBN: 9781108926645. [Online]. Available: https://www.cambridge.org/9781108926645.

[35] G. Reina, M. Paiano, and J.-L. Blanco-Claraco, "Vehicle parameter estimation using a model-based estimator," *Mechanical Systems and Signal Processing*, vol. 87, pp. 227–241, 2017, Signal Processing and Control challenges for Smart Vehicles, ISSN: 0888-3270. DOI: 10.1016/j.ymssp.2016.06.038. [Online]. Available: https://www.sciencedirect.com/science/article/pii/S0888327016302205.

[36] S. Särkkä and L. Svensson, *Bayesian Filtering and Smoothing*, 2nd. Cambridge University Press, 2023, Pre-publication version available via Cambridge University Press.

[37] Z. Chen, C. Heckman, S. Julier, and N. Ahmed, "Weak in the nees?: Autotuning kalman filters with bayesian optimization," in *2018 21st International Conference on Information Fusion (FUSION)*, 2018, pp. 1072–1079. DOI: 10.23919/ICIF.2018.8454982.

[38] Y. Bar-Shalom, X. R. Li, and T. Kirubarajan, *Estimation with Applications to Tracking and Navigation*. Wiley-Blackwell, 2001, ISBN: 9780471465218.

[39] A. J. Krener and K. Ide, "Measures of unobservability," in *Proceedings of the 48h IEEE Conference on Decision and Control (CDC) held jointly with 2009 28th Chinese Control Conference*, 2009, pp. 6401–6406. DOI: 10.1109/CDC.2009.5400067.

[40] T. Glad and L. Ljung, *Control Theory*. Taylor & Francis, 2000, ISBN: 9780748408788.

[41] Oxford Technical Solutions, *Rt3000 v3 product guide*, Datasheet for High-Precision Inertial Navigation Systems, Oxford Technical Solutions Ltd (OXTS), Oxfordshire, UK, 2024. [Online]. Available: https://www.oxts.com/the-rt3000-v3-datasheet/.

[42] A. Ceder, *Muse: Multiple unit state estimation*, 2025. [Online]. Available: https://github.com/DarthDazzle/MUSE.

[43] L. Fosse and S. Ahsan Ali Shah, *MMSX30 TCS estimation*, 2026. [Online]. Available: https://github.com/f0sse/mmsx30-tcs-estimation.

[44] IPG Automotive GmbH, *Truckmaker user's guide*, Version 15.0, IPG Automotive GmbH, Karlsruhe, Germany, 2025.

A

Additional Results

This appendix includes additional results that are not included in the main report but are mentioned explicitly. They are included to give extra context to the results shown in the report.

A.1 TwoTrack Model

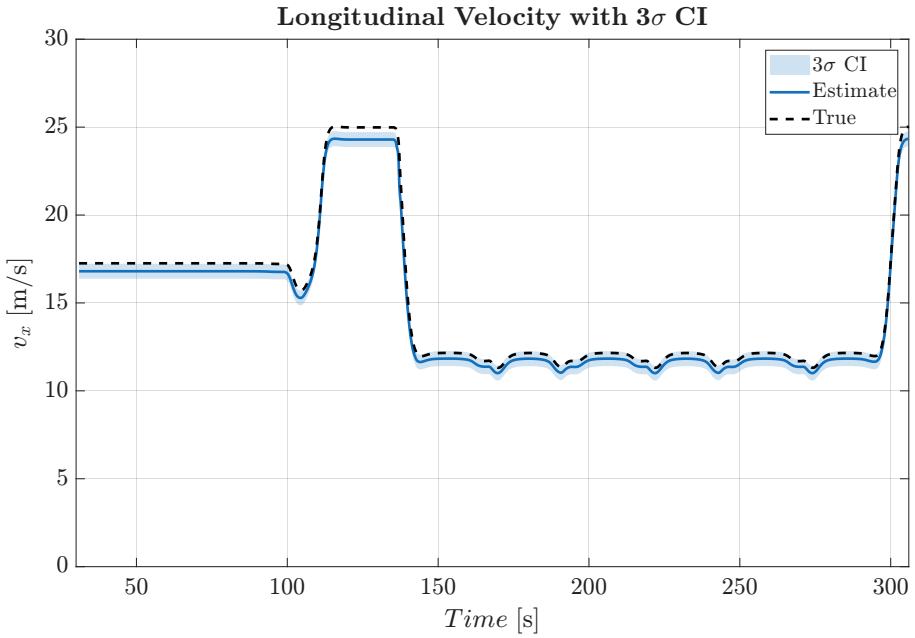

Figure A.1: Estimated longitudinal velocity for the two-track vehicle model together with the corresponding reference signal and the estimated 3σ confidence interval. The estimated 3σ confidence interval reaches approximately ± 300. For improved visualization, the plotted axis range is clipped to highlight the estimator behavior.

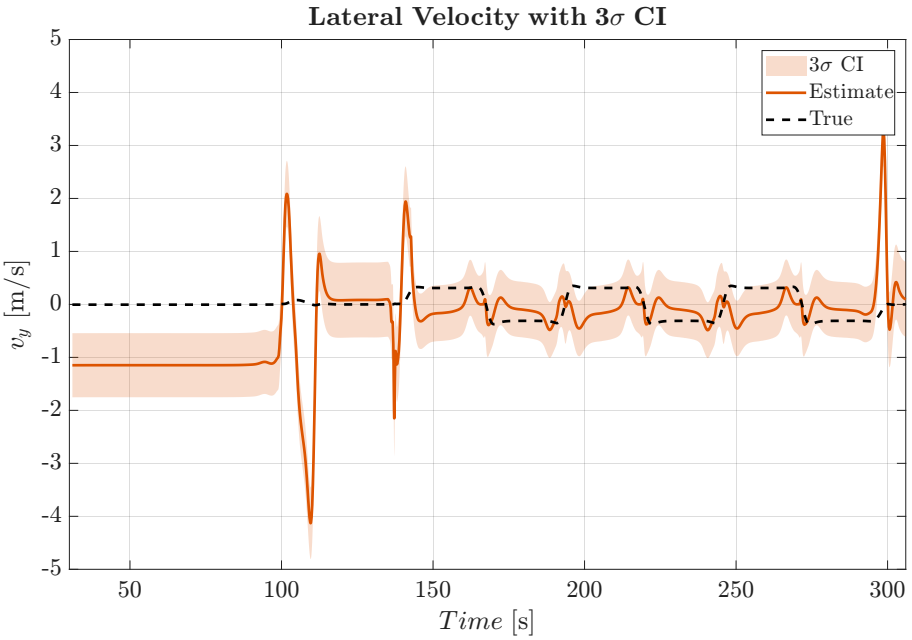

Figure A.2: Estimated lateral velocity for the two-track vehicle model together with the corresponding reference signal and the estimated 3σ confidence interval. The estimated 3σ confidence interval reaches approximately ± 300. For improved visualization, the plotted axis range is clipped to highlight the estimator behavior.

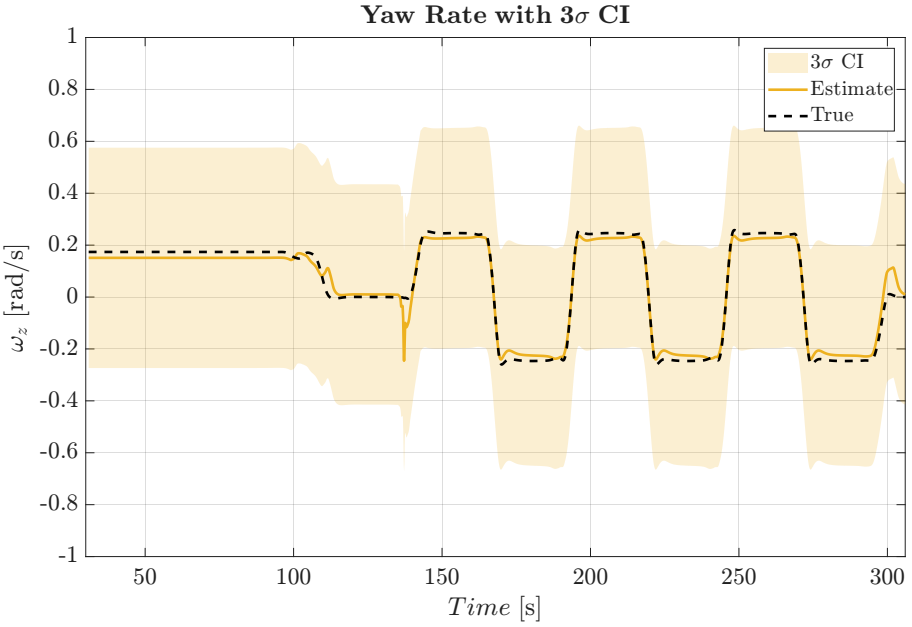

Figure A.3: Estimated yaw rate for the two-track vehicle model together with the corresponding reference signal and the estimated 3σ confidence interval. The estimated 3σ confidence interval reaches approximately ± 300. For improved visualization, the plotted axis range is clipped to highlight the estimator behavior.

A.2 One Track Model Nonlinearity

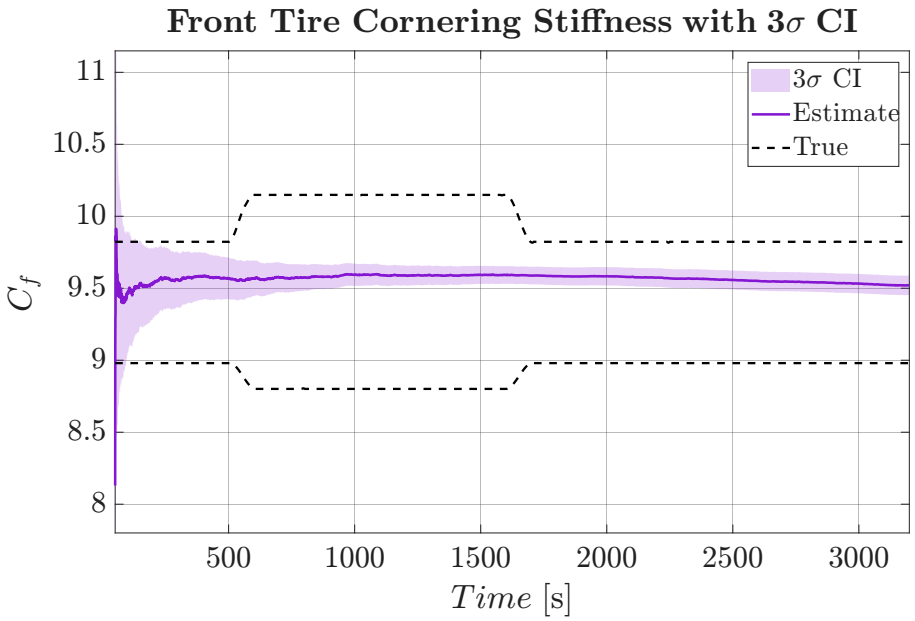

Figure A.4: Tractor-only front cornering stiffness estimate, driving the steady-state circle while varying the longitudinal velocity 50 km/h → 60 km/h → 50 km/h during an extended simulation spanning almost an hour of driving.

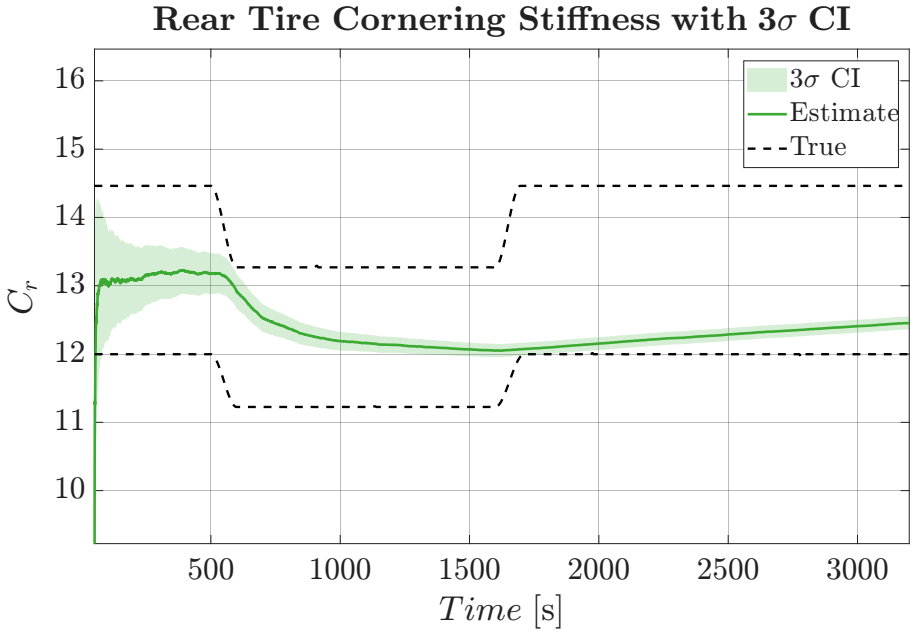

Figure A.5: Tractor-only rear cornering stiffness estimate, driving the steady-state circle while varying the longitudinal velocity 50 km/h → 60 km/h → 50 km/h during an extended simulation spanning almost an hour of driving.

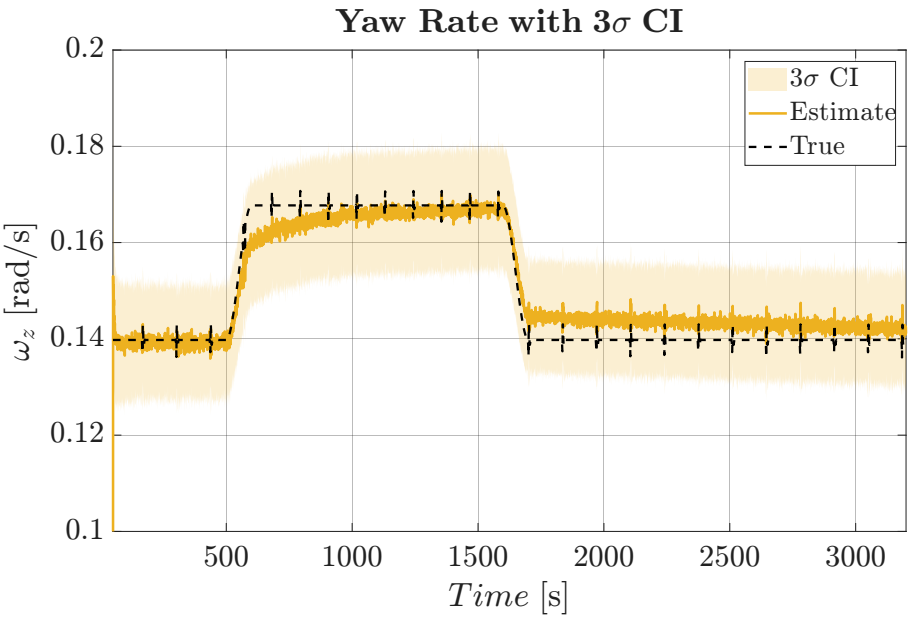

Figure A.6: Tractor-only lateral velocity estimate, driving the steady-state circle while varying the longitudinal velocity 50 km/h → 60 km/h → 50 km/h during an extended simulation spanning almost an hour of driving.

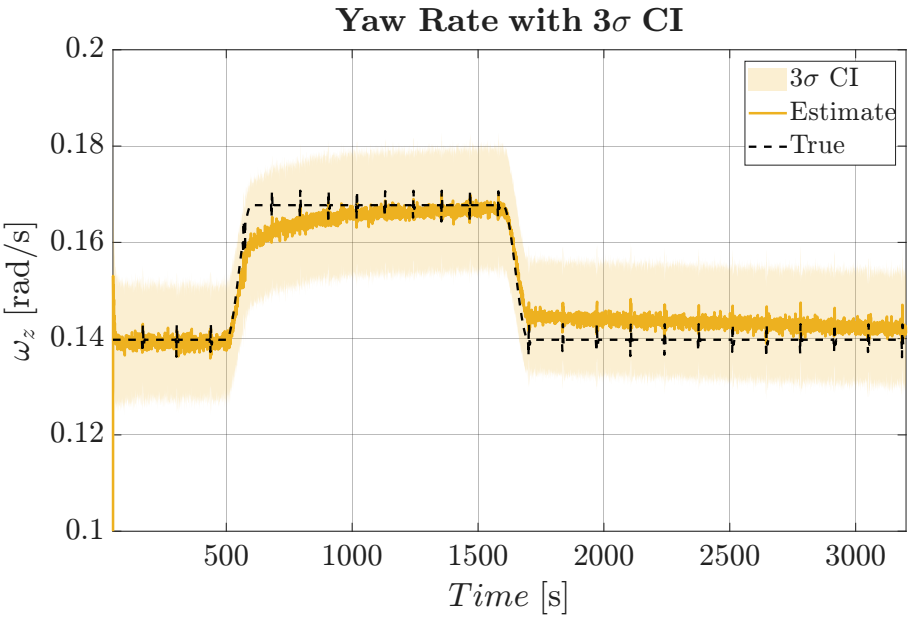

Figure A.7: Tractor-only yaw rate estimate, driving the steady-state circle while varying the longitudinal velocity 50 km/h → 60 km/h → 50 km/h during an extended simulation spanning almost an hour of driving.

DEPARTMENT OF MECHANICS AND MARITIME SCIENCES
CHALMERS UNIVERSITY OF TECHNOLOGY
Gothenburg, Sweden
www.chalmers.se

CHALMERS
UNIVERSITY OF TECHNOLOGY